A study of nitrogen-containing, high manganese austenitic stainless steel coatings deposited by sputter PVD

By:

Lynne Hopkins

A thesis submitted in partial fulfilment of the requirements for the degree of Doctor of Philosophy

The University of Sheffield
Faculty of Materials Science and Engineering

July, 2019

ABSTRACT

The use of nitrogen as an alloying element in steel is either limited to small quantities (<2 wt% / 7. 5 at%) in bulk materials, where it is used primarily as an austenite stabiliser and mechanical/tribological property enhancer, or introduced in much larger quantities (e.g. 38 at%) in thermochemical surface engineering treatments – where it is used to create a hard, corrosion-resistant diffusion layer of typically 20-30 μm depth, commonly referred to as "Expanded austenite" or "S-phase". This study examines the effects of nitrogen incorporation in a high-manganese austenitic stainless steel (Staballoy AG 17), at levels that lie between these two extremities with the intention of improving the mechanical and wear properties without compromising the inherent high resistance to corrosion which such alloys possess.

Thick, dense and featureless coatings of austenitic-manganese steel containing different levels of interstitial nitrogen were deposited by reactive magnetron sputtering in an argon-nitrogen plasma. The resulting microstructures, characterized by XRD, SEM/EDX, nano-indentation, and fracture analysis were found to exhibit a texture and a small nitrogen gradient across their thickness. With increasing nitrogen content, the hardness was observed to increase and the morphology changed. Moreover, changes in nitrogen content were found to have a more profound effect on the coating properties than any of the process parameters evaluated, the results of which are presented. Excessive nitrogen resulted in the precipitation of Mn_4N, apparently avoiding chromium sensitisation. Finally, since the deposited coatings were characterized by high compressive stresses, the stresses involved and the failure modes observed are discussed.

ACKNOWLEDGEMENTS

I truly appreciate the opportunity to work on this project given by: my supervisors – Dr Adrian Leyland and Prof Allan Matthews; Dr Glen Cassar and Dr Ann Zammit; and the European Research Council that funded the research. I would also like to express my most sincere gratitude to Dr Adrian Leyland for his invaluable insights, guidance, supervision and support throughout the research.

The help and assistance given by Ms Dawn Bussey with nano-indentation, Dr Nik Reeves McLaren with the XRD technique and Dr Le Ma, Dr Cheryl Shaw and Dr Peter Korgul with the SEM/EDX equipment is very much appreciated. Special thanks go to Mr John Lowndes, who gave invaluable technical support on the PVD equipment. I am also grateful to my colleagues and (mostly) former members of the RSCE group Dr Gorkem Yumusak, Dr Xingguang Liu, Mr David Brown, Dr Xiao Tao, Dr Chang Liu, Dr Wei-Yu Chen and Dr Hussein Meshrghi. I would also like to offer sincere thanks to the University of Malta, department of Metallurgy & Materials Engineering staff, particularly Dr Glen Cassar, Prof Joseph Buhagiar and Dr Ann Zammit, for providing use of and assistance with the equipment at the University of Malta.

Special thanks go to my friends in Sheffield, most especially Ms Hande Özbayraktar, for being like a sister to me; and Mr Nikola Tanov, for not only being a friend, but also for helping me with his experience on SEM/EDX.

Finally, I would like to thank my beloved parents for their support – both moral and financial – and my husband Dr Emir Avcioglu, for his love and endless support, without which, I would not have completed my PhD.

CONTENTS

ABSTRACT i

ACKNOWLEDGEMENTS ii

LIST OF FIGURES vii

LIST OF TABLES xi

CHAPTER 1: INTRODUCTION 1

1.1 Introduction 1

1.2 Aims and objectives 3

1.3 Thesis layout 4

CHAPTER 2. NITROGEN IN STAINLESS STEEL 5

2.1 Stainless steel 5

2.1.1 Introduction 5
2.1.2 Classification of steels 5
2.1.3 Stainless steel 6

2.2 Nitrogen alloying of steels 12

2.2.1 Nitrogen in bulk 12
2.2.2 Surface treatments 14

CHAPTER 3: PVD AND PROPERTIES OF DEPOSITED COATINGS 19

3.1 PVD processing 19

3.1.1 Introduction 19
3.1.2 Sputter deposition 21
3.1.3 Magnetron sputtering 24
3.1.4 Unbalanced magnetron sputtering 25

3.2 Process parameters 28
3.2.1 Base pressure 28
3.2.2 Working pressure 28
3.2.3 Reactive sputtering 30
3.2.4 Target power 32
3.2.5 Pulsed magnetron sputtering 34
3.2.6 Target-to-substrate distance 38
3.2.7 Substrate bias 38
3.2.8 Substrate pulsed bias 39
3.2.9 Substrate temperature 41
3.3 Coating Characteristics 43
3.3.1 Structure-zone models 43
3.3.2 Coatings from alloy or compound targets 47
3.3.3 Stress 47
3.3.4 Adhesion 54
3.4 Sputtering of austenitic stainless steel coatings 55
CHAPTER 4 – EXPERIMENTAL EQUIPMENT AND PROCEDURES 63
4.1 Materials used 63
4.2 Substrate preparation 64
4.3 Coating deposition 65
4.3.1 Deposition apparatus 65
4.3.2 Equipment preparation 67
4.3.3 Deposition procedure 68
4.4 Analytical techniques 69
4.4.1 X-Ray diffraction 70
4.4.2 Scanning electron microscopy (SEM) and energy-dispersive X-ray spectroscopy (EDX) 71
4.4.3 Nano-indentation hardness measurements 72
4.4.4 Fracture analysis 72
4.4.5 Potentiodynamic corrosion tests 73

4.4.6 Statistical considerations 74

CHAPTER 5: RESULTS AND DISCUSSION 75

5.1 Introduction 75

5.2 Generic observations 75

5.2.1 Morphology and deposition temperature 75
5.2.2 Chemical composition 77
5.2.3 Adhesion 79

5.3 Target power 80

5.4 Pulsed target parameters: frequency and duty cycle 85

5.5 Substrate bias 91

5.6 Substrate pulsing 95

5.7 Substrate material 98

5.8 Nitrogen doping 102

5.8.1 Corrosion testing 108
5.8.2 Nitride precipitation 110

5.9 De-adhesion and stress 114

5.10 Summary 119

CHAPTER 6: CONCLUSIONS AND FUTURE WORK 123

6.1 Main findings 123

6.2 Future Work 125

6.3 Concluding remarks 126

REFERENCES 129

APPENDIX I 145

I.I Composition of materials used 145

I.II Relevant thermal properties 145

APPENDIX II – XRD PEAK POSITIONS 147

II.1 Austenite and ferrite 147

II.2 Chromium nitrides..147

II.3 Manganese nitrides 148

LIST OF FIGURES

Figure 2. 1 Classification of Steels, adapted from Callister, Jr. [15] 6

Figure 2. 2 Classification of Stainless Steel Grades by microstructural class, adapted from EN10088-2:2014 [20]...8

Figure 2. 3 Optical micrograph of microsection of AISI 316 steel nitrided at 450 °C, from [46] 16

Figure 3. 1 Classification of PVD techniques by target varpourisaton methods, compiled from [77] and [73] 20

Figure 3. 2 Sputtering principle, adapted from [75]..22

Figure 3. 3 Schematic diagram of some processes occurring after ion impact, adapted from [78]...22

Figure 3. 4 (a) Conventional 'balanced' magnetron; (b) and (c) Unbalanced magnetrons of Types I and II respectively..25

Figure 3. 5 Multiple unbalanced magnetron sputtering configurations 27

Figure 3. 6 (a) Schematic diagram of a target voltage waveform in PMS and (b) an actual oscilloscope trace of a target voltage waveform in PMS operation, from [110]. In both cases the frequency was set to 100 Hz with a duty cycle of 80 %...36

Figure 3. 7 Variation in substrate ion current with pulse frequency & bias, adapted from [124] 40

Figure 3. 8 Thornton's structure-zone model [96,130] 44

Figure 3. 9 Anders' extended and modified structure zone diagram, applicable to energetic deposition [131] 46

Figure 3. 10 Manifestations of (a) Compressive and (b) Tensile stress, adapted from [73] 54

Figure 3. 11 An example of nitrogen content in sputter-deposited AISI 316 coatings with nitrogen percentage in the gas mixture (N + Ar) during deposition, from reference [133]. 57

Figure 3. 12 Lattice parameter, a (nm) with nitrogen content (nitrogen atoms per 100 metal atoms), from reference [48]...57

Figure 4. 1 Schematic diagram of the target and substrate holder configuration of the Nordiko unbalanced magnetron sputtering equipment 66

Figure 4. 2 (a) the substrate holder mounted with substrates, and (b) the target and substrate holder during a deposition run in the Nordiko unbalanced magnetron sputtering rig. 66

Figure 4. 3 Mounting of samples, with coating-to-coating interface 71

Figure 4. 4 Schematic diagram of sample preparation for fracture analysis, showing notch and direction of bending following immersion in liquid nitrogen 73

Figure 5. 1 (a) SEM polished cross section and (b) Fractured surface of coating deposited in an argon-only environment, at 1500W target power and -70V substrate bias...76

Figure 5. 2 Temperature profile in a typical sputter deposition run...............................77

Figure 5. 3 EDX line scan across the cross-section of a coating deposited in an argon atmosphere at 1500 W (123 kHz, 90%), -70 V (250 kHz, 88%) substrate bias. Substrate, AISI 304 steel, and coating sections are indicated. 79

Figure 5. 4 Deposition rate vs. wattage, for runs conducted at a pulsed power (123 kHz, 90%), and -70 V (250 kHz, 88%) substrate bias 82

Figure 5. 5 (a) theta-2theta XRD patterns for coatings deposited at 1500W and 1200W in an argon only atmosphere; (b) GAXRD patterns for coatings deposited in a nitrogen containing atmosphere (4sccm) at 1200W and 1000W; (c) Peaks for ferrite and austenite, as per PDF cards 00-006-0696 and 04-018-3211, respectively..83

Figure 5. 6 Examples of fracture from coatings deposited in an argon atmosphere at 1500 W (a), (b) and 1200 W (c),(d) 85

Figure 5. 7 (a) Theta-2theta XRD patterns for coatings deposited at different duty cycles at 1200 W, 123 kHz and nitrogen flow rate of 10 sccm and (b) GAXRD patterns for coatings deposited at different duty cycles at a target power of 1000 W, 123 kHz and 4 sccm nitrogen flow rate. 87

Figure 5. 8 (a) Theta-2theta XRD patterns for coatings deposited at different frequencies at 1200 W, 10 sccm nitrogen; (b) GAXRD patterns of coatings deposited at different frequencies at 1000 W and 4 sccm nitrogen; (c) Peak positions for austenite and Mn_4N as per PDF cards 04-018-3211 and 01-089-3704, respectively..90

Figure 5. 9 Nitrogen content, thickness and hardness against substrate bias (pulsed at 250 kHz, 88 % duty cycle) for coatings deposited at 1200 W (123 kHz, 90 % duty cycle) and flow rate of 4 sccm nitrogen 91

Figure 5. 10 GAXRD patterns for coatings deposited at a pulsed target power of 1200 W (123 kHz, 90 % duty cycle), nitrogen flow rate of 4sccm, and different pulsed (250 kHz, 88 % duty cycle) substrate bias values -40, -70 and -100 V. Superimposed are the austenite peaks from PDF card 04-018-3211 ...93

Figure 5. 11 SEM cross-sectional images of coatings deposited at pulsed target power of 1200 W (123 kHz, 90 % duty cycle), nitrogen flow rate of 4sccm, and pulsed (250 kHz, 88 % duty cycle) substrate bias values of -110 V (a) and -40 V (b)..94

Figure 5. 12 Theta-2theta XRD patterns for coatings deposited in pulsed (250 kHz, 88 % duty cycle) and DC mode, at different nitrogen flow rates (5 or 10 sccm) and power 1200 W (123 kHz, 90 % duty cycle)......................................97

Figure 5. 13 (a) Theta-2theta XRD patterns for coatings deposited onto different substrates: steel and glass. Also displayed are the peak positions and relative intensities for ferrite and austenite as per PDF cards 00-006-0696 and 04-018-3211 respectively. (b) shows same patterns in (a) but in logarithmic scale...99

Figure 5. 14 Fracture of coating deposited on steel (a) and glass (b) in an argon atmosphere, 1500 W target power and -70 V substrate bias..................101

Figure 5. 15 Elemental composition by EDX, across the cross-section of a coating having an average of 24 at% nitrogen...103

Figure 5. 16 Cross-sectional images of a 29 at% Nitrogen containing deposit in SE (a) and BSE (b) modes. Arrows show the interface 104

Figure 5. 17 Fracture of 24 at% nitrogen coating (deposited using a pulsed target power of 1200 W and a pulsed substrate bias of -70 V) showing a columnar structure...105

Figure 5. 18 Theta-2theta XRD patterns of coatings with different nitrogen levels: 0, 7, 13 and 24at%, all remaining parameters constant 106

Figure 5. 19 Potentiodynamic tests in Ringer’s solution for AISI 304 steel (grey), Staballoy AG17 coating with no added nitrogen (blue) and with 24 at% nitrogen (red). Coatings were deposited at a pulsed target power of 1200 W and pulsed substrate bias of -70 V 109

Figure 5. 20 (a) Theta-2theta XRD patterns for coatings containing high levels of nitrogen; (b) Peak positions for Mn_4N – PDF card 01-089-3704 and austenite, PDF card 04-018-3211..111

Figure 5. 21 Change in free energy against temperature for various chromium, manganese and iron nitrides, from [178] 112

Figure 5. 22 Examples of compressive stress manifestations following cutting: (a) Catastrophic failure showing curling of a coating and (b) Worm-tracks following cutting. 115

Figure 5. 23 An example of substrate damage in a coating that was deposited at a pulsed target power of 1200 W, pulsed substrate bias of -70 V and contains 7 at% nitrogen 116

Figure 5. 24 Deadhesion (a) and fracture of delaminated coating (b) produced using a target power of 1200 W (123 kHz, 90 % duty cycle), substrate bias -110 V (250 kHz, 88 % duty cycle) and 4 sccm Nitrogen flow rate 117

Figure II. 1 XRD peaks for ferrite, PDF card 00-006-0096 and austenite, PDF card 04-018-3211 147

Figure II. 2 XRD peaks for CrN, PDF card 01-076-2494 and Cr_2N, PDF card 01-079-2159 148

Figure II. 3 XRD peaks for MnN - PDF card 04-019-1077, $MnN_{0.43}$ - PDF card 04-007-2198, Mn_3N_2 - PDF card 01-089-3704 and Mn_4N - PDF card 01-089-3704 149

LIST OF TABLES

Table 2. 1 Classification of steels; generic properties and examples, compiled from [21–24]. 10

Table 2. 2 Properties of some common stainless steels, adapted from (BS) EN10095:1999 [28] & (BS) EN10088-2:2014 [20]..12

Table 3. 1 The zones in Thornton's structural zone model..45

Table 3. 2 Parameter effect on stress...53

Table 3. 3 Structures observed for stainless steel coatings deposited in literature 61

Table 4. 1 Chemical compositions of typical biomedical materials, as well as target and substrate materials. 64

Table 4. 2 Parameters used for sputter deposition process 69

Table 5. 1 Composition of target (at%): theoretical, measured and sputter-deposited coating...78

Table 5. 2 Parameters for runs deposited at different target powers.............................80

Table 5. 3 Hardness measurements for samples deposited at different target power 85

Table 5. 4 Parameters, thickness, nitrogen at% and hardness for samples deposited at different target pulse width and duty cycle..86

Table 5. 5 Parameters, thickness, nitrogen content and hardness for samples deposited at different target frequencies 88

Table 5. 6 Nitrogen content, thickness and hardness for coatings deposited in the pulsed and DC substrate bias modes, at different nitrogen flow rates 96

Table 5. 7 Elemental composition, thickness and hardness of coatings deposited onto different substrates: steel and glass...100

Table 5. 8 Hardness for coatings having different nitrogen contents..........................108

Table I. 1 Chemical composition of materials used 145

Table I. 2 Melting temperatures and thermal expansion coefficient from literature, and calculated using reference [190] 145

CHAPTER 1: INTRODUCTION

1.1 Introduction

Physical vapour deposition (PVD) coating techniques provide unrivalled flexibility to deposit materials with metastable structures and to, for example, supersaturate phases with interstitial atoms, such as nitrogen and carbon, or substitutional transition metal or metalloid atoms, to develop previously unobtainable mechanical, tribological or functional properties. The aim of this research was to exploit these advantages and by using PVD techniques, study the properties of novel alloys which cannot presently be manufactured by conventional methods. A scenario that fits within this broad scope was that presented by austenitic steel and its doping with nitrogen.

Nitrogen is used in the production of steels for a variety of reasons: as an austenite stabiliser and therefore, as a replacement for expensive nickel, to increase yield and ultimate tensile strengths and to improve corrosion resistance. Quantities in bulk materials are generally below 1 or 2 wt% (4-7.5 at%) [1–5] as larger quantities are unattainable by current conventional manufacturing methods. Moreover, higher nitrogen quantities have been reported under conventional casting or powder metallurgy processing to form nitride precipitates that deteriorate corrosion properties [6].

On the other hand, over the last 25-30 years, nitrogen has also seen increasingly extensive use in thermochemical surface engineering treatments to create hard, corrosion resistant stainless steel surfaces, referred to as expanded austenite. In these instances, low treatment temperatures, typically in the 300-500 °C range, suppressed nitride

precipitation, preserving corrosion properties, despite the nitrogen quantity could be as high as 38 at% [7]. Stainihard®, Expanite® and Bodycote's S^3P processes [8–10] are examples of commercial nitrogen (and/or carbon) diffusion processes that produce hard expanded austenite layers to improve wear resistance, galling and scratch resistance, while maintaining good corrosion resistance. Such treatments are generally applied to improve the lifetime of moving parts that incur wear. Examples include shafts, drive parts, valve and pump parts, plunges, guides and fasteners, in industries such as the food and beverage, automotive, medical devices and general engineering.

Clearly, there is a gap in the use of nitrogen as an alloying element: although it is used in quantities ranging from very small amounts (4-7.5 at%) in bulk materials to relatively much higher contents in surface engineering (38 at%), with benefits for using nitrogen lying at both ends, literature is very scarce on the materials whose nitrogen contents lie in between these two extremes. The original scope of this research was therefore to provide knowledge on how nitrogen content, particularly in those intermediate quantities, affects the mechanical, wear and corrosion resistance properties of austenitic steels. Employing PVD methods to produce thick coatings provides a means of achieving this goal by enabling the synthesis and characterisation of such novel alloys that currently cannot be manufactured commercially. Ultimately, the benefit of such a study would be to provide insight on whether methods for further increasing nitrogen content in bulk materials should be pursued as a means to improve the mechanical and wear resistance properties without compromising the generally inherent good corrosion resistance that austenitic steels exhibit.

1.2 Aims and objectives

In the light of the discussion in the previous section, the aim of this project was: to investigate the properties of austenitic stainless steels, particularly high manganese steels, that are stabilised as well as hardened by the interstitial incorporation of nitrogen at levels not currently achievable by conventional bulk metal processing, and hence i) improve mechanical properties, whilst retaining the good corrosion resistance of austenitic stainless steels, ii) reduce the cost of the alloy by the replacement of expensive nickel with manganese, and iii) development of novel alloys with a potential application in the medical industry due to the absence of nickel.

These aims have been translated to the following objectives:

1) To deposit thick manganese-rich stainless steel coatings. This would require an evaluation of parameters and the determination of optimum parameters.
2) To modify the stainless steel coatings by adding nitrogen to the coatings in different quantities.
3) To characterize the produced coatings and analyse their mechanical, wear and corrosion properties through various analytical techniques including XRD, SEM/EDX, hardness testing, scratch testing, electrochemical corrosion tests and other tribological wear tests.

1.3 Thesis layout

This work sets off with two literature review chapters: one giving a brief discussion on steels and assessing the available literature on the use of nitrogen in such steels and the other provides information on physical vapour deposition techniques. While the former chapter (Chapter 2), provides the reader with the background required to understand the role of nitrogen and the aims of this project, the other (Chapter 3) gives a brief description of PVD methods and how deposition parameters can affect the coating properties. The latter chapter is particularly important to understand the adhesion problems that were experienced in the initial trials and the sequence of experiments that had to be undertaken in order to address this problem.

Following the literature review chapters, Chapter 4 gives a detailed description of the equipment used, the procedure used to produce the coatings and the analytical techniques used to characterize them.

Chapter 5 provides the results for the experiments that were undertaken to understand the effect of different parameters on the austenitic stainless steel coatings, with the ultimate aims being to reduce the stress in the coatings that was causing deadhesion. Towards the end of the chapter the effect of nitrogen in the coatings is also evaluated.

Chapter 6 summarises the results from this study and gives some recommendations for future work.

CHAPTER 2. NITROGEN IN STAINLESS STEEL

2.1 Stainless steel

2.1.1 Introduction

The use of steel as a material finds its origins in India and Anatolia, around 2000 BC [11]. However, it was not until the industrial revolution, which saw the advent of the steam engine and critical developments in steel processing by Huntsman, Darby and Cort, that the production of steel gained momentum to the point where it is today the most abundant and essential of alloys, being applied to the industries of infrastructure, transportation, packaging, and machinery, amongst others.

Of course, nowadays, the metallurgy of steel is better understood, although research in steel is far from saturated, with many questions still remaining to be answered. Present endeavours entail reductions in energy consumption for steel production, improvements in strength to weight ratio and recyclability [11] – all of which support the 'sustainability' mind-set of modern industrial society.

2.1.2 Classification of steels

In the ASM Handbook, Krauss [12] defines steel as: "alloys of iron, carbon and other elements that contain less than 2 (wt)% carbon". Exceeding this limit, the alloy would

be classified as a cast iron. In addition to carbon, steels generally may contain other alloying elements, leading to a myriad of compositions that yield a most versatile range of properties [13].

Although steels can be classified in a variety of ways, the most generally applied system uses the chemical composition [14]. Figure 2.1, which has been adapted from Callister, Jr. [15], shows one example of such a classification. In this system, steels are categorised according to their alloying levels; the level of carbon content: low, medium or high; and whether there are additional alloying elements other than carbon and some manganese (plain carbon steels vs. alloy steels).

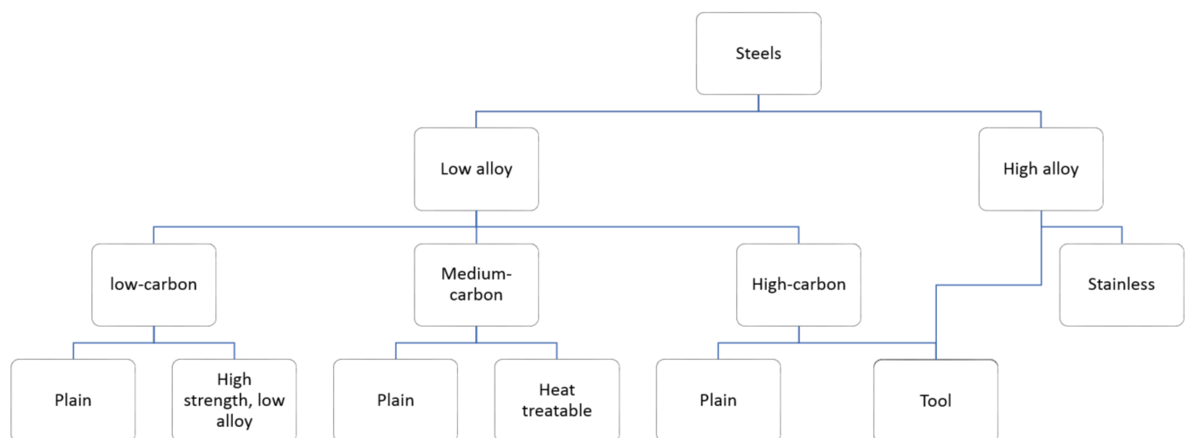

Figure 2. 1 Classification of Steels, adapted from Callister, Jr. [15]

2.1.3 Stainless steel

Amid the various conflicting claims of priority, Harry Brearley, of Sheffield UK, is generally accredited in 1913 with the discovery of the first commercially available

stainless steel, with 12.8 (wt)% chromium and 0.24 (wt)% carbon. As the story goes, the self-taught researcher set out experimenting with chromium and carbon in an attempt to employ the higher melting temperatures of chromium-iron alloys and create a more erosion resistant alloy able to withstand the temperatures and discharge gases endured by the barrel of a gun. However, when trying to etch the material to analyse its microstructure, Brearley found the steel to be highly resistant to acids and immediately realised its potential for the prevailing cutlery industry of Sheffield [16,17].

It would eventually be explained how chromium forms a tightly adherent surface oxide in air, that prevents any further oxidation, thereby protecting the underlying material [13]. Over time, numerous alloys have been developed and a stainless steel is nowadays considered to be any corrosion resistant alloy with minimum of 10.5 (wt)% chromium and less than 1.2 (wt)% carbon [18,19].

In the absence of any other alloying elements, an alloy with 13 (wt)% chromium would exhibit an entirely ferritic microstructure [12], i.e. one in which the primary phase is the body centred cubic ferrite. However, whilst chromium, like molybdenum, silicon and niobium is a ferrite stabiliser, other alloying elements, such as nickel, manganese, carbon and nitrogen, if retained in substitutional or interstitial solid solution, stabilize the face centred cubic austenite phase. In other words, different microstructures, as well as different property enhancements can be targeted through the correct balance of different alloying elements [12]. Stainless steels are in fact generally classified according to the nature of their microstructure [20]. Figure 2.2 displays how the listed 111 stainless steel grades in EN 10088-2:2014 are distributed by microstructural class and Table 2.1 provides the basic properties of each class, together with some staple examples.

Of particular interest in this research are the austenitic stainless steels and hence, these shall be discussed in further detail.

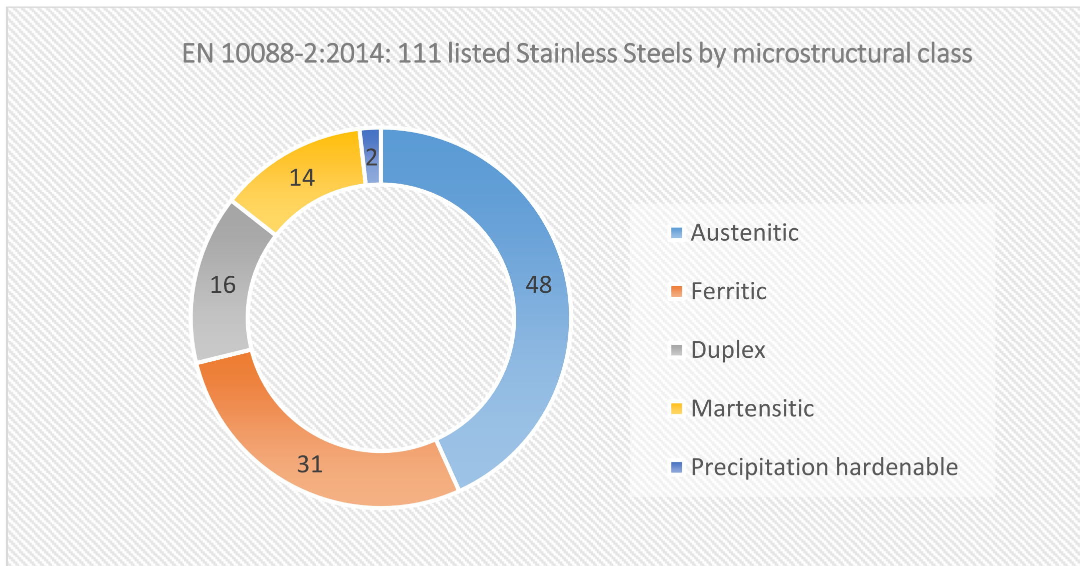

Figure 2. 2 Classification of Stainless Steel Grades by microstructural class, adapted from EN10088-2:2014 [20]

			Examples	
STAINLESS STEEL	FERRITIC	Cr: 10.5-30 %, C: <0.08 %, Mo: 0-4 % Magnetic, non-heat-treatable. Limited toughness, strength, formability and weldability (thin sections). Best suited for general and high temperature corrosion resistance; excellent chloride stress corrosion cracking resistance.	**AISI 430** (S43000)	Most common ferritic grade in sheet form. Cost effective and applied to many general purpose applications, such as washing machine drums, cutlery, catering equipment, lifts and window hinges.
			AISI 409 (S40900)	Low-cost (low Cr content) – with its dominant application being that for components of the aggressive, high temperature environment of the vehicle exhaust systems.

Type	Properties	Grade	Description
AUSTENITIC	Cr: 16-28 %, C: <0.08 %, Ni: 3.5-32 % Non-magnetic, non-heat treatable. Excellent corrosion resistance, ductility, formability and toughness. Generally weldable.	**AISI 304** (S30400)	The backbone of the steel industry with >50 % of stainless steel produced. Numerous applications across various industries, including the food, infrastructural, surgical, chemical and automotive industries.
		AISI 316 (S31600)	The addition of 2-3 % Mo (with respect to AISI 304) improves the corrosion resistance and this steel is therefore used in harsher environments such as marine conditions, heavy urban, acidic or high chloride environments.
MARTENSITIC	Cr: 11.5-18 %, C: 0.15-1.2 % (+Mo) Magnetic and heat treated for strength and hardness (that increases with carbon content). Increases in strength and hardness potential come at a cost of ductility and toughness. Limited corrosion resistance and caution is required for welding.	**AISI 420** (S42000)	Cost effective, high strength and wear resistance at basic corrosion resistance. Typical applications include cutlery blades, surgical instruments, drive shafts, bearings, gears and tools.
		AISI 416 (S41600)	With the addition of Sulphur (0.25/0.35 %) this steel exhibits excellent machinability, at a basic corrosion resistance and moderate strength and toughness. Applications typically include intricate components, shafts, axles, gears, golf club heads, sensors and gun barrels.

	Properties	Example	Applications
DUPLEX	Cr: 21-26 %, C: <0.03 %, Ni: 3.5-8 %, Mo: 0-4.5 % Magnetic, not heat treatable. Microstructure consists of a ferrite and austenite mixture, with the physical properties exhibited reflecting such a mixture. Properties include reasonable formability and weldability together with a higher strength than ferritic or austenitic (in annealed condition) and improved corrosion resistance, particularly, stress corrosion cracking (SCC) resistance.	**2205** (S31803/ S32205)	Used as an improvement over 316, offering better strength and corrosion resistance at the cost of some loss of toughness. It is therefore employed in more aggressive environments and industries such as the chemical, marine, nuclear, food processing and oil and gas.
PRECIPITATION HARDENING	Low temperature (500-800 °C) heat treatment gives very high strength through hard intermetallic compound precipitation and minimal distortion. Ductility and toughness depend on the heat treatment, weldability is good, while the corrosion resistance is medium (comparable to AISI 304).	**17-4PH** (S17400)	Combines good corrosion resistance, toughness and high strength. Its strength is obtained from copper particle precipitation in a martensitic matrix. Examples of applications include aerospace and medical components, drive shafts, bearings, gears and conveying equipment.

Table 2. 1 Classification of steels; generic properties and examples, compiled from [21–24]. *(All elemental quantities are in wt%)*

Austenitic stainless steels

Austenitic stainless steels are alloys of iron, chromium, nickel and/or manganese with small amounts of carbon (and of other alloying elements), the end result of which, however, is a microstructure exhibiting the austenite phase, which is a face centred cubic polymorph of iron. A good combination of ductility and strength, over a wide temperature range, together with formability, weldability and good corrosion resistance

are what make this class of stainless steels the largest group and the most widely used [25–27].

Austenitic stainless steels are generally used in an annealed form, which is obtained by heating to a temperature range of 1000-1200 °C followed by rapid cooling [25]. The resulting microstructure consists of a single austenitic phase made up of equiaxed grains and twins [12]. If the cooling rate is not fast enough, or if the material is subsequently exposed to temperatures in the 425-870 °C temperature range, ferric carbides may precipitate to the grain boundaries, depleting the surrounding areas of chromium making such areas susceptible to corrosion of intergranular type [6]. It is for this reason that austenitic alloys are not hardened by heat treatment, but by cold work or through alloying with, for example, nitrogen [25]. Reducing the carbon content (as in grades 304L and 316L), or alloying with stronger carbide formers such as titanium and niobium (as in grades 321 and 347) helps in suppressing ferric carbide formation.

It is while all the carbides and alloying elements are in solid solution that the best corrosion resistance is exhibited. This is the underlying principle of austenitic stainless steels: when alloying elements such as chromium and molybdenum, known ferrite stabilisers, are added to improve certain properties, generally corrosion resistance, nickel or other austenite stabilizers such as manganese, nitrogen and carbon, are also added to maintain the austenitic structure [26].

Another important aspect of this family's alloy design is the austenite stability relative to its transformation to the harder and more brittle martensite [12]. As austenite may be mechanically induced to undergo a martensitic transformation through cold work, the austenite stability will affect the work hardening rate and ductility [26]. Essentially, the

leaner the alloy, the less stable is the austenite as even ferrite phase promoters like chromium, stabilise the austenite by retarding martensitic transformation.

Table 2.2 displays some properties of some typical austenitic stainless steels.

Common name (AISI)	Steel No.	UNS	Yield Strength	Tensile Strength	Elongation	Notes on composition
304	1.4301	S30400	230	520	45	18Cr-8Ni
304L	1.4307	S30403	200	500	45	lower C version
310	1.4845	S31008	210	500	33	25Cr-20Ni
316	1.4401	S31600	220	520	40	17Cr-10Ni-2Mo
316L	1.4404	S31603	220	520	40	lower C version
321	1.4541	S32100	200	500	40	18Cr-9Ni, +Ti
347	1.4550	S34700	200	500	40	18Cr-9Ni, +Nb

Table 2. 2 Properties of some common stainless steels, adapted from (BS) EN10095:1999 [28] *& (BS) EN10088-2:2014* [20]

2.2 Nitrogen alloying of steels

2.2.1 Nitrogen in bulk

nitrogen is generally used as an alloying element in solid solution in stainless steels to fulfil one or more of the following roles: 1) as an austenite stabilizer replacing expensive nickel [29,30], 2) as a solid solution strengthener [3] and / or 3) an enhancer of properties such as creep strength [31] and corrosion resistance – for example pitting corrosion resistance [32], and intergranular corrosion cracking [33]. For instance, in the AISI 200 steel series – while the mechanical properties (yield strength) can be improved by 30 %

(when compared to the staple chromium-nickel steel AISI 304), the cost is decreased due to reduced nickel content (which is replaced by a combination of manganese and nitrogen) [34].

The solubility of nitrogen in pure iron is limited to 0.028 wt% but, as the solubility depends on pressure, temperature and alloy content, it can be increased by increasing the nitrogen gas pressure above the melt and through alloying additions. The work of Rawers et al., [35] gives evidence for both Sievert's law (that states that nitrogen solubility increases linearly with the square root of the nitrogen pressure over the melt) and the effects of alloying elements on the solubility, whereby whilst chromium and manganese increase the solubility of nitrogen in iron, nickel decreases it. In addition, the solubility also increases with a phase change from b.c.c. to f.c.c., which ultimately is also determined by the alloy composition. In the work of Rawers et al. [35], nitrogen solubility in the austenitic Fe-15Cr-15Mn alloy was increased from 0.56 wt% at an overpressure of 0.1 MPa, to 5.26 wt% at an overpressure of 200 MPa. However, the high amount of retained nitrogen formed nitrides in the alloy: Mn_4N for the initial case (0.56 wt%, 0.1 MPa), and CrN as the nitrogen content (and overpressure) increased further.

A high nitrogen steel has thus been defined as one where the nitrogen content exceeds 0.08 wt% in a ferritic microstructure and 0.4 wt% in an austenitic structure: whereby these values are the equilibrium nitrogen quantities that can be retained when the steel is processed at atmospheric pressure [36]. Examples of steel alloys that have been developed in the past decade in which nitrogen content exceeds 0.4 wt% (1.6 at%), are P550 (F2581-07) and P900 (18Cr-18Mn) which are characterised by high strength and corrosion resistance [1].

The yield strength of nitrogen alloyed austenitic stainless steels has been widely reported to increase with interstitial nitrogen content as a result of grain boundary hardening and solid solution strengthening [2–5]. However, in all of the alloys in these studies, nitrogen is generally limited to around 1 wt%. When this limit is exceeded, alloys become susceptible to precipitation of nitrides, typically di-chromium nitride (Cr_2N) [29,37,38]. Even when 1 wt% nitrogen is retained within the alloy, exposure to a temperature above 600 °C will also cause nitrides to precipitate. Cr_2N has a hexagonal [37,39] structure and tends to precipitate on grain boundaries first through discontinuous precipitation and eventually transgranularly through the matix [38]. The precipitation of Cr_2N is generally to be avoided, as this depletes chromium from the matrix, leaving the austenite in a 'sensitised' condition (i.e. susceptible to corrosion) [38,40]. Moreover, nitride precipitation has been shown to have an adverse effect on the ductility and toughness of the material [38]. To avoid such sensitisation, some steel grades intended to be used at higher application temperatures, are designed to include strong nitride formers such as titanium and niobium, to react with any nitrogen (or carbon) that can be found in the alloy, preventing the formation of chromium nitrides (or carbides) [41]. For instance, AISI 321 is designed in such a way that the titanium quantity is 5 times that of carbon and/or nitrogen [5 x (C % + N %)]. Similarly, AISI 347 contains niobium quantities at a minimum of 8 times the amount of carbon within the alloy.

2.2.2 Surface treatments

In the past 30 years, nitrogen has also played a major role in surface alloying treatments of stainless steel where the main aim of these treatments is improve mechanical and

tribological surface properties, namely, improving wear resistance without losing the good corrosion resistance normally attributed to such steels. High quantities of nitrogen (up to 30 at%) are dissolved in the austenitic stainless steels, mostly via plasma processes; typically by plasma nitriding [42–46], but also through processes like sputtering [47,48] and plasma immersion ion implantation [49]. The single phased, featureless, precipitate-free layer produced has been referred to by several names, most commonly, the 'S-phase' which was originally coined by Ichii et al. [50] in 1985 to designate the unrecognized XRD peaks of the supersaturated and 'expanded' austenite, latter description being attributed to Leyland et al. [51,52] reflecting the structurally anisotropic lattice expansion/strain of the austenite grains (which in part explains the 'unrecognized' XRD peaks). These processes are carried out at low temperatures (below c. 450 °C)– to avoid grain boundary nitride precipitation, the occurrence of which would, as explained in the previous section for bulk nitrogen alloying, compromise the corrosion resistance by locally depriving the matrix of chromium [42,43,49,53,54].

The 'S-phase' is characterized by a high hardness that can reach values as high as 15 GPa [55–57]. This high hardness is related to the nitrogen content in the material and has been shown to vary with the nitrogen content depth profile [44]. The shift of XRD peaks to lower angles reveals an increase in lattice parameter. This was also shown to increase with nitrogen content [53,54,56,58–61] and to follow the nitrogen profile for plasma nitrided samples [42,43].

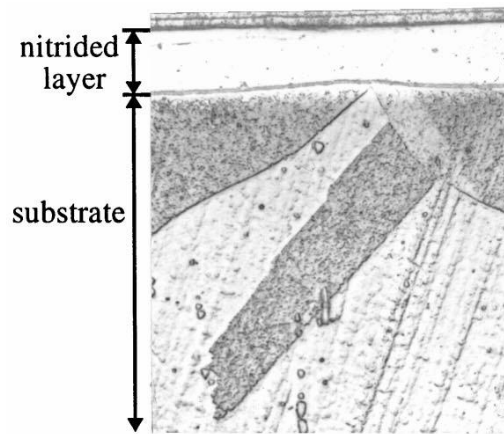

Figure 2. 3 Optical micrograph of microsection of AISI 316 steel nitrided at 450 °C, from [46]

A cross section of a material with an expanded austenite surface layer would typically show a featureless white layer on top of the apparently unaffected substrate (Figure 2.3) [43,46,56]. This occurs essentially as a result of a superior resistance of the nitrogen-rich layer to the etching agent used. Studies investigating the corrosion properties of expanded austenite often find that while the bulk corrosion resistance is maintained [44,49,62], the surface resistance to pitting corrosion resistance in chloride solutions is improved, particularly for pHs higher than 4 [44,45,62,63]. The most accepted explanations for this increased pitting corrosion resistance are [64]: 1) nitrogen segregation, in a negative state, on the metal side of the metal-oxide film interface causing repulsion of Cl^- ions [65–67] and 2) the dissolution of nitrogen forms NH_4^+ thereby increasing the local alkalinity of the electrolyte in areas of pitting initiation, inhibiting further pit growth [32,65]. Such corrosion properties together with substantial wear resistance improvements [42,44,49,57] have been the driving force behind the study of expanded austenite for biomedical applications where the aims were twofold: 1) to improve the tribological properties of the cheaper (compared to titanium and cobalt

alloys) biomedical material option AISI 316 [68] and 2) to study the properties of expanded austenite in Ni-free stainless steels [56].

The ‘S-phase’ is often reported to be in a state of stress – however, the origin and extent of the stress is dependent on the method of production of the expanded austenite. For instance, while in S-phase coatings produced by nitriding the unsaturated substrate constrains the saturated, expanded upper layers, resulting in compressive stress [46,69], in ‘S-phase’ layers produced by sputtering an austenitic target, the cause of the stress results from thermal mismatch between the coating and substrate and from the process itself (refer to Section 3.3.3). It has been reported [44,46] (in studies that produced S-phase layers by nitriding) that this stress results in a microstructure which contains a significant number of microtwins, dislocations and slip bands, which indicate plastic deformation.

Upon exposure to high temperatures, typically above 400 °C, the super saturated austenite decomposes into nitrides, which in surface treatment applications is reported to be CrN (as opposed to Cr_2N in bulk material) [53,59] and f.c.c. depleted austenite and/or b.c.c. ferrite [43,59,70,71]. Decomposition is diffusion controlled and hence, the incubation time is dependent on the annealing temperature and can range from a few minutes at a temperature above 500 °C to thousands of hours at a temperature of 350 °C. This metastability of expanded austenite limits its safe application to lower operating temperatures.

For further reading on expanded austenite, the reader is recommended the review conducted by Hanshan Dong [72] which features mostly S-phase produced from plasma nitriding (and plasma carburising). In this thesis, further discussion on expanded

austenite will focus on that produced by the PVD sputter coating method and how the parameters affect the resultant properties of the expanded austenite coating (Section 3.4). However, before getting to this discussion, a review of the sputtering process and parameters will follow in the next chapter.

CHAPTER 3: PVD AND PROPERTIES OF DEPOSITED COATINGS

This chapter introduces the technology used to deposit nitrogen doped austenitic stainless steel coatings – i.e. the process of magnetron sputtering. The process, machine parameters and how these can affect the resulting coating properties are discussed in some depth as such concepts shall be revisited in the later chapters of this thesis.

3.1 PVD processing

3.1.1 Introduction

Physical vapour deposition processes involve the transfer of a material in the form of vapourised atoms or molecules from a source onto a surface upon which they condense. The source material, called the target, may be solid or liquid and the vaporised material may be transported through vacuum or a low pressure plasma environment. The substrate, i.e. surface to be coated, may vary in both size and complexity; examples of industrial applications of PVD coatings include cutting, forming and moulding tools that may require hard and wear-resistant coatings or thermal barrier coatings and decorative coatings for watch wristbands, jewellery and fixtures [73,74].

Deposit thicknesses can vary from a few tens of nanometers to many tens of micrometers and may consist of multilayers, graded compositions, or even free standing structures. Typical deposition rates are 1-10nm/s [73] and may be conducted at temperatures that are low enough not to incur substrate distortion or microstructural changes [75].

There are many different methods for producing the vaporized species from the target, however most of these tend to fall within one of the two categories: evaporation or sputtering. While evaporative techniques involve heating of the source material, in sputter deposition methods energetic particles, typically accelerated ions, physically knock out atoms from the target [76]. Figure 3.1 (adapted from [77] and [73]) gives some examples of different configurations in each of these classes. In this study, further discussion will proceed in the direction of sputtering and magnetron sputtering – i.e. the methods utilized in this work.

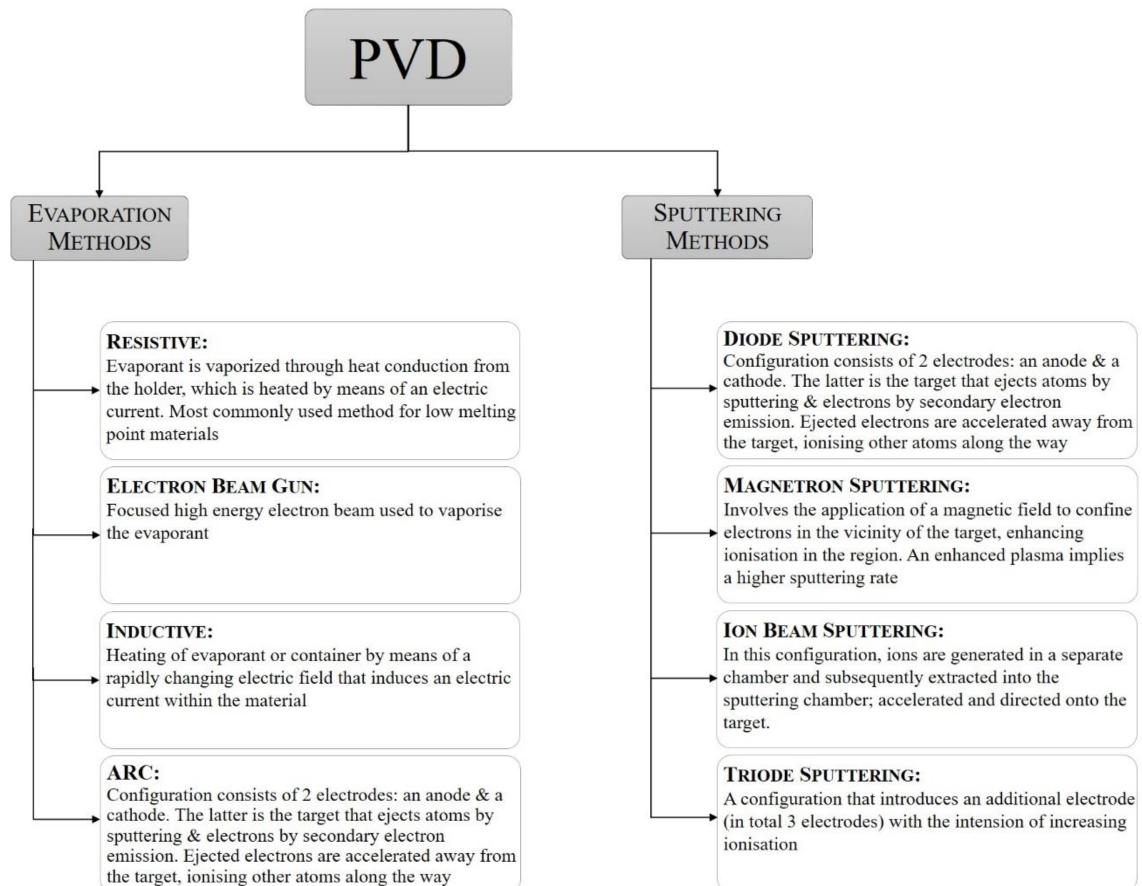

Figure 3. 1 Classification of PVD techniques by target varpourisation methods, compiled from [77] *and* [73]

3.1.2 Sputter deposition

Sputtering is a non-thermal, momentum transfer process whereby target atoms are physically ejected by means of bombardment from an energetic species. Such species can be ions generated from an ion gun in a vacuum environment (such as in ion beam sputtering), or ions from a low pressure plasma of, for example, argon, that are accelerated towards the target by means of an electric field in which the target acts as a cathode. When accelerated ions impinge on the target surface, their momentum is transferred to the target surface atoms, which in turn, collide with other atoms in the target matrix. This collision cascade results in the ejection of recoils, which subsequently deposit on the substrate, forming the coating [73,75,76,78]. Figure 3.2 shows a schematic of sputtering deposition, while Figure 3.3 shows some of the processes that occur following ion impact onto a target surface. As indicated, in addition to sputtering: (i) secondary electrons are ejected from the target. These are accelerated away from the cathode (target), ionising other gas atoms; and (ii) some ions which become neutralised while in transit towards the target, are reflected off the surface.

The chemical bonding of the target atoms and the momentum transferred to them from the bombarding particles during collision, will determine the sputtering yield, which is defined as the ratio of the sputtered atoms to the number of impinging particles [73]. The mass, energy and angle of incidence of the bombarding particles, unlike the target's temperature, are all parameters that can therefore affect the sputtering yield, and consequently the film growth rate. The energy distribution of the sputtered atoms follows a Sigmund-Thompson distribution that generally has its peak around $U_b/2$; where U_b is the surface binding energy of the target atom [79–81].

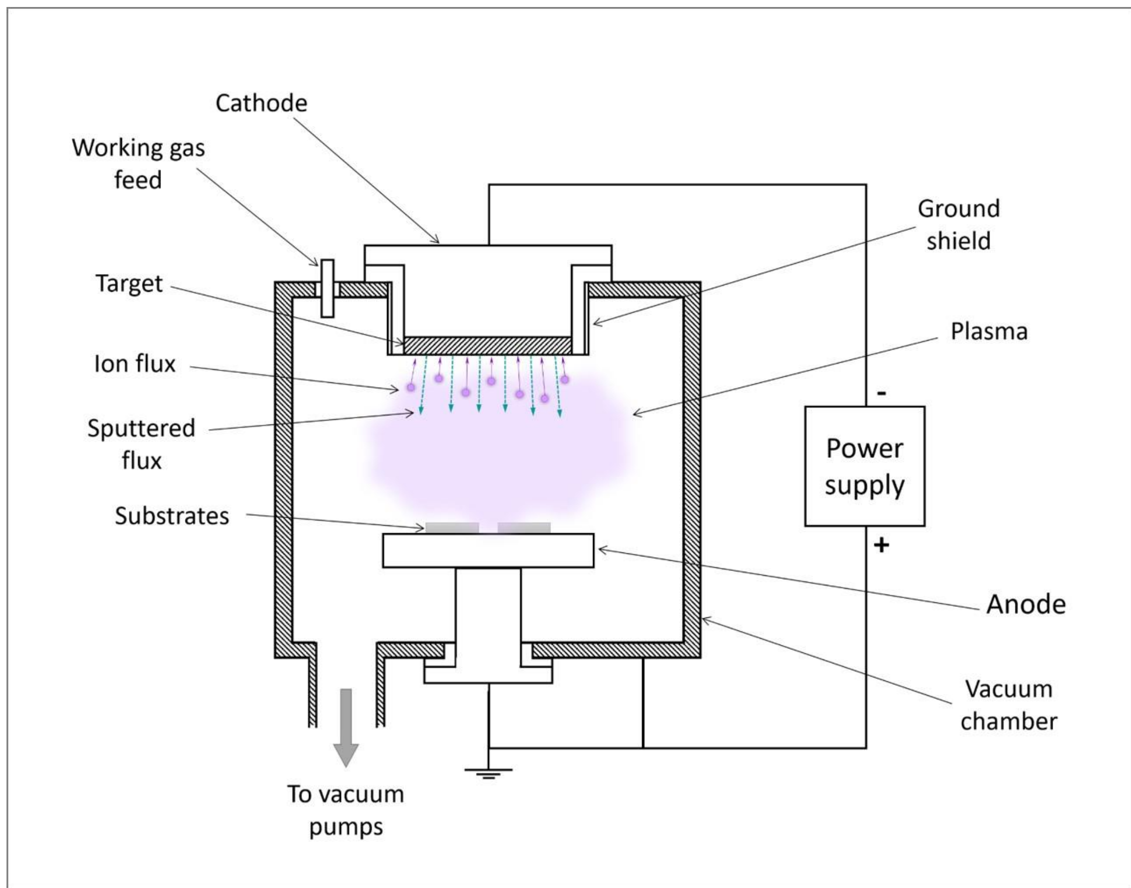

Figure 3. 2 Sputtering principle, adapted from [75]

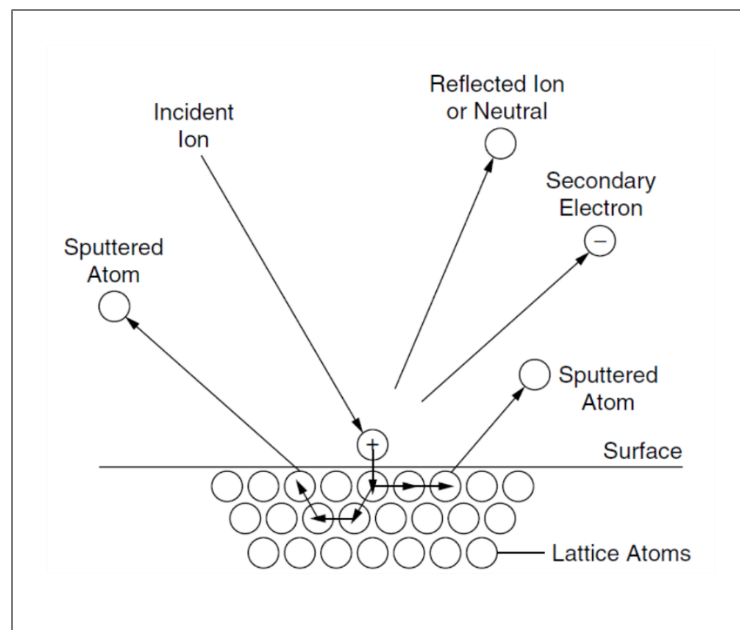

Figure 3. 3 Schematic diagram of some processes occurring after ion impact, adapted from [78]

The substrate tends to gain heat from the condensing atoms that release energy upon their return to solid state as well as from their kinetic energy, especially since sputter ejected atoms have higher kinetic energies than thermally evaporated ones [73]. Plasma effects such as radiation, as well as surface recombination may also contribute to substrate heating. The energy of the bombarding particles, the energy of the ejected particles, the substrate temperature and the pressure in the chamber are all parameters that will determine the morphology and ultimately the properties of the deposited and growing film.

Reactive gases such as oxygen or nitrogen may be used to form compounds with the sputtered atoms (e.g. oxides or nitrides) in what is referred to as reactive sputter deposition. Alternatively, the sputtered target may be a compound itself, or an alloy, and the sputtered material generally consists of the target composition. In some cases however, there might be some loss of the more volatile element from the target alloy or compound, like for example oxygen from a SiO_2 or TiO_2 target. In this particular case, the loss of oxygen can be made up for by introducing some oxygen gas in to the chamber[73].

Almost any material can be sputtered (element, alloy or compound), even when the constituents of the target have different melting points and vapour pressures [73,82]. Doping with gaseous species, chemically grading a coating and the formation of superlattices contribute to the advantages of sputter deposition techniques. In addition, good coating uniformity and the possibility of depositing on large area substrates make large scale productions possible [83]. Among the drawbacks of sputter deposition are possible line-of-sight depositions and the need for a vacuum. Moreover, the process lacks

energy efficiency since a lot of energy (≈90 %) is wasted as heat in the targets, which necessitates target cooling [73].

There are many different configurations for sputter deposition, some of which are listed in Figure 3.1. However, the most widely employed system is that of magnetron sputtering.

3.1.3 Magnetron sputtering

The sputtering rate of magnetron sputtering is made larger applying a magnetic field, parallel to the cathode that confines electrons in the vicinity of the target. For planar targets, magnets (electromagnetic or permanent) are placed behind the target as indicated in Figure 3.4(a) – with one pole placed along the central axis of the target and the other positioned along the outer edges (of the target). The electric and magnetic fields (ExB) act as an electron trap, confining their movement along a loop path ('racetrack') on the surface of the target [78,84].

As the trajectory of the electrons is elongated, the probability of ionising a gas atom is increased, leading to a higher ionisation rate for the same number of electrons [75,85,86]. This denser plasma density in the vicinity of the target not only increases the sputtering rate, but also enables the discharge to be maintained at lower operating pressures (10^{-3} to 10^{-2} mbar) and lower potentials – generally around -500 V instead of -2 to -3 kV [73,78,83,84].

However, as the target area beneath the electron loop is subjected to an enhanced sputtering rate, target erosion is non-uniform – in the shape of a 'racetrack', reflecting the shape of the denser plasma above it. Target utilization is therefore poor (may be as low as 10-30%) and may also result in non-uniform film deposition. However, appropriate target and/or substrate fixtures can be used to overcome these problems [73,86].

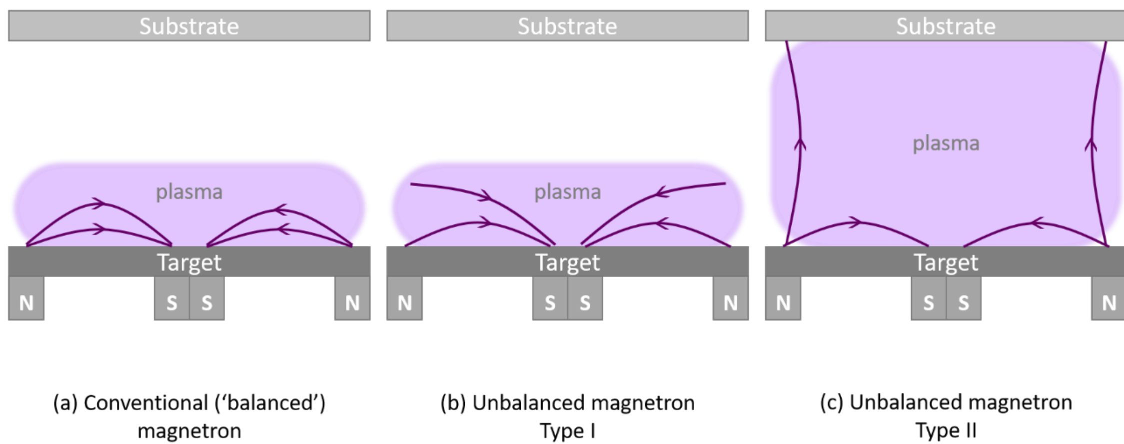

Figure 3. 4 (a) Conventional 'balanced' magnetron; (b) and (c) Unbalanced magnetrons of Types I and II respectively

3.1.4 Unbalanced magnetron sputtering

In an unbalanced magnetron sputtering configuration one of the magnetic poles found behind the target (the central or the outer), is stronger than the other. This creates additional magnetic field lines that remain 'unclosed' or 'unbalanced' and since secondary electrons follow magnetic field lines, undergoing ionising collisions with gas

atoms, the region of high density plasma is extended from close target proximity to a larger region [84,87]. Window and Savvides [88] identified two types of configurations: type I which has the central magnetic pole stronger than the outer set and type II, where the outer magnets are stronger than the inner pole. As shown in Figure 3.4, whilst in type I the additional field lines are directed towards the chamber walls, type II has additional field lines extending towards the substrate. Hence, whilst type I still leaves the substrate in a low density plasma region and has therefore no commercial use, type II enables the substrate to be immersed in a higher density plasma. If a substrate is immersed in the latter, ions from the plasma can be drawn by the substrate bias, providing a means of bombarding the forming film, enhancing its density. [87,89], Unbalanced magnetron sputtering therefore allows greater target-substrate distances and when a multiple cathode system is employed, larger components may be coated [75,87].

A schematic diagram showing several multiple unbalanced magnetron systems is shown in Figure 3.5. In such systems, the number of cathodes is generally even and the adjacent magnetic arrays are set up with opposite magnetic polarities such that electrons are confined to the region in between the cathodes, increasing the plasma density significantly [73,84,87]. Such systems are hence referred to as ‘closed-field’ (Figure 3.5 (a) and (c)). Conversely, if the magnetic fields of multiple magnetrons are not linked, the parallel magnetic fields that would result from two magnets having same poles facing each other (as shown in Figure 3.5 (b)), would direct electrons towards the chamber walls, resulting in a low plasma density in the substrate region. Such systems are referred to as ‘mirrored’ field configurations.

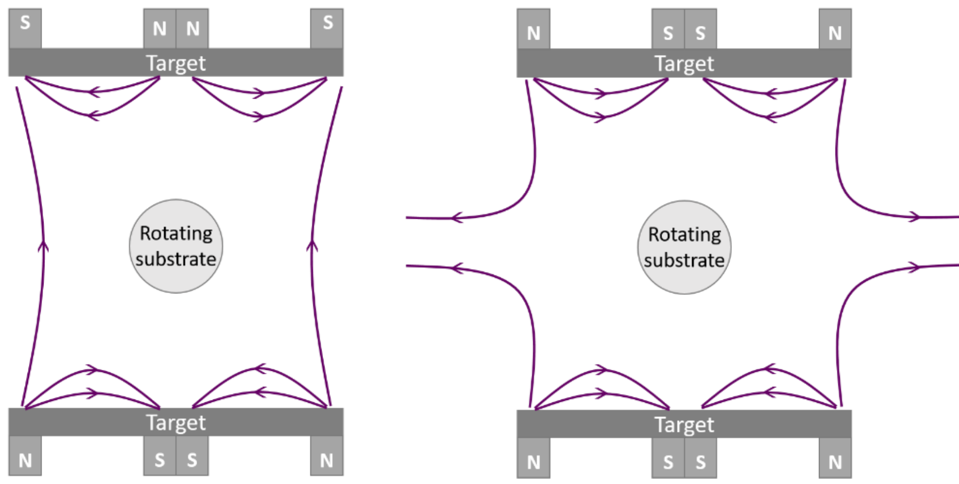

(a) Closed-field configuration

(b) Mirrored configuration

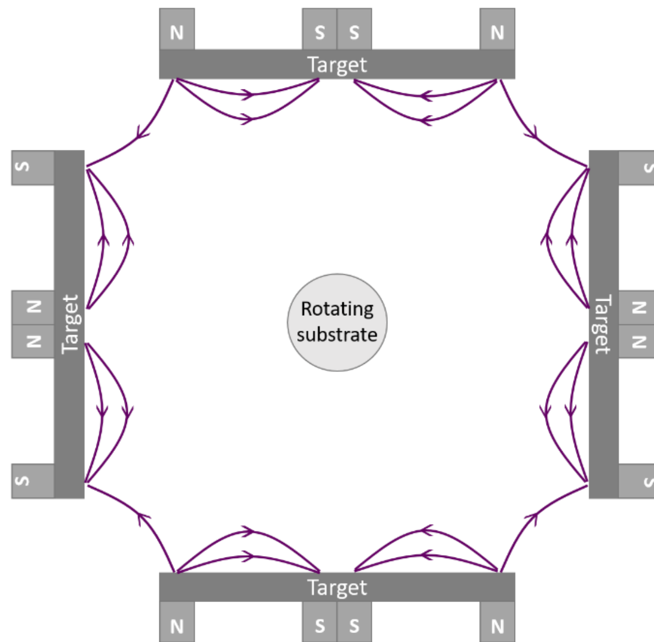

(c) 4-cathode, closed-field configuration

Figure 3. 5 Multiple unbalanced magnetron sputtering configurations

3.2 Process parameters

In this section, the importance and effects of the parameters of an unbalanced magnetron sputtering process, the technique used in this research, will be discussed.

3.2.1 Base pressure

The sputtering process is carried out in a controlled low pressure atmosphere of inert or reactive gas. However, since any residual gas in the chamber is a source of impurity that may get included in the deposited coating, the very first step of any sputtering process is to pump down the chamber to a background pressure that is as low as possible within a reasonable amount of time, before the process gas/es is/are let into the chamber. Typically, the base pressure is below a few milli-Pascals and is obtained by using diffusion, turbo or cryogenic pumps [83,90–94].

3.2.2 Working pressure

In the sputtering process, gas ions in the plasma are accelerated towards the target and from the physics of a collision between two hard spheres, it is known that for maximum momentum transfer between the sputtering ions and the target atoms, the mass of the gas ions must be similar to those of the target [73]. However, in almost all cases, argon gas is used as the working gas because of its low cost, inertness and relative 'safety' (when compared to the health concerns for alternative gases). The working pressure, also called the operating pressure, is the pressure of the argon or gas mixture (Ar/O_2, Ar/N_2,

Ar/acetylene…etc refer to Section 3.2.3, Reactive Sputtering) in the chamber during the sputtering process.

The working pressure will affect the mean free path, (i.e., the distance travelled before experiencing a collision), of the species in the plasma:

(i) Ions being accelerated in the cathode sheath, may become neutralised if another argon atom is travelling close enough. This process, called a symmetric charge exchange collision [85], results in the accelerated ion becoming an atom, and the colliding non-energetic atom becoming an ion. The latter may still gain some acceleration, depending on where in the sheath the collision takes place; however, such collisions result in the bombarding ions having a variety of reduced impact energies.

(ii) On the other hand, the newly formed energetic neutral atom will be reflected off the target and become a source of substrate bombardment [95]. The encounter with further argon ions in their transition from the target towards the substrate will scatter the direction and decrease their energy [96].

(iii) Similar to the energetic neutrals, sputtered atoms will be scattered with collisions, which in addition to decreasing their energy, may result in an oblique component in the depositing flux, affecting the morphology of the deposition [96].

In general, it can therefore be concluded that increasing the pressure will decrease the mean free path of the species in the plasma, which in turn leads to a decreased sputtering rate, and a scattering of sputtered atoms and energetic neutrals.

Many researchers [90,96–99] have studied how the working pressure affects the stress state of the coating and have reported a transition from tensile to compressive stress in various materials as the working pressure is decreased. Film properties like optical reflectance [96], electrical resistance [99] and texture [90] have also been found to be affected by the working pressure, with properties improving with a decreasing pressure. As a consequence of the increased collisional scattering events, as the pressure inside the chamber increases, the deposition rate has been found to decrease [90,100].

3.2.3 Reactive sputtering

Reactive sputtering is the deposition of a compound film from a metal, alloy or compound target in the presence of a reactive gas, such as nitrogen or oxygen, in the chamber [101]. This method enables the deposition of ceramic coatings such as alumina and TiO_2 – that are used for their dielectric properties, and titanium nitride, a hard wear resistant coating.

Typical reactive gases (e.g. nitrogen and oxygen) have low atomic masses (14 and 16, respectively), and are therefore not effective in sputtering heavier atomed targets such as aluminium, chromium etc. (atomic masses 27 and 52, respectively). Hence, heavier inert gases (e.g. argon) are still required to conduct the sputtering [73]. However, Lilejeholm [83] pointed out that different gases in the chamber may sputter different target constituents with different efficiency. For instance, in the deposition of aluminium-boron-nitrogen based films, ions from the reactive gas nitrogen sputter the lighter boron

in the target more efficiently than argon ions, while the aluminium in the target is sputtered more efficiently by the argon ions.

In some situations where the sputtered target is a compound itself, some loss of the more volatile element from the target, such as oxygen from an indium tin oxide (ITO) or from a silicon dioxide (SiO_2) target may occur [73]. This loss of oxygen can be made up for by having some partial pressure of oxygen in the chamber. This practice is referred to as quasi-reactive sputtering.

Sometimes the reactive gas does not react to form a compound, but is merely incorporated into the depositing coating, much like any other contaminants that can be found in the chamber environment. Examples of this kind of doping are nitrogen [59] or carbon [98] doped stainless steel coatings. In these cases, the nitrogen or carbon content in the coatings increases with its percentage in the chamber atmosphere.

A reactive gas in the chamber may react with the target forming a compound top layer. This is called target poisoning and it is largely to be avoided especially when the forming compound is non-conductive (such as an oxide) as it can lead to a charge build-up and subsequent breakdown, resulting in an unstable process [83]. Target poisoning is further discussed in Section 3.2.5 (Pulsed Magnetron Sputtering), since applying a pulse to the target is one solution to this problem.

3.2.4 Target power

After the chamber is pumped down to the base pressure and backfilled with the working gas to the desired working pressure, the plasma is struck when power is given to the target. The current-voltage characteristic of a plasma discharge is complex, comprising of several different current stages as the voltage is increased: the collection of free electrons present in the chamber (ohmic conduction and saturation stages); the generation of electrons (and ions) resulting from impact ionisation of neutral gas atoms during the acceleration of electrons towards the anode (Townsend regime); emission of secondary electrons from the cathode after impact by sufficiently energetic ions (breakdown, followed by normal and abnormal glow regimes); thermionic electron emission from the cathode (arc regime). Most DC sputtering takes place in the abnormal glow regime, because this stage is where the highest sputtering rate occurs. (For further detail about these different stages, the reader is encouraged to refer to [76,85].

During the abnormal glow stage, a DC magnetron has been described as following the empirical current-voltage relation: $I \propto V^n$, where n is typically between 5 – 15, depending on the performance of the magnetic electron trap (magnetron design and magnetic field) [85,95,102]. Experimental parameters such as the gas-target combination, pressure and gas density would also affect n and the proportionality constant. This equation predicts small changes in voltage for large current changes. However, not all magnetron sputtering systems have been observed to follow this relationship; for instance, the work by Depla [103] exhibited a better fit to an alternative equation proposed by Westwood [104]: $I = \beta(V-V_0)^2$, (where V_0 is the minimum voltage required to maintain the discharge and β a measure of the steepness of the curve) than to the former equation ($I=kV^n$).

In any case, a power increase in a magnetron sputtering system translates to an increase in both current and voltage. An increase in the current of a system, means that more electrons are present in the plasma. The higher number of electrons, in turn, means a higher ionisation rate (higher plasma density), implying that a greater number of ions is accelerated towards the target causing sputtering, which results in a higher deposition rate. On the other hand, an increase in voltage means that the ions are being accelerated to higher velocities and will have higher kinetic energies upon impact at the target surface. This increase in kinetic energy upon impact translates primarily in a higher sputtering yield (number of atoms being sputtered per incoming ion), i.e. it results in a higher deposition rate. Also, an increase in the velocities of the sputtered atoms is observed with an increase in voltage, however, this effect is not as strong as the increase in the sputtering yield [105]. As a result, many studies, for a variety of materials have observed a linear increase of deposition rate with power (aluminium [90], tungsten boride [106], titanium nitride [107], cadmium oxide [93], molybdenum [108], nickel [109]). Since a large fraction of the energy incident on the target is lost in heating, the limitation for maximum power is often the point at which the target incurs melting or damage [101].

Explaining how the target power affects the film properties is more complex. First and foremost, it affects the morphology of the forming film due to the amount of energy given for diffusion to the condensed adatoms to form the structure. This is discussed further in Section 3.4.1 that discusses the structure-zone models. Secondly, it affects properties like surface roughness and stress – however, the manifestation of this affect is not explicit as it depends on other parameters during the deposition. For instance, in the work of Liu [106], as the target power increased and the depositing atoms had more kinetic energy, the film surface roughness at the substrate increased as a result of resputtering of previously deposited target atoms. The planes of higher densities were most susceptible

to this resputtering leading to a change in orientation. Moreover, in this tungsten boride deposition, the lighter element boron was preferentially etched, leading to a change in composition with increasing target power. The stress transitioned from tensile to compressive with an increase in target power. On the other hand, in the study of Iriarte [90], as the target power increased, the corresponding increase in deposition rate meant that less oxygen inclusions could be found in the deposited coating. As oxygen inclusions in aluminium nitride films are detrimental to stress and structure (different size and chemistry leading to lattice distortion and compressive stress), with the decrease in oxygen contamination that was brought about by increase in target power, the surface roughness improved and the highly compressive stress decreased.

3.2.5 Pulsed magnetron sputtering

When conducting a reactive magnetron sputtering process, there is a risk of having regions on the target that get coated. Particularly in the deposition of electrically insulating materials, such as aluminium oxide [91,110] or aluminium nitride [83], the target's surface (aluminium) can react with the reactive gas in the chamber (e.g. oxygen, nitrogen) and form an insulating layer on the target surface. Such 'poisoned' parts / layer, prohibit efficient charge transport causing a charge build up until breakdown occurs through arcing. In addition to a drastically reduced deposition rate of a poisoned target, the onset of arcs makes the process unstable and unpredictable which leads to fluctuations in power regulation and adverse effects on the coating's structure and properties. As a solution to this problem, the target is pulsed in such a way that during the time the pulse is 'off', the accumulated voltage is dissipated before arcing can occur

[83,91,110]. There are two pulsing modes [92]: unipolar, where the cathode is earthed during the pulse 'off' period, or bipolar, where a positive voltage – called reverse voltage, which is usually between 10-20% of the sputtering voltage is applied to the target. Such a system of operation is often referred to as pulsed magnetron sputtering (PMS).

The main characteristics of the pulsed waveform are: the frequency, the duty factor and the reverse voltage value (assuming a bipolar mode) – all of which are represented in the theoretical waveform in Figure 3.6 (a). The duty factor, also called the duty cycle, is the ratio of the time when the pulse is 'on' to the time of the whole cycle. In practice, the waveform would experience some overshooting at both positive and negative ends of the voltage pulse, as shown in Figure 3.6 (b) which shows an oscilloscope trace of a target (aluminium) voltage operating at a frequency of 100 kHz, 80 % duty factor and 20 % reverse voltage, as measured by Kelly [110].

Some studies [91,110] of Al_2O_3 coating depositions have shown that rather than the frequency used, the duty cycle is the more important factor for an arc-free process. This is because the 'off' time must be long enough to dissipate the accumulated charge. However, since during the 'off' time no deposition takes place, the duty factor must be set at the highest value possible for an arc-free deposition. On the other hand, the coatings were rather insensitive to the frequency employed.

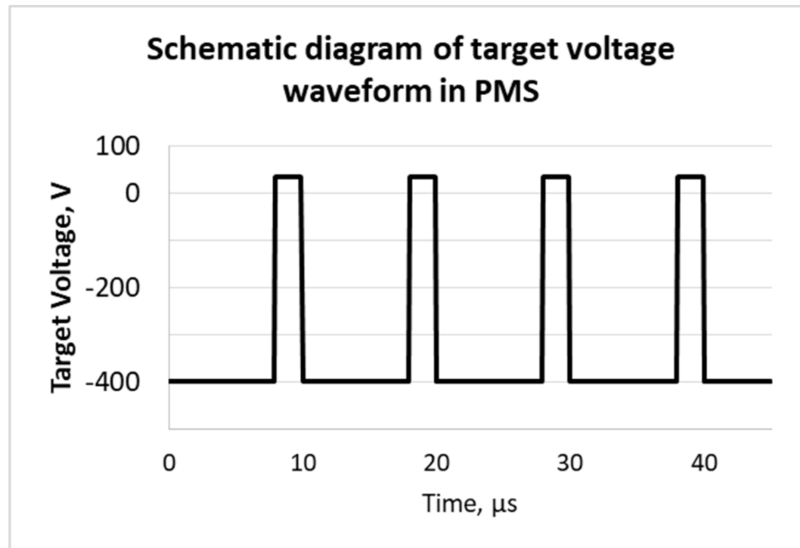

(a)

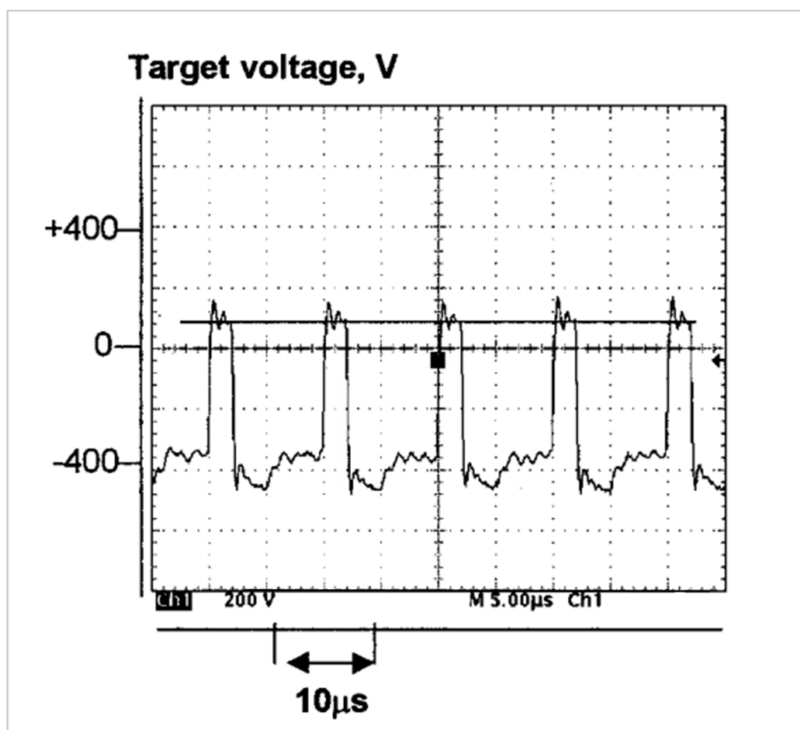

(b)

Figure 3. 6 (a) Schematic diagram of a target voltage waveform in PMS and (b) an actual oscilloscope trace of a target voltage waveform in PMS operation, from [110]. *In both cases the frequency was set to 100 Hz with a duty cycle of 80 %.*

It has been shown [92,111] that pulsing the target in an unbalanced DC magnetron system results in changes to the plasma conditions and amongst other things, the energy of the ion flux (Ar^+ and post-ionized sputtered target atoms) arriving at a floating substrate correlates to the target voltage waveform. Hence, while in continuous mode the ions in the plasma bombarding the substrate have a certain constant value; in the pulsed mode, ions originating during the reverse voltage or overshooting stages have higher energies, resulting in a higher energy delivered per deposited atom. Some studies (on Ti and TiO_2 [111,112]; ZnO:Al [113]; TiN [114]) have investigated the effect of such higher energy fluxes by increasing the frequency of the pulsed target. While the earlier studies reported minimal effects on the crystallographic structure and hardness (hence probably the reason why frequency insensitivity was sometimes reported), in a more recent study by the same authors [114], it was found that the hardness increased with target pulsing frequency for TiN coatings. However, even when the crystallographic structure and hardness remained unchanged, other properties such as adhesion (in TiO_2 and TiN films [113]), wear resistance (of TiO_2 coatings [111–113]), lower friction coefficient (TiN coatings [113,114]) and optical properties (of TiO_2 coatings [111–113]) were found to be affected by the high energy fluxes imparted by the plasma in a pulsed system. Benegra et al. [115], also reported an increase in compressive stress when the target was pulsed for TiN coatings.

In conclusion, in addition to solving target poisoning issues, pulsing can be used to improve the properties of the coatings by increasing the pulsing frequency, which in turn provides a higher ion energy flux bombarding the substrate. On the other hand, the duty cycle, must be kept as high as possible, so long as it is sufficient to dissipate any accumulated charge on the target.

3.2.6 Target-to-substrate distance

Like the working pressure, the target-to-substrate distance affects the number of collisions sputtered atoms encounter before being deposited. With distance, the probability for collision/s increases and since collisions scatter the atoms, both the energy and the directionality of the condensing atoms are affected [83].

3.2.7 Substrate bias

When a negative bias is added to a substrate, ions in the plasma (generally, Ar^+) are accelerated towards the substrate, resulting in an ion bombardment effect. Based on many experimental observations and on a variety of materials, authors unanimously agree that biasing the substrate causes the stress in the deposit to trend towards the compressive state, with an increase in the bias (Al [116]; Cr [117]; ZrO_2 –Y_2O_3 [118]; Ta [119]; Nb [99]; TiN [115]; various materials [120]). Researchers have considered several mechanisms to justify the observed phenomena. These included impurity (argon and / or oxygen) entrapment, phase change, and momentum-transfer-induced displacements from bombardment effects (such as target atoms implanted into interstitial and grain-boundary sites). However, it seems there is no clear explanation of which mechanisms are responsible for this increase in compressive stress.

Some authors [117,119–121] have observed that while the compressive stress in the deposit increased with substrate bias, the stress saturated to a maximum, and in some cases, this was followed by a decrease. Some authors [99,119] have attributed this to the

onset of plastic deformation that would result in stress relief in the deposits. Other authors have noted that following this maximum stress level, bad adhesion that caused peeling of the coating was observed [118]. Other than the stress in the deposit, a bias applied to the substrate may result in a changes in other properties such as preferential orientation, thickness and hardness. However, the conclusions on these aspects vary. For instance, while some studies have observed changes in preferential orientation with variation in the substrate bias [97,107,116,119]; others [117], did not. Similarly, while Darbeida et al. [122] and Freeman et al. [123] observed no changes in the hardness of AISI 316L and CrN films, respectively, Sproul et al. [107] found that it increased with substrate bias in TiN films. Changes in thickness were only reported by Freeman et al. [123] and it decreased significantly with the addition of a bias. The authors suggest that the reduction in thickness is the result of re-sputtering.

3.2.8 Substrate pulsed bias

Not only can a negative bias be applied to a substrate, but this bias can also be pulsed, in a similar way that the target it pulsed in PMS. There are very few works that have studied how this affects the process and the resulting deposits, but the main findings can be summarised as follows:

Firstly, an increase in the ion current drawn at the substrate is reported as the substrate bias increased [121,124–126]. The work by Kelly et al. [124] showed that while the ion current drawn by a DC bias tended to increase until a saturation point, when the bias was pulsed, there was no saturation. The authors suggested that this could be the result of a

second plasma forming on top of the substrate surface. Moreover, instantaneous measurements have revealed that while during the pulse-on period, low ion currents were drawn at the substrate, during pulse-off, large electron currents were drawn. These currents led to an increased substrate heating rate when compared to DC biasing. Increasing the frequency of the pulse led to further increases in the ion current, as shown in Figure 3.7.

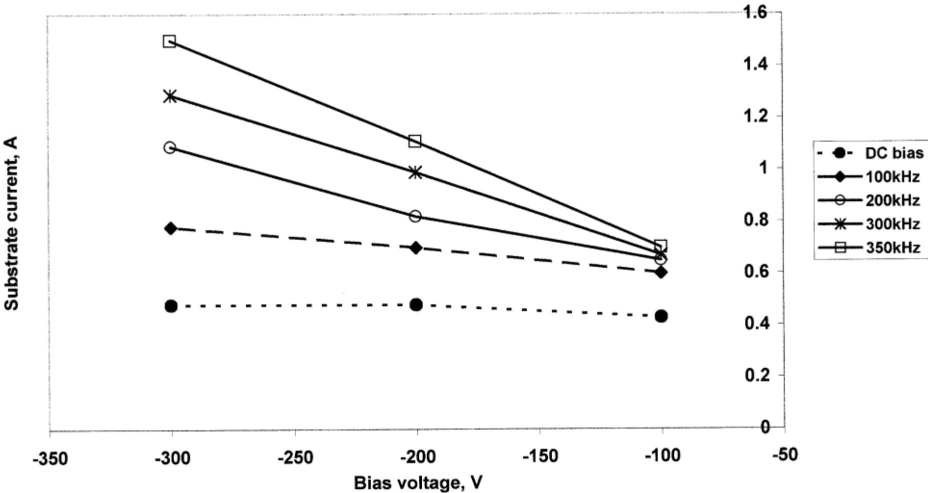

Figure 3. 7 Variation in substrate ion current with pulse frequency & bias, adapted from [124]

Secondly, as pulsing increased the flux of bombarding ions (as evidenced by the ion currents drawn at the substrate, e.g. Figure 3.7) and hence the energy imparted on the growing films, the resulting properties of the coatings changed accordingly. For instance, pulsing the substrate was reported to alter the structure and texture of the deposits in various material systems (TiO_2 [124]; CrN [123]; TiN [114,125,127]) – often with the structure becoming more densified and more highly textured with further increases in the

pulsed substrate bias. Compressive stress [123,125], critical loads in scratch testing [114,123,125] and hardness [114,123,125,127] have all been reported to increase with pulsed substrate biasing. However, in some studies an improvement in mechanical properties (e.g. hardness and adhesion) was observed only until a certain bias value, after which the properties deteriorate due to the 'cracks' or 'defects' in the films [125,127].

The work of Audronis et al. [126] on the deposition of chromium oxide (Cr_2O_3) using unbalanced magnetron sputtering, involved pulsing at both the target (PMS) and substrate. Their work reported the voltage waveforms at target and substrate for two different configurations: when the frequencies were synchronised and when they were relatively different. It was found that having an asynchronous frequency configuration resulted in a significant enhancement of the process and the consequent coating structure. The authors suggest that this was because the plasma was enhanced and because all the species in the plasma: electrons, positive ions and negative ions, (contrary to the situation in synchronized frequencies), contributed in modifying the growth conditions of the film.

3.2.9 Substrate temperature

Control of the substrate temperature by external heating provides another means of supplying energy to the condensing film. Keeping the substrate at an elevated temperature therefore influences the mobility of the atoms, dislocations…etc, that can result in stress relief, texturing [47] and phase change [70]. The substrate temperature can also affect the amount of reactive gas (e.g. nitrogen) retained by a coating, which tends to decrease with an increase in substrate temperature [53,128].

The substantial effect of the substrate temperature on the coating structure will be revisited in Section 3.3.1 – where the resulting coating structure is related to the ratio of substrate temperature over the melting temperature (i.e. the 'homologous temperature') of the film material (in Thornton's structure- zone models).

Final comments on process parameters:

There are other parameters that can affect the film and its properties – for instance the angle of incidence of the flux (normal incidence or otherwise, rotating substrates), the geometry of the equipment (cylindrical cathode and anodes vs planar) and the working gas species. However, since these parameters are generally kept constant within any setup, a discussion of variation in these parameters was deemed beyond the scope of this study.

One final note is that, while this section has attempted to explain the effect of most of the parameters in the equipment, very often these parameters are interlinked and a balance between conflicting effects would need to be established. For instance, consider the work of Liu et al. [106] on tungsten boride depositions, that discusses how the working pressure affects adatom mobility at the substrate surface, which in turn determines the diffusion rates occurring at the surface and hence, the preferential orientation. While decreasing the working pressure means that the condensing atoms will have a higher mobility, excessive energy resulted in re-sputtering of the deposited atoms on the densest planes – affecting the resultant orientation and deposition rate. Moreover, re-sputtering was higher for the lighter element, boron, resulting in compositional

changes. On the other hand, increasing the working pressure increased the scattering rate which also decreased the deposition rate. Scattering was also higher for the lighter element (boron), again affecting the composition. Alternatively, the energy of the ions arriving at the substrate surface could be reduced by decreasing the target power, which however, also decreases the deposition rate. This point shall be revisited again when discussing the stress in the films in the Section 3.3.3.

3.3 Coating Characteristics

3.3.1 Structure-zone models

Structure-zone models are used to categorize the morphologies of deposited films qualitatively. During deposition of a coating, the incident atoms can undergo different processes: i) shadowing – as a result of surface roughness and direction of flux, ii) & iii) surface or bulk diffusion – depending on the respective activation energies and iv) desorption – depending on sublimation energy [129]. Since in many metals, these energies are related to each other and proportional to the melting temperature, in the structural zone models developed by Movchan and Demchishin in the 1960s and later modified by Thornton [130], the ratio of the substrate temperature during deposition to the melting point of the coating (T/T_m), is used to obtain an indication of the dominant acting processes and hence a prediction of the resulting structure [129].

While Movchan and Demchishin classified the possible resulting structures of coatings deposited by electron beam evaportaion into three zones based only on this ratio,

Thornton [130] considered also the pressure in chamber during deposition, thereby adding an axis to the model. Thornton's work featured thick (~25 μm) DC sputtered coatings from various targets; primarily copper and aluminium alloys, but also including coatings from molybdenum, chromium, iron and titanium. The resultant modified model (Figure 3.8), in addition to being more accessible to researchers, included a transition zone (Zone T) between the first and second zones previously defined by Movchan and Demchishin. The primary axis remained the same, i.e. the ratio of substrate temperature over the melting temperature of the coating (T/T_m) (homologous temperature).

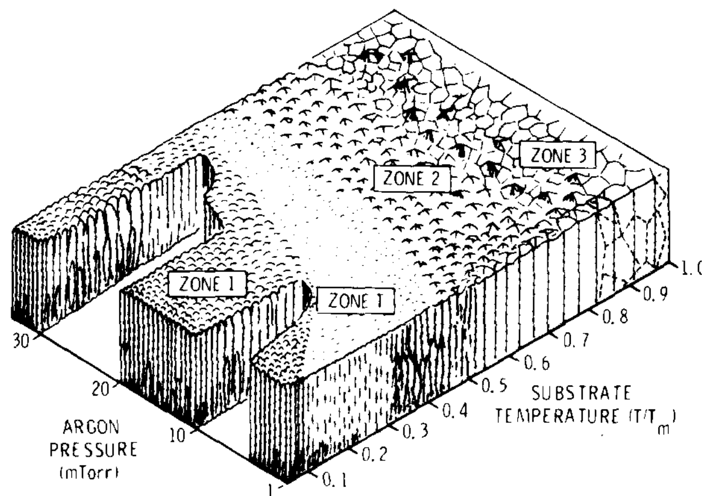

Figure 3. 8 Thornton's structure-zone model [96,130]

Thornton [130] discusses the effect of temperature and working pressure on the resulting morphology of the coatings. In other words, Thornton's structure-zone model is based on the energy given to the film during condensation as a result of these properties. However, as discussed in Section 3.2, there are other means of increasing adatom energy

which could result in a change in structure. For instance, by increasing the target power Song et al. [94] changed the structure of (Al,B)N coatings from amorphous to crystalline. Other parameters that could affect the resulting morphology are biasing the substrate and pulsing, that alter the bombardment flux properties, and hence the energy delivered to the growing film.

Zone	Description
Zone 1 $T/T_m < 0.1$	This zone is characterised by a dark grey surface and a porous columnar structure of tapered crystallites and voids. At low T/T_m, there is little energy for mobility leading to growth in the direction of the incoming flux and shadowing results in tapered crystallites and voids. This zone extends over higher T/T_m as the argon pressure increases in the chamber.
Zone T $0.1 < T/T_m < 0.3$	With increasing T/T_m, diffusion increases and the structure changes to a dense fibrous structure where the grains increase in width and length with further increases in T/T_m. Zone T tends to form on smooth substrate surfaces with a perpendicular flux incidence that minimizes shadowing and results in a surface that is relatively smooth and fine-domed, thereby exhibiting a high reflectivity [96].
Zone 2 $0.3 < T/T_m < 0.5$	Zone 2 consists of columnar grains that extend through the coating thickness. Surface mobility is substantial leading to proper grain boundaries and faceted surfaces.
Zone 3 $T/T_m > 0.5$	The structure remains columnar, but the surface becomes smooth with flat topped grains and grooved grain boundaries.

Table 3. 1 The zones in Thornton's structural zone model

Based on similar arguments, Anders [131] proposed some modifications and an extension to the classic Thornton structural zone model. In this model, the homologous

temperature (T/T_m) axis is replaced by a generalised temperature T* that adds any temperature shift caused by the potential energy (e.g. heat of sublimation and ionization energy) of the arriving particles to the homologous temperature ($T^* = (T/T_m) + T_{pot}$). The second axis replaces the working pressure with a normalised energy, E*, in logarithmic form. It represents the displacement and heating caused by the kinetic energy of bombarding particles (arriving atoms, ions accelerated by biasing, energetic neutrals etc). The third axis represents thickness, t*, which is used to indicate effects such as densification and resputtering effects. Figure 3.9 shows this modified and extended model.

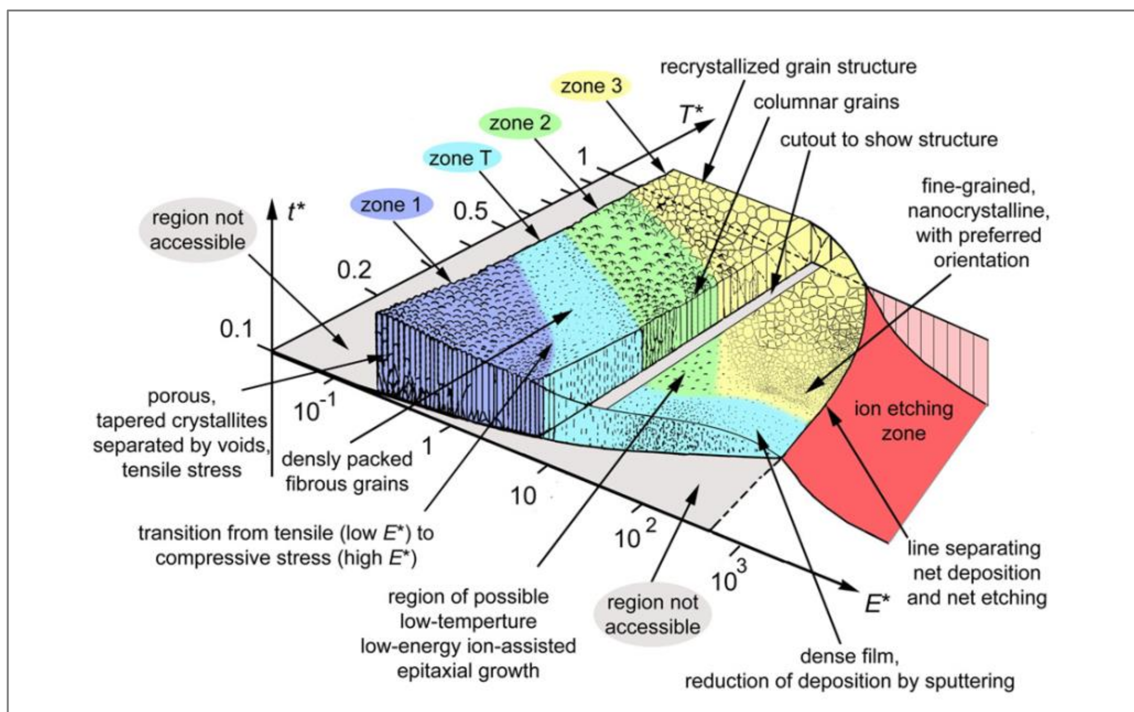

Figure 3. 9 Anders' extended and modified structure zone diagram, applicable to energetic deposition [131]

3.3.2 Coatings from alloy or compound targets

As discussed earlier in section 3.1.2, the sputtering yield depends, amongst other things, on the chemical bonding of the target atoms. Hence, a pure metal will be sputtered at a higher rate than a compound, as a consequence of the stronger chemical bonds in the latter. Sometimes compounds lose some of the more volatile constituents, such as oxygen when sputtering from a TiO_2 target, and unless this oxygen is replenished by additional gas in the atmosphere (reactive sputtering), the resulting film composition may differ from that of the target [73].

Similarly, when sputtering alloys and mixtures of materials, differences in the sputtering yields of the constituents can lead to films of a different composition than that of the target. Conversely, when the sputtering yields of the mixtures are similar, such as in the sputtering of stainless steels, despite the multi-element compositions of the target, the resulting coatings have been reported to have compositions that were very close to that of the target [132,133] or with small deviations, such as less than 6% [59,70].

3.3.3 Stress

Irrespective of the process employed, stress is to a certain extent inherent in every deposition process [96,134]. The stress can be tensile or compressive and in excessive quantities can result in cracking, buckling or other failure of the coating. However, even in moderate quantities, stress affects certain properties like the optical, electrical and magnetic characteristics of a film [96,135–137].

The resultant stress in a film is composed of the thermal stress and the intrinsic stress. The thermal stress is caused from a difference between the thermal expansion coefficients of coating and substrate. On the other hand, the intrinsic stress is process sensitive and is the accumulation of chemical and structural flaws formed during condensation of the film [96,135].

Thermal stress

For thin films (film thickness < 10^{-4} of the substrate thickness), the thermal stress induced by the different thermal expansion coefficients of different film and substrate materials can be found from Hoffman's [138] equation (3.1) that was later simplified by Thornton and Hoffman [96] to equation (3.2) that neglects the Poisson's ratio effect.

$$\sigma_{th} = \frac{E_f}{(1-\nu_f)}(\alpha_f - \alpha_s)(T_s - T_a)$$

Equation 3.1

$$\sigma_{th} = E_f(\alpha_f - \alpha_s)(T_s - T_a)$$

Equation 3.2

In these equations E_f and ν_f are the Young's modulus and Poisson's ratio of the film, α_f and α_s are the average coefficients of thermal expansion for the film and substrate, T_s is the substrate temperature during deposition and T_a is the temperature at which the stress value is being calculated, for e.g. room temperature, or the temperature of the application. A positive value for σ_{th} represents a tensile stress while a negative value corresponds to a compressive one.

Applying this expression to two practical examples: (i) chromium film deposited on ABS for an automotive application where the application temperature is 82 °C and (ii) an aluminium coating on a silicon wafer substrate that is deposited at 150 °C and subsequently annealed at 400 °C, Thornton and Hoffman [96] show how the thermal stresses predicted (tensile 0.16 GN/m^2 and compressive 0.26 GN/m^2, respectively) exceed the yield strength of the coatings and can therefore fracture the coating-to-substrate bonds.

Intrinsic stress

In the absence of energetic particle bombardment, a porous, sub-bulk density microstructure under a tensile stress can be observed in sputtered films [96]. Among the explanations given in literature for a resulting tensile stress are:

i) A phase change: The internal stress developed could be the result of differences in density between a metastable phase and the subsequent stable state phase formed in a growing film. In the work of Buckel [139], gallium,

bismuth, tin and lead when condensed at very low temperatures retain a frozen-in amorphous phase without stress. At higher deposition temperatures, a microstructures crystallise. If the crystallised stable phase has a higher density than the metastable phase, then a tensile stress would result – observed for tin and lead. If, on the other hand, the stable phase exhibited a lower density, as for gallium and bismuth, a compressive stress would be observed. The author observed compressive stresses only for gallium and expressed that while this model may explain some of the tensile stress observations, its applicability is not certain.

ii) Structural re-arrangement: In a study that involved 15 different evaporated metals, Klokholm and Berry [140] proposed that the intrinsic stress resulted from the annealing and consequent shrinkage of the condensing material. The authors describe the condensing atoms as 'disordered material' with a structure and density that was in between that of a perfect crystal and that of a highly defective supercooled liquid. As this disordered material was buried under subsequent condensing layers, thermally activated restructuring, i.e. annealing, took place to form a more ordered structure (with a higher density). This annealing resulted in a shrinkage that is constrained by the substrate, thereby giving rise to a tensile stress in the film. In other words, the intrinsic tensile stress is caused by a structural rearrangement of the growing film and its magnitude reflects the initial disorder on the surface. The authors also showed how this stress was highly temperature dependent and decreases with increasing deposition temperature, when the annealing rate was much higher than the deposition rate and thermally activated processes such as vacancy movement and grain growth became more probable. Conversely, when the

deposition rate was much higher than the annealing rate, which occurs when the deposition temperature was low, the observed stress was high. Sun et al [141] and Windischmann [142] applied this model to rf sputtered films and ion-beam sputtered films, respectively.

iii) Grain boundary relaxation [135,143]: In this model, the stress is considered to develop as a consequence of two adjacent growing crystals that come into contact. While randomly oriented, isolated crystals grow on a surface, interatomic forces act across the voids in between the crystals. These attractive forces cause a grain boundary relaxation but since the crystals are constrained by their adhesion to the substrate, a tensile stress results in the forming film.

On the other hand, many researchers have observed compressive stresses in their films and these have generally been explained by one of the two main theories discussed below:

i) Impurities: Inclusions can cause lattice distortion through the incorporation of differently sized atoms in the film, through reactions at the grain boundary that may result in a phase of different molar volume, or through grain surface energy reduction [135]. The inclusion of oxygen, water vapour and other impurity particles [137,144] was found to provide a compressive stress component that in, for example, evaporation processes can be used deliberately to decrease the otherwise tensile stress. Other studies [145] have

reported that inert gas inclusion was the source of compressive stress. However, some authors have expressed disagreement [96,136,146] for this explanation as a source of compressive stress and instead favour the atomic peening model described next.

ii) Atomic peening: D'Heurle [147] proposed that the origin of compressive stresses could be the result of a shot-peening-like action conducted by the depositing atoms onto the surface. Since in sputtering, the depositing atoms arrive at the substrate surface with considerable kinetic energy, it was suggested that the atoms might be entering small interstices that would otherwise remain vacant and thereby causing a compressive stress. Neutralised gas ions reflected off the cathode also arrive at the substrate surface with sufficient energy to contribute to this bombardment of the growing film. In their experiments Hoffman and Gaerttner [146] have ion peened evaporated chromium films during deposition using an independent beam of argon or xenon ions. This study attempted to analyse the effects of ion bombardment on the growing films – a process which generally occurs in sputtering systems – by independently controlling the ion bombardment stream. The results showed that otherwise tensile films turned into compressively stressed ones with an increase in ion bombardment dosage and that the process was momentum transfer controlled. This model remains one of the mostly widely employed to explain compressive stress in thin films.

Effect of parameters on stress

The overall stress state of a film would be the combined effect of several of the mechanisms discussed above. This means that the stress state could be tailored to the particular application – for example, it could be minimized or it could be made compressive to improve wear resistance and hardness [96,97,148]. Ultimately, the parameters chosen during the process will determine the energy supplied to the growing film and consequently the stress state. Table 3.2 below gives some examples of how stress changes with substrate bias, working pressure and target power. Furthermore, it should be noted that while applying a temperature to the substrate can relieve intrinsic stresses, it could increase the possibility of thermal stress issues.

Parameter	**Direction of stress with parameter increase**	**References**
Substrate bias	Compressive	[97,98,116–120,145]
Working pressure	Tensile	[90,96–98,136]
Target power	Compressive	[108,145]

Table 3. 2 Parameter effect on stress

3.3.4 Adhesion

In a film-substrate system where the film is stressed, the compatibility of the system means that an equal, but opposite stress acts in the substrate [96,134,138]. Moreover, if the system is not constrained, the substrate will bend to compensate for the bending moment imposed by the film. However, excessive mechanical stress can lead to a de-adhesion of the film from the substrate [73,134,149,150]. Depending on the nature of the stress, whether it is compressive or tensile, isotropic or anisotropic, different failure modes can be observed, as shown in Figure 3.10 that is adapted from [73]. In cases when the film's adhesion to the substrate is high or when the strength of the substrate is low, the fracture may occur in the substrate and not at the interface.

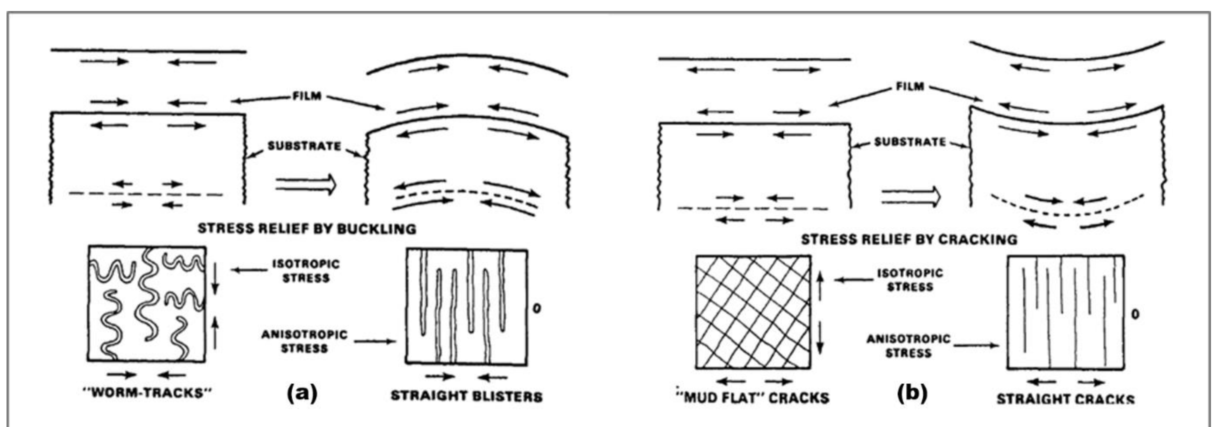

Figure 3. 10 Manifestations of (a) Compressive and (b) Tensile stress, adapted from [73]

Delamination sometimes results in the ‘curling’ of the film away from the substrate. Laugier [151] suggests that this is the result of a residual thermal stress profile within the film, since the intrinsic stress tends to be constant.

Despite the critical importance of adhesion, there is no broadly applied method for quantitatively measuring adhesion and any available tests provide only comparative measurements [73,134]. Amongst the tests available for adhesion characterization are those that apply tensile or shear stresses to the interface, or the scratch test, where the critical load required to scratch off a film from a substrate is measured.

In order to avoid the deleterious effects of excessive stress on film adhesion, the following suggestions have been proposed:

- Limiting the film thickness [152]
- Changing the deposition technique or parameters [152]
- Stress relief after deposition [150]

3.4 Sputtering of austenitic stainless steel coatings

Unlike nitrogen thermochemical diffusion treatments, research on sputtered austenitic stainless steel coatings doped with nitrogen is very limited. As a consequence, the data is very sporadic and with few replications of the findings, leading to a lack of clear understanding on how the parameters affect the coating properties. Incidentally, the recent studies [47,53] seem to have identified this need and tried to investigate some of

the parameters involved in sputtering. The following section attempts to collect the available data related to sputtering parameter effects and the generic properties of nitrogen-doped austenitic stainless steel coatings.

In nitrogen doped austenitic depositions produced by sputtering, the nitrogen concentration (as well as those of other elements) typically has no gradient: it is constant [48] and perhaps the parameter effect that is common and reported in all studies is that nitrogen content in the depositions increases linearly with nitrogen percentage in the argon-nitrogen gas mixture [47,48,52,53,59,60,133], as shown in Figure 3.11. Similar to the expanded austenite obtained from nitriding, XRD peaks shift to lower angles with increasing nitrogen content (which corresponds to an increase in lattice parameter, Figure 3.12) [60,70,128,133].

Hardness has also been known to increase with nitrogen content and in some studies it was shown to peak and then stabilize at some slightly lower value [58,59,70]. The work of Dahm and Dearnley [48] reported a maximum hardness of 20 GPa when the nitrogen concentration is between 23 and 29 at%. Once this limit was exceeded, there was a departure from the linear relationship between nitrogen concentration in the coating and the nitrogen partial pressure in the gas mixture and subsequently, XRD peaks for nitrogen-rich phases were observed. The authors propose the explanation that the interstitial-substitutional clusters that are formed by nitrogen atoms clustering around chromium atoms, impede dislocation movement within the lattice and were therefore responsible for the increase in hardness.

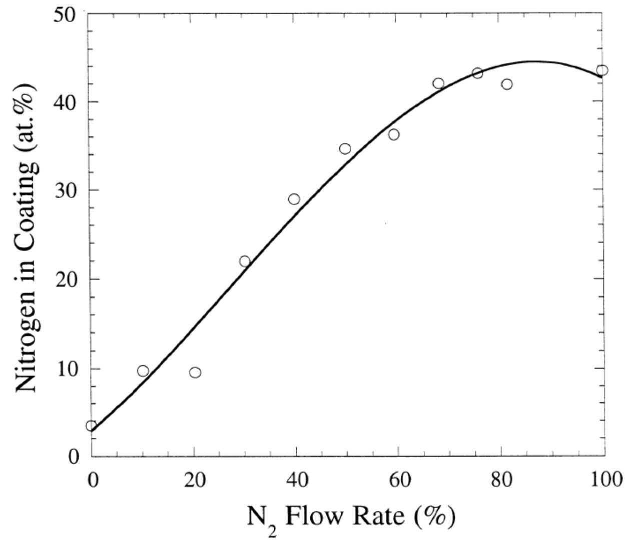

Figure 3. 11 An example of nitrogen content in sputter-deposited AISI 316 coatings with nitrogen percentage in the gas mixture (N + Ar) during deposition, from reference [133].

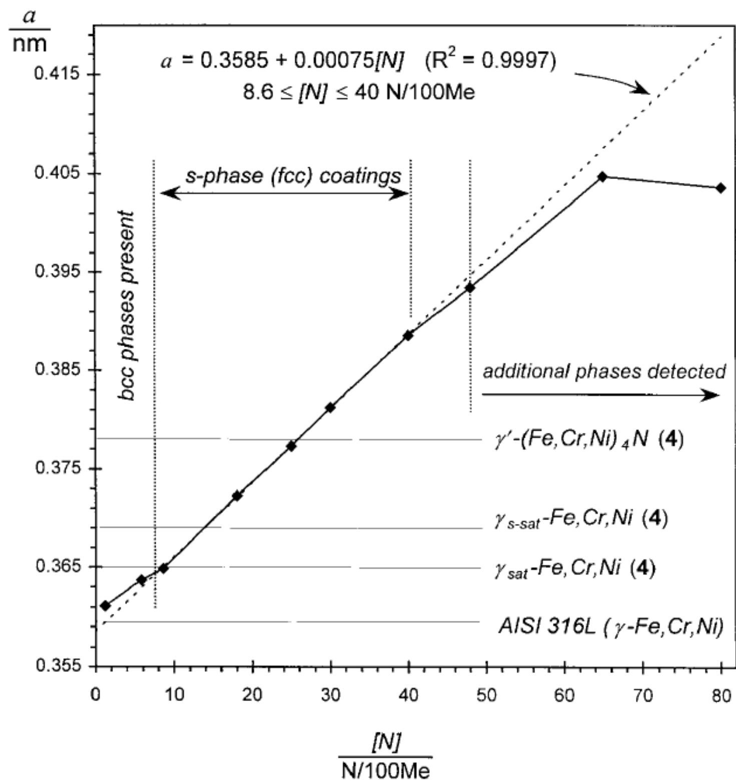

Figure 3. 12 Lattice parameter, a (nm) with nitrogen content (nitrogen atoms per 100 metal atoms), from reference [48]

Although as discussed above, some studies report nitride precipitation after exceeding a certain nitrogen content limit [48,53], only the work of Kappaganthu [128] had sputter-deposited coatings with nitrogen levels reaching 50 at% nitrogen in the film. In this work, the nitrogen percentage in the nitrogen-argon gas mixture during deposition was varied from zero to 75 % and although the nitrogen content in the film increased with nitrogen gas percentage in the gas mixture, it saturated at nitrogen gas percentages of 50 % or higher, forming a single phase of stoichiometric MN nitride (where M was a metal (e.g. Fe, Cr, Ni, Mo) that corresponds to the composition of the stainless steel target – AISI 316L, in this case). These results can be compared to those of Shedden [133], shown in Figure 3.11, that used an AISI 316 target and the same substrate material (silicon (100)) as Kappaganthu [128]. In this case the nitrogen content in the depositions increased linearly to reach and remain at around 40 at% for gas mixtures having nitrogen percentage (in an argon-nitrogen mixture) of 68 % or higher. Furthermore, the same work did not observe any iron nitride formation, even when the gas mixture was 100 % nitrogen. This disagrees with the earlier referred to studies that have observed nitride precipitation upon exceeding a certain amount of nitrogen quantity in the film.

Nitrogen percentage in the deposited coatings also increases with distance from the target [70,128] and according to the work of Alresheedi [53] seemed to be little affected by the substrate bias. Increasing the target power increaseed the flux arriving on the substrate, giving less time for nitrogen incorporation, resulting in lower quantities of nitrogen within the coating for the same gas mixture [128]. There is some disagreement when it comes to the effect of substrate temperature on the amount of nitrogen uptake: while Alresheedi [53] and Kappaganthu and Sun [128] show that nitrogen uptake is decreased with increasing substrate temperature, the work of Fryska et al. [47] does not show this trend, except when the N:Ar gas mixture was 1:1 and the authors explain that the

reduction in nitrogen occurs as a result of target poisoning. A similar target poisoning observation with consequent nitrogen uptake reduction was reported by Dahm and Dearnley [48] when the nitrogen partial pressure was equivalent to 50 % or higher of the total gas mixture.

Coatings of varying thicknesses (0.25 – 10 μm) have been deposited on various substrates: steels [47,48,58,60,70,122], silicon wafer [53,60,128] and soda glass [58] and a shiny metallic appearance that can become matte with high nitrogen content has been reported by some researchers [52]. It is generally accepted that there is a good correlation between the target composition and that of the deposit [59,92,133]. Despite this, some authors [48,52,60,133] report obtaining a b.c.c. ferrite deposit when no nitrogen is added to the gas mixture. However, upon adding small quantities of nitrogen to the gas mixture, the microstructure of the deposit changed back to austenitic [60,128]. Dahm and Dearnley [48] suggest the theory that f.c.c. austenitic targets have a metastable f.c.c. structure because atoms at temperatures below 340 °C do not have enough mobility to form the more stable b.c.c. and thus retain the f.c.c. structure. When these targets are sputtered, the resulting coating is b.c.c. ferrite unless it is conducted at a temperature of 500 °C or has large amounts of austenite stabilizing elements (such as nickel and nitrogen). However, the former option is not really viable, as it has been shown, similar to nitriding, that with temperatures exceeding 400 °C, chromium nitrides form in the expanded austenite coating [53,128].

In the majority of the studies, a preferential orientation has been observed: whereas in austenite, the (111) peak has the strongest intensity, many studies reveal XRD patterns where the (200) peak is stronger [47,48,52,53,58–60,70]. Some authors have observed that this texture came about with increased nitrogen concentration or substrate

temperature. Other studies, such as that of Kappaganthu and Sun [128] who sputtered an AISI 316L target onto silicon wafer, have not observed this tendency.

Since different studies use different parameters, different coating structures have been reported. Table 3.3 provides some examples. In some of these studies, the substrate was heated – therefore increasing the T/T_m – to avoid an amorphous deposition which has been observed in some studies when sputtering was conducted at a low temperature (e.g. <100 °C) [60,128]. Indeed, the work of Kappaganthu [128] showed that when adatom mobility was low, an amorphous deposit resulted, but when the adatom mobility was increased – either by heating the substrate or by increasing the target power (and therefore increasing the kinetic energy of the arriving flux), the structure became crystalline. The study only considered these two parameters, however, from the discussion in this chapter, it is clear that other parameters can also affect the kinetic energies of the depositing atoms – and the combination of all the parameters will ultimately affect the adatom mobility and therefore the structure formed.

Adhesion problems are not generally discussed and it is therefore generally assumed to be adequate. Actually, when nitrogen doped AISI 316L coatings deposited on substrates of the same material were tested for wear resistance, no delamination was observed [48]. In general, wear resistance improved with increasing nitrogen content, while toughness decreased once a certain level of nitrogen is exceeded [48,153].

Ref.	Target	Substrate	Substrate temp. (°C)	N at%	Structure observed (with respect to Thornton's Zone Model)
[53]	AISI 304	silicon	150 - 600	0-46	Columnar, angular and highly faceted structure (=> Zone 2). At higher temperatures: nodular, powder-like.
[60]	AISI 304L	silicon & low carbon steel	RT*	0-26	Columnar, fibrous (=>Type T)
[58]	AISI 316	copper & soda glass	RT*	--	Single magnetron mode: T-type 2 magnetrons operating in closed field mode: Zone 2 type
[47]	AISI 304 (X2CrNi 18-9)	AISI 304	200 - 400	10-33	~13 at%N – densely packed, fine grains: T-type ~24 at%N – very fine columnar grains (=> Zone 2) ~34 at%N – coarse and porous: Zone 1

Table 3. 3 Structures observed for stainless steel coatings deposited in literature

*RT = room temperature. Substrates are not heated – temperature increased by an unspecified amount as a result of the process.

The study by Bourjot et al, [70] briefly discussed an observation of a compressive internal stress in the coatings which the authors suggested is due to the intrinsic process stress and isothermal expansion mismatch between the AISI 310 austenitic coatings and the plain carbon steel substrates used in this work. This conclusion was drawn following

analysis of the curvature of a steel strip that acts like a cantilever beam. The authors provided a value for the thermal expansion for the AISI 310 austenitic steel coatings with nitrogen content in between 10 and 36 at%: 15-17 $x10^{-6}$ $°C^{-1}$. In this study [70], the compressive stress, although not quantified, was not deemed excessive and was regarded as favourable. In other work [133], the intrinsic compressive stress, measured from using the crystallite group method, was found to increase with nitrogen flow rate until it reached a maximum of 3 GPa at around 30 at% nitrogen content.

As has been seen throughout this chapter, the sputtering system is a complex set of interlinked parameters. Obviously, these process parameters affect the coating properties and make replication of a set of coatings difficult once the sputtering equipment is changed, since no two different sputtering systems have identical characteristics. The studies carried out by Dahm and Dearnley [58] and Saker et al [59] – are examples of studies where the authors performed an investigation using different deposition equipment and obtained relatively different coatings. At the end of this discussion it should be clear that more work is required to understand how the sputtering parameters affect nitrogen-doped austenitic stainless steel coatings.

CHAPTER 4 – EXPERIMENTAL EQUIPMENT AND PROCEDURES

4.1 Materials used

The chosen austenitic alloy target material for this work was ATI's Staballoy AG17 grade, the composition of which can be seen in Table 4.1. The appeal of this material lies in its lack of nickel – which is good for economic reasons as well as for potential biomedical applications. As explained in Section 2.2.2, there are several studies that focus on the use of expanded austenite for load-bearing medical implant applications such as hip joint replacements [56,153,154]. However, typical medical grade austenitic stainless steels such as AISI 316LVM / ASTM F138 / UNS S31673 and ASTM F1586 / UNS S31675 / (Rex 734 / Ortron 90) contain some nickel, which is always an issue since this substance can be a cause for contact dermatitis in some people. The use of a nickel-free material is therefore an additional benefit.

Readily available AISI 304 of dimensions 50 x 25 x 2 mm were chosen as a substrate material because of the similar austenitic structure (and Cr-content) to the target material and to conform to previous literature, where AISI 304 and AISI 316 are by far the most commonly used substrate grades. Moreover, the nickel in AISI 304 (and its absence in Staballoy AG17), together with the high manganese content in the coating (compared to the low quantities found in the substrate), would provide clear indications of the coating/substrate interface location in subsequent coating analysis. Some trials on silica glass substrates have also been conducted.

		Fe	C	Si	Mn	Cr	Ni	N	Mo	Cu
ATI STABALLOY AG17™ [155]	wt %	bal.	0.03	0.3	20	17	-	0.5	0.05	-
AISI 304 / S30400 / 1.4301 [20]	wt %	bal.	0.07	1	2	17.5-19.5	8-10.5	0.1	-	-
AISI 316LVM /S31673 /ASTM F138 [156]	wt %	bal.	0.03	1.00	2	17-19	13-15	0.1	2.25-3	0.5
ASTM F1586 / S31675 [157,158]	wt %	bal.	0.08	0.75	2.4-4.25	19.5-22	9-11	0.25-0.5	2-3	0.25
In atomic %, the target and substrate chemical compositions, respectively:										
ATI STABALLOY AG17™	at %	bal.	0.13	0.58	20	17.6	0	1.9	0.03	-
AISI 304 / S30400 / 1.4301	at %	bal.	0.3	1.45	2	18.4-20.5	7.5-10	0.4	0	-

Table 4. 1 Chemical compositions of typical biomedical materials, as well as target and substrate materials.

4.2 Substrate preparation

AISI 304 samples were manually ground and polished to a surface roughness of 0.03 µm or better, using silicon carbide grinding paper of grit size 120, up to 2500, and diamond suspensions of sizes 6 and 1 µm. Additionally, samples were ultrasonically cleaned in acetone for 15 minutes and subsequently, in isopropanol for 10 minutes, prior to coating deposition.

For those tests that included glass slides as substrates, substrate preparation comprised of the ultrasonic cleaning part only.

4.3 Coating deposition

4.3.1 Deposition apparatus

The equipment used to deposit coatings is a Nordiko unbalanced magnetron sputtering machine. The original configuration of this rig consists of closed field system with two targets placed at an angle of 90° to each other. In this work, only one of the targets was employed; the other target was fitted with a magnetic shield to prevent any interference from the permanent magnets that could be found behind it. The magnetic shield consisted of two nonmagnetic stainless steel sheets separated by a gap of 1 cm. The rig was therefore used as an open field unbalanced magnetron sputtering system with the substrate holder at a distance of 210 mm, directly facing the target – as indicated in Figure 4.1.

In such a Type II magnetron configuration (Window and Savvides, [88]), the plasma is confined between the unbalanced outer pole magnetic fields, which however, extend towards the substrate holder as indicated in the schematic diagram, Figure 4.1. Practically, the setup and plasma are shown in Figure 4.2. As explained in Section 3.1.4, such a plasma flux provides a means of ion bombardment to the growing film, affecting its structure and properties.

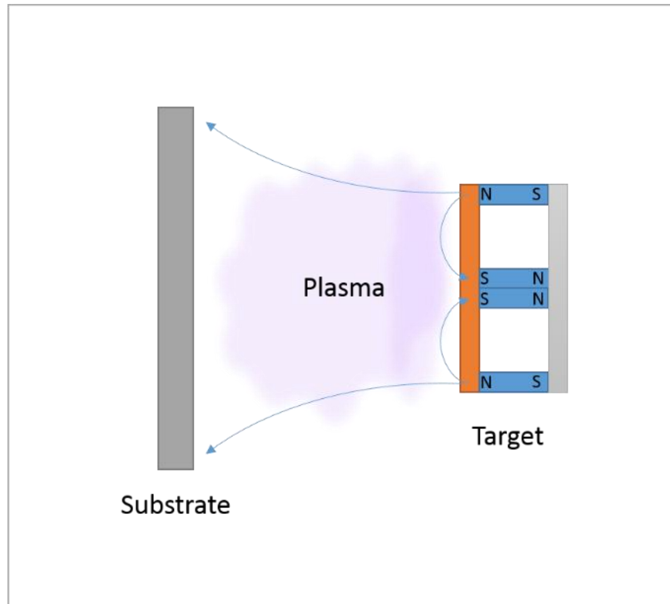

Figure 4. 1 Schematic diagram of the target and substrate holder configuration of the Nordiko unbalanced magnetron sputtering equipment

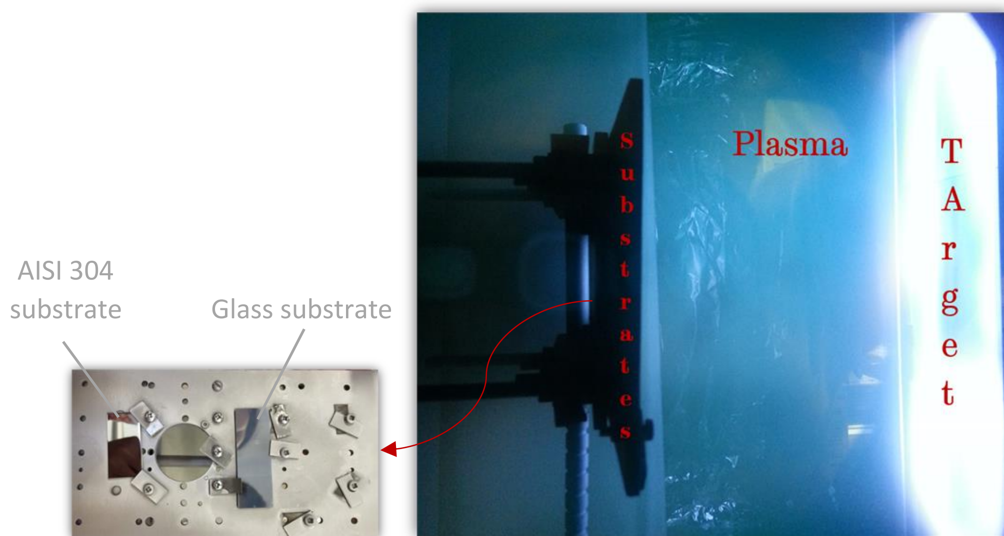

Figure 4. 2 (a) the substrate holder mounted with substrates, and (b) the target and substrate holder during a deposition run in the Nordiko unbalanced magnetron sputtering rig.

The rectangular target measures 380 x 100 x 6 mm and is fitted to a copper backing plate and cooling system to prevent target overheating. On the other hand, the substrate holder is stationary and has no temperature control option. The temperature of the substrates at the end of a run could be read off a K-type thermocouple that was inserted into a hole within a dummy substrate.

Both target and substrate holder were powered by ENI 10kW RPG-100E power supplies. The unit supplying the target was regulated in power mode whilst that supplying the substrate was set in voltage mode. The units provide a pulsing option that is regulated by two parameters – the frequency, 50-250 kHz, and pulse width of the reverse bias which the unit limits to a maximum of 40 % of the total cycle time. The reverse bias is fixed at a value between +30 and +40 V. The voltage and current, and current and wattage for the target and substrate, respectively, read off the LED monitors of the power supplies during the deposition runs were average values and not instantaneous ones.

High vacuum in the chamber was obtained via a rotary and diffusion pump system.

4.3.2 Equipment preparation

The chamber of the coating machine must be thoroughly cleaned to prevent contamination from chamber walls and other furniture as much as possible. All the removable parts, such as the shields, substrate holder and target cover were therefore sandblasted and air jet cleaned, while the rest of the chamber was covered in foil. Moreover, before the coating runs were conducted, a dummy run, whereby the chamber

was coated with the target material for 20 min was performed. This deposited a coating all over the chamber and its various components, reducing the risk of cross-contamination from the chamber materials.

4.3.3 Deposition procedure

A base pressure of $3x10^{-3}$ Pa was obtained by using the rotary pump to achieve 5 Pa, and then switching to the diffusion pump. Argon at a flow rate that gives an overall chamber pressure of 1 Pa was then let into the chamber and the sputter cleaning of the substrates at a pulsed (250 kHz, 88 % duty cycle) substrate bias of -500 V was conducted for 15 minutes. Subsequently, the target was sputter cleaned for 5 minutes at a chamber pressure of 0.27 Pa and a pulsed (123 kHz, 90 % duty cycle) target power of 1500 W. A mechanical shield in between the substrates and target prevented any particles that are sputtered off the target during cleaning to be deposited on the substrates.

The initial parameters used are listed in Table 4.2. These parameters, established partly based on literature but mostly on previous users' experience, were varied with the intention of providing an understanding of their effect on the coating and to subsequently establish a set of optimum parameters. Details of the specific coating deposition runs are given in each respective section in Chapter 5.

Parameter	Value
Chamber pressure	0.27 Pa
Target wattage	1200 W
Target pulsing: frequency and pulse width[1]	250 kHz, 496 ns
Substrate bias	-70 V
Substrate pulsing: frequency and pulse width[1]	123 kHz, 816 ns
nitrogen flow rate	Varied
Deposition time	2.5-5 hrs

Table 4. 2 Parameters used for sputter deposition process

No attempt was made to coordinate the pulse cycles of the target and substrate whenever these were both pulsed. When the cycle included nitrogen addition into the chamber, it was added at a rate of 1 sccm per minute subsequent to 5 minutes of deposition without any nitrogen. This was done to grade the film-substrate interface and minimize an abrupt change in properties from the film to the substrate. The substrates remained stationary throughout the deposition process.

4.4 Analytical techniques

All the deposited coatings were subjected to various analytical techniques for investigations of microstructure, composition and hardness. Some samples were also tested for corrosion resistance.

---

[1] Pulse width of the reverse time (i.e. of the 'pulse off' phase of a pulsed cycle – refer to Section 3.2.5).

4.4.1 X-Ray diffraction

X-ray diffraction analyses was carried out in a Siemens D5000 diffractometer. This equipment uses CuKα radiation (λ=0.15418 nm) and at normal working conditions the X-ray tube operates at 40 kV and 40 mA. Scans across the 2θ range of 30-120° were conducted at a step size of 0.02 and step time of 10 s.

In the specimen holder, test samples of a size generally larger than 10 x 20 mm sat on an Apiezon putty mound. By means of a glass slide, the sample was then gently pressed until its surface was level with the top of the sample holder. For this sample size, it is possible that some beam overspill could occur at lower angles, since the beam size increases as the angle is decreased. However, since the samples were sitting on a mound, any beam overspill would likely result in reduced intensities at low scattering angles, rather than any additional peaks.

For thinner coatings (<7 µm), where X-rays penetration of the substrate resulted in a pattern that had some interference from the substrate material, the glancing angle mode (GAXRD) was employed. The angles used were 6° and 8°, depending on the thickness of the coating. These angles were determined after a quick scoping exercise with one of the thinner coatings in which angles of 2, 4, 6 and 8 degrees were evaluated.

Finally, the obtained peak patterns were compared to those of known materials/compounds that can be found in the International Centre of Diffraction Data (ICDD).

4.4.2 Scanning electron microscopy (SEM) and energy-dispersive X-ray spectroscopy (EDX)

The thickness and chemical composition of the coatings was investigated by a Philips XL30 field emission gun scanning electron microscope (FEG-SEM) operated at an accelerating voltage of 20 kV. Both secondary electron (SE) and backscattered electron (BSE) imaging modes were used to identify certain features of the coatings. For these investigations, the samples were cut, mounted cross-sectionally in conductive Bakelite, ground and polished. Moreover, to protect the coating during grinding and polishing procedures, samples were mounted in pairs, with coatings facing each other, as indicated in the schematic diagram of Figure 4.3.

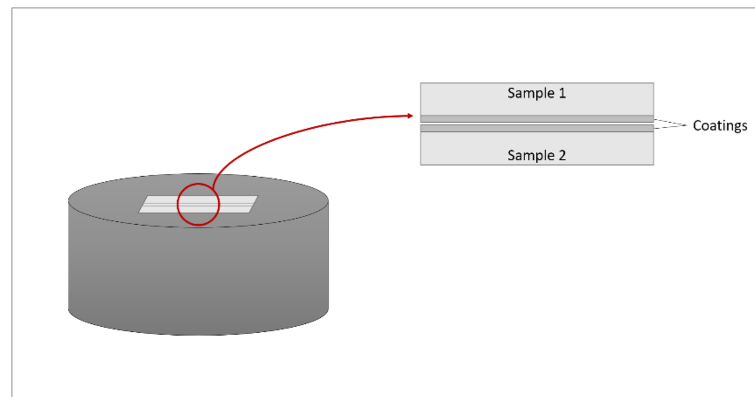

Figure 4. 3 Mounting of samples, with coating-to-coating interface

The same piece of equipment, the Philips XL30, is fitted with energy dispersive X-ray (EDX) detectors and Oxford Instruments INCA software, for quantitative elemental measurements. For these tests, calibration using a cobalt standard was conducted prior to every specimen measurement. By mounting the calibrating cobalt sample together with the sample under scrutiny, identical beam conditions for calibration and measurement

were ensured. The beam parameters used for EDX measurements were again an accelerating voltage of 20 kV, a spot size of 4 and a working distance of 5 mm.

4.4.3 Nano-indentation hardness measurements

The surface hardness of the coatings was measured by nano-indentation testing using a Hysitron Triboscope® nano-indenter, fitted with a Berkovich triangular diamond indenter. The load applied to measure the hardness was 10 mN, the maximum allowed by the instrument. The penetration depth at this load was less than 400 nm in all samples; and, since the thinnest coating had a thickness of 5.3 μm (most were ≈10 μm), the penetration depth was always well within 10 % of the coating thickness – conforming to the rule of thumb established by Bückle [159] for avoiding any substrate contributions to the hardness readings.

A minimum of 16 indents arranged in a 4x4 matrix, were performed on each sample. However this value was doubled or tripled when the hardness variation was high.

4.4.4 Fracture analysis

Fracture sections of the coatings were prepared by first cutting a thin slice (2 mm wide) from the test sample. This thin section was then incised from the back, until only about 1 mm of thickness remained for fracture, as indicated in Figure 4.4. The notched sample was then immersed into liquid nitrogen until the sample was entirely cooled, and

subsequently fractured by bending the sample in tension. This fracture operation was conducted manually, using pliers and the necessary protective equipment.

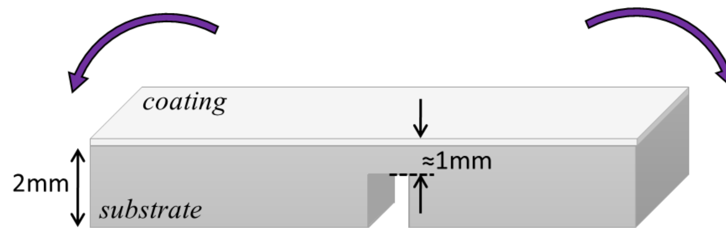

Figure 4. 4 Schematic diagram of sample preparation for fracture analysis, showing notch and direction of bending following immersion in liquid nitrogen

Fractured pieces were then adhered to an aluminium stub with double sided carbon tape, with the fracture facing upwards. Analysis of the fractured surface could then be conducted using the scanning electron microscope, Philips XL30, referred to in Section 4.4.2. For these analyses an accelerating voltage of 4 kV and a spot size of 3 were used.

4.4.5 Potentiodynamic corrosion tests

Finally, a few corrosion resistance tests were conducted. These tests served two aims: first, one aim of the project was to improve the mechanical properties of austenite with nitrogen doping without losing the good corrosion resistance exhibited by this phase; hence, assessing the corrosion resistance was very important. Secondly, testing for corrosion resistance was a good method to assess for chromium-nitride precipitation,

since if the latter was present, the corrosion resistance deteriorates due to the severe associated depletion of chromium incurred by the austenite [40].

The tests conducted involved a 1 hour open circuit potential (OCP) monitoring and a potentiodynamic scan, starting from 0.1 V before the OCP up to breakdown potential. A saturated calomel electrode (SCE) and a platinum electrode were used as reference and counter electrodes, respectively. The samples were tested in Ringer's Solution (9 gL^{-1} NaCl, 0.42 gL^{-1} KCl, 0.48 gL^{-1} $CaCl_2$, 0.2 gL^{-1} $NaHCO_3$) – a fluid of a salinity and pH equivalent to that found in the human body – at a temperature of 37 °C. The exposed area was 1.727 cm^2 and the scan rate was 0.17 mVs^{-1} – as suggested by ISO 17475:2008.

4.4.6 Statistical considerations

All the measurements presented in this work were given as the mean of repeated measurements together with one standard deviation to indicate the spread in the data. The sample size depended on the test being undertaken and on the variation within the measurements.

CHAPTER 5: RESULTS AND DISCUSSION

5.1 Introduction

In this chapter, the results shall be presented by first discussing the generic characteristics of nitrogen doped austenitic stainless steel coatings, then the effects of target power, target pulsing, substrate bias, substrate pulsing, substrate material and nitrogen quantity in these coatings. Finally, a discussion on stress, adhesion and precipitation will be presented.

5.2 Generic observations

5.2.1 Morphology and deposition temperature

Coatings produced in an argon only atmosphere exhibited a dense and featureless structure as shown in the polished cross sectional sample in Figure 5.1 (a). However, fracture analysis (Figure 5.1 (b)), revealed a dense, fibrous structure. Such a morphology falls under the classification of zone T in both the Thornton's and Anders' structure zone models. [96,131]. In addition most of the coatings, with the exception of a few cloudy samples, possessed a mirror-like surface finish – which is also a trait that pertains to a Zone T structure.

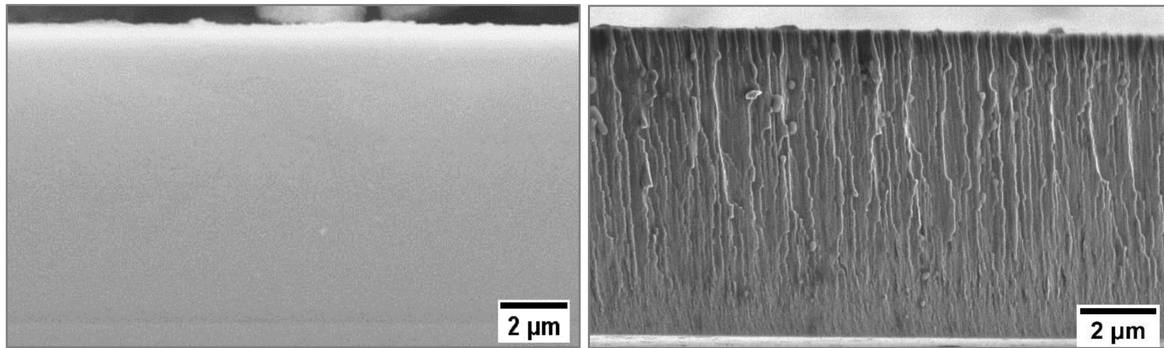

Figure 5. 1 (a) SEM polished cross section and (b) Fractured surface of coating deposited in an argon-only environment, at 1500W target power and -70V substrate bias

A closer examination of the fractured surface reveals another interesting observation; the fibres are initially extremely dense and become more defined, continuous and coarser after the first 2 µm of the coating. A similar denser layer close to the substrate has also been observed by other authors for deposited stainless steel coatings as well as other materials (AISI 316 deposits: [58], Be deposits [97], Cr films [117]), although an explanation has never been given. In this work, it is believed that this initial layer is a result of the temperature at the substrate during condensation that is initially relatively lower. Figure 5.2 gives the typical temperature profile of the substrate throughout the process. It can be seen that the substrate temperature, from an ambient 24 °C, initially decreases by a few degrees during pumping down, but then increases during the substrate etching (cleaning) process to 150 °C. During the subsequent target cleaning, since the substrate is protected by the shield in between the target and substrate preventing any sputtered atoms off the target to reach it, the temperature decreases by around 50 °C to about 100 °C. Upon the onset of the deposition process, the substrate temperature starts increasing once again, but saturates at around 200 °C. This means that the first layers of the film are deposited at a temperature of 100 °C, that gradually increases to 200 °C, at which temperature the rest of the coating is deposited. This difference in substrate

temperature results in the different coating morphology shown in Figure 5.1(b). It should be noted that the above referenced studies [58,97,117] all conducted sputter deposition on substrates that were initially at room temperature and therefore should have had similar conditions to this study. Furthermore, to the knowledge of the author – there are no studies that conducted sputter deposition on heated substrates and that have reported a similar sublayer.

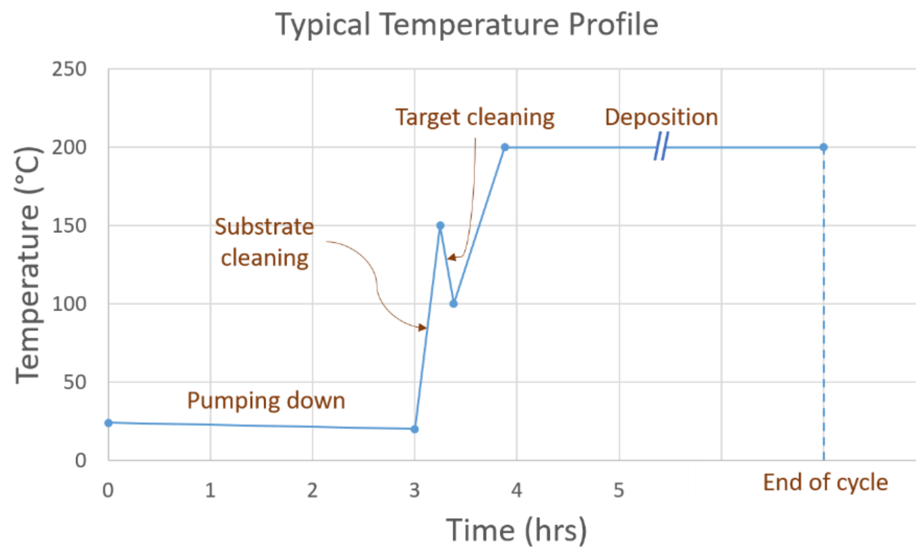

Figure 5. 2 Temperature profile in a typical sputter deposition run

5.2.2 Chemical composition

The elemental concentration of the coatings deposited in a pure argon atmosphere, presented in Table 5.1, deviated only slightly from that of the target material, with some loss of manganese and possibly nitrogen. These observed compositional deviations are similar to those observed by other authors [47,59,70,160]. It should be also be noted that

although at the vacuum levels employed in this work some impurity contamination was expected in the coatings, no oxygen was detected in the produced films. This suggests that the contamination quantities present were small and beyond the detection capabilities of the EDX equipment used.

The resulting phase of the coating in pure argon was ferritic, and although such a phase change to a b.c.c. structure from an austenitic target is widely reported in literature [48,52,60,133,161], the loss of manganese (and probably nitrogen) would tend to favour such a change, since both manganese and nitrogen are strong austenite stabilizers. With nitrogen addition into the chamber during deposition, the phase structure changed back to austenitic; this will be discussed in Section 5.8 (nitrogen doping).

	Fe	**Si**	**Mn**	**Cr**	**N**	**Ni**	**Other elements:**
Staballoy AG 17 theoretical	bal	0.58	20	17.6	1.9	-	C: 0.13, Mo: 0.03
Staballoy AG 17 as measured	bal	0.56 ±0.08	18.5 ±0.5	18.4 ±0.1	-	0.67 ±0.03	-
Deposited Staballoy AG 17	bal	0.46 ±0.05	17.5 ±0.1	19.1 ±0.1	-	0.76 ±0.01	-

Table 5. 1 Composition of target (at%): theoretical, measured and sputter-deposited coating.

A cross sectional EDX analysis of the coating deposited in an argon only atmosphere revealed that the coating is homogenous and therefore that the process is stable.

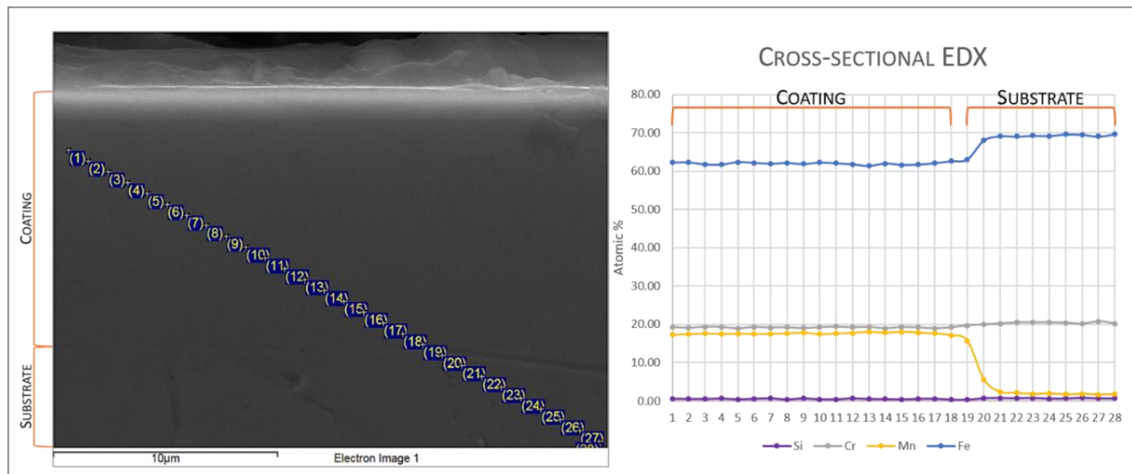

Figure 5. 3 EDX line scan across the cross-section of a coating deposited in an argon atmosphere at 1500 W (123 kHz, 90%), -70 V (250 kHz, 88%) substrate bias. Substrate, AISI 304 steel, and coating sections are indicated.

5.2.3 Adhesion

Typically, the coatings exhibited poor adhesion, which generally was not apparent upon unloading from the sputtering rig chamber, but which manifested itself upon further processing, such as cutting of the coated sample prior to analysis. The delamination incurred was to different degrees, varying from catastrophic delamination to coatings which had delamination only in some parts and which could only be seen through microscopic inspection. Further discussion on this subject will follow towards the end of the chapter (Section 5.9). At this point it should be pointed out that such delamination issues affected and limited the analytical tests that could be conducted on the coated samples produced. Whilst X-ray diffraction, EDX and nano-indentation could be conducted on most of the samples, except those few that failed catastrophically,

delamination has at times affected the quality of some of these results, particularly surface hardness measurements.

5.3 Target power

The target power was evaluated under two different conditions: in an argon-only chamber environment (0.27 Pa), were coatings were deposited at a target power of 1200 W and 1500 W, and in a nitrogen containing chamber environment, where the partial pressure contributed by the nitrogen was controlled by means of a flowmeter that was set to 4 sccm. The target powers evaluated in the latter case were 1000 W and 1200 W and the rest of the details for the runs are listed in Table 5.2.

Parameter \ Sample Name		argon- only (No nitrogen)		4 sccm nitrogen flowrate + argon (bal.)	
Base pressure	Pa	2×10^{-3}	2×10^{-3}	2×10^{-3}	2×10^{-3}
Target Power (123 kHz, 90%)	W	1200	1500	1200	1000
Substrate Bias (250 kHz, 88%)	V	-70	-70	-70	-70
Pressure	Pa	0.27	0.27	0.27	0.27
Duration	hrs	5	2	3	4
Nitrogen content	at%	0	0	16.7 ±0.8	16.9 ±0.4

Table 5. 2 Parameters for runs deposited at different target powers

The measured nitrogen content in the nitrogen containing samples was unaffected by a target power change of 20 %. This is despite the increase in deposition rate that a rise in

target power was observed to bring about – as shown in Figure 5.4, and as was previously reported by other authors [90,100,106–108].

The deposition rate is generally reported to increase linearly with power [90,100,106–108], however in this case, the curve is nonlinear. At this point it is not clear why the deposition rate has increased significantly at the power of 1500 W and further investigations would have to be conducted to provide a satisfactory explanation. However, some possible reasons could be suggested. When targets are operated at temperatures close to their melting temperatures, evaporative processes, in addition to sputtering, start taking place. This mode of operation, referred to as hot cathode sputtering, can lead to an increase in the deposition rate [162,163]. In this study, the target cooling system may have been insufficient during the higher target power used, unintentionally leading to the reported high deposition rate. It should also be noted that whilst many runs have been conducted at the other two powers (1000 W and 1200 W), only one run was conducted at 1500 W, meaning a one-off malfunction of the cooling system could have also led to this result.

Another reason that has been given in some studies for higher deposition rates is gas rarefaction [164,165]. It has been shown [166,167] that the gas in proximity of the target incurs a decrease in density due to collisional heating from the sputtered atoms. Presumably, the decrease in density leads to less scattering of the sputtered atoms, resulting in a higher deposition rate.

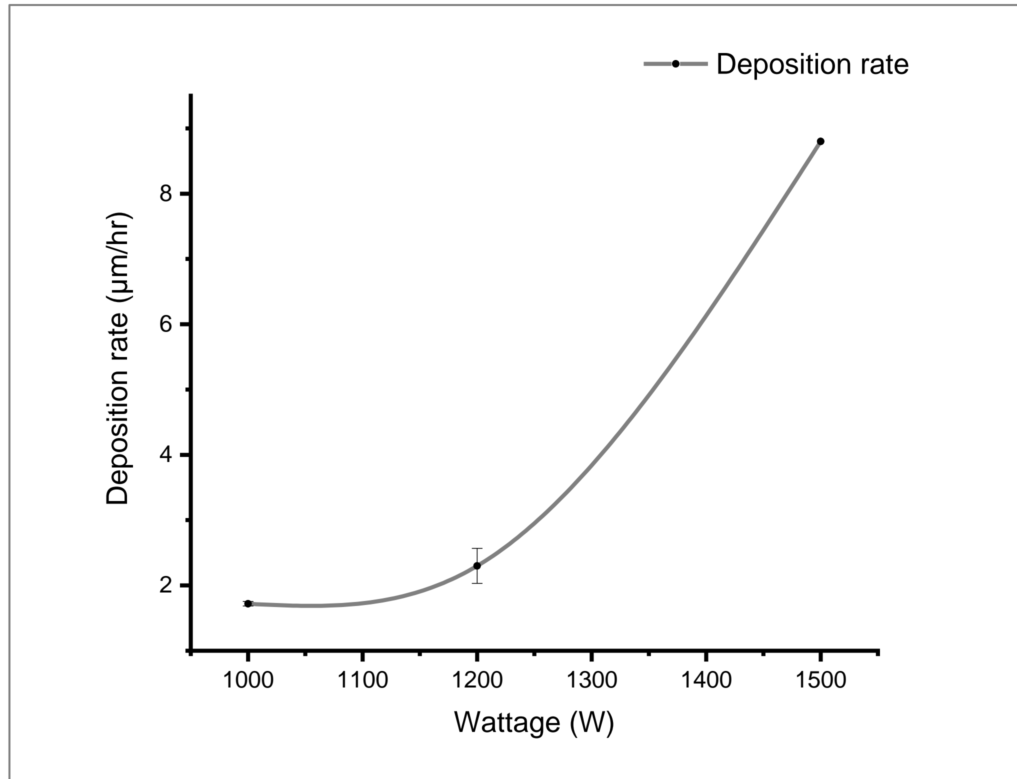

Figure 5. 4 Deposition rate vs. wattage, for runs conducted at a pulsed power (123 kHz, 90%), and -70 V (250 kHz, 88%) substrate bias

Figure 5.5 (a), shows the theta-2theta XRD pattern for coatings deposited in a pure argon atmosphere that were deposited at 1200 and 1500 W respectively, whereas Figure 5.5 (b) compares the GAXRD patterns for coatings deposited in a nitrogen atmosphere (at a flowrate of 4 sccm) deposited at 1000 and 1200 W. The former case (argon-only atmosphere) exhibits a predominantly ferrite structure for both patterns, whilst the latter (nitrogen-containing atmosphere) shows several austenite peaks. The discussion of what phases were obtained and how nitrogen gas, or lack of, in the chamber environment affects the phases obtained will take place in Section 5.8 (nitrogen doping). For the present discussion on target power, it should be noted that in each of the cases presented, the patterns obtained for different target power are similar. This means that a change in target power had minimal effect on the phases formed in the coatings.

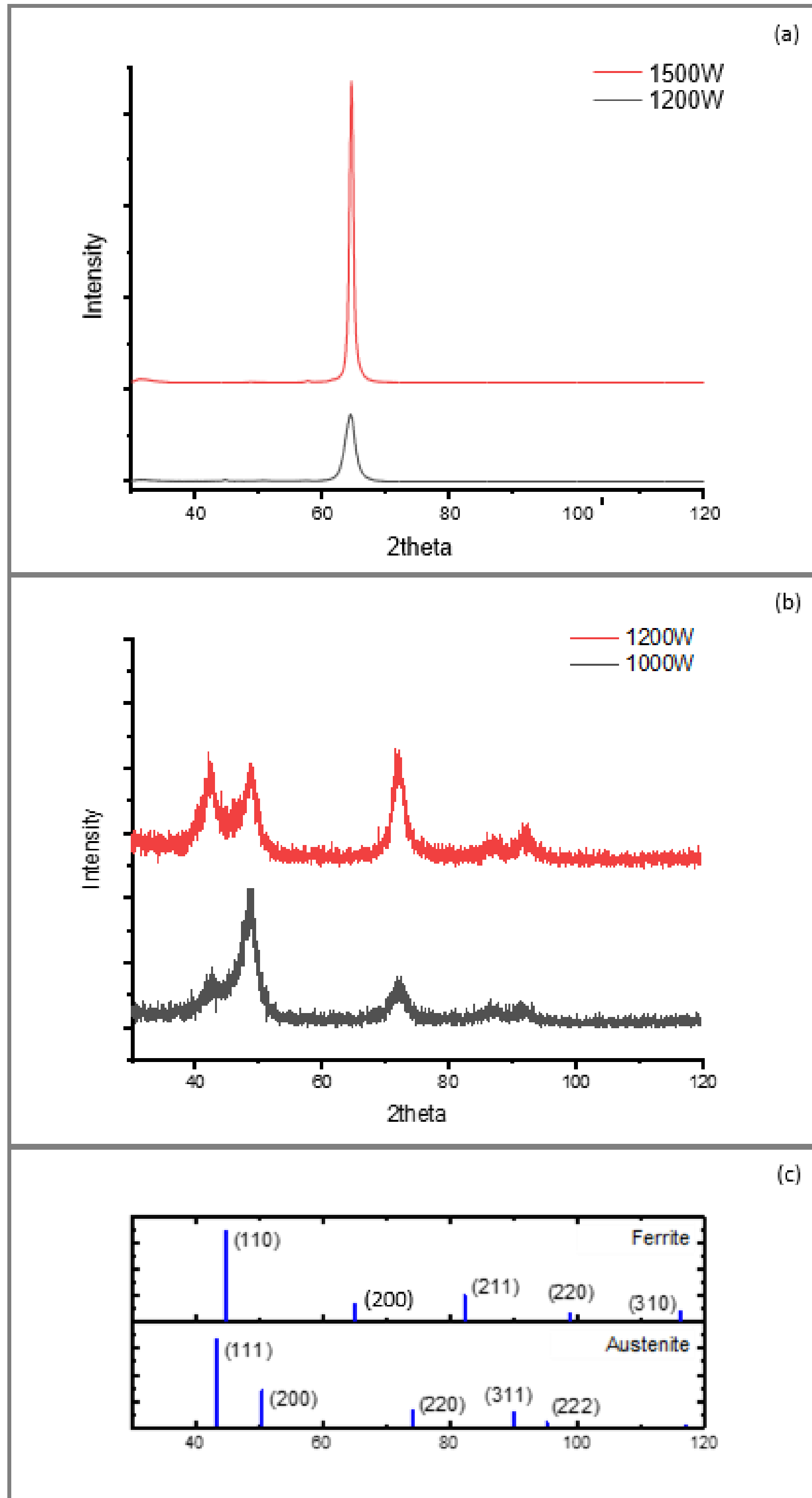

Figure 5. 5 (a) theta-2theta XRD patterns for coatings deposited at 1500W and 1200W in an argon only atmosphere; (b) GAXRD patterns for coatings deposited in a nitrogen containing atmosphere (4sccm) at 1200W and 1000W; (c) Peaks for ferrite and austenite, as per PDF cards 00-006-0696 and 04-018-3211, respectively.

The images in the Figures 5.6 (a) – (d), which show the structure of the coatings obtained when the deposition took place in an argon-only atmosphere at target powers of 1500 W, (a) and (b), and 1200 W (c) and (d), reveal how increasing the target power has affected the structure of the coating. While a dense fibrous structure was obtained at 1200 W, a coarser fibre structure, with some of the fibres extending through the thickness of the coating was obtained at a target power of 1500 W. This change in structure is a consequence of the higher energetic environment to which the growing coating is subjected to. As discussed in Section 3.2.4, increasing the power of the target increases the current, which in turn increases the plasma density, resulting in a greater quantity of argon ions available for target sputtering (increasing the deposition rate) as well as substrate bombardment (through the substrate bias). In addition, as the voltage is also increased, both the sputtered atoms, as well as the reflected neutrals which provide additional substrate bombardment, will have higher energies. In summary, increasing the target power provides a higher and more energetic flux impinging on the growing film.

This increase in momentum energy provided to the growing film at a higher target power could also be causing higher compressive stress in the coatings – resulting in higher hardness values, as suggested by the nano-indentation results tabulated in Table 5.3. Further research needs to be conducted to confirm this, as although for both of the cases presented (argon-only and nitrogen-containing deposition atmosphere), the average hardness increased with target power, a wide range of hardness values measured for one of the samples (the argon-only atmosphere sample deposited at 1200 W), prevents this statement to be statistically correct for the argon-only samples.

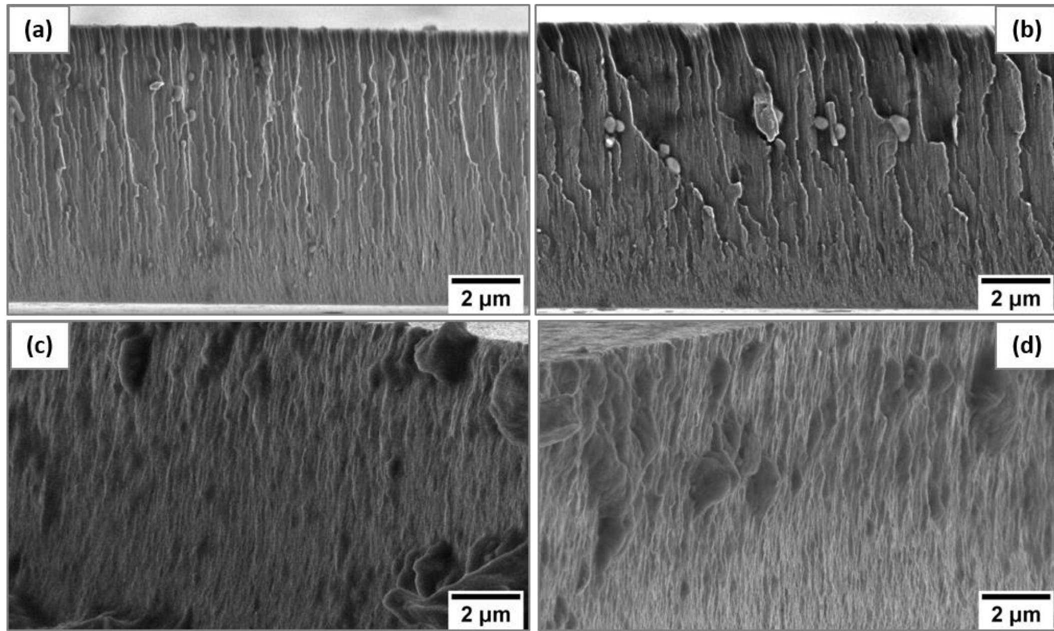

Figure 5. 6 Examples of fracture from coatings deposited in an argon atmosphere at 1500 W (a), (b) and 1200 W (c),(d)

Deposition atmosphere	nitrogen (at%)	Wattage (W)	Hardness (GPa)	Hardness Standard Deviation
Ar	0	1200	8.0	±1.2
Ar	0	1500	9.2	±0.5
Ar + N	17	1000	11.2	±0.5
Ar + N	17	1200	12.2	±0.6

Table 5. 3 Hardness measurements for samples deposited at different target power

5.4 Pulsed target parameters: frequency and duty cycle

The aim of this section was to try to understand the extent of the target pulsing parameters on the deposits. Hence, coatings were deposited under different duty cycle or frequency conditions, at two different nitrogen and target power levels. The working pressure of

0.27 Pa and a pulsed substrate bias of -70 V (250 kHz, 88 % duty cycle) were used for all the deposits.

The duty cycle at the target was varied by changing the pulse width of the reverse bias, and the different conditions tested are listed in Table 5.4. As shown by the thickness, nitrogen content in the deposits, hardness and texture presented in Table 5.4 and Figure 5.7, respectively, changing the duty cycle over the ranges tested did not yield any evident differences in the deposited coatings. The samples that were deposited at 1200 W, contained high nitrogen contents which consequently resulted in some nitride precipitation. As will be discussed in further detail in Section 5.8 (nitride precipitation), a large variation in hardness was measured with the onset of nitride formation. On the other hand, the hardness of the samples deposited at 1000 W could not be measured due to extensive coating delamination. While in previous studies [91,110], the focus was on establishing the maximum duty cycle possible for an arc free process, in these tests, no arcing was experienced for any of the conditions.

Power	**N flow rate**	**Time**	**Freq.**	**Pulse width**	**Duty cycle**	**Thickness**		**N content**		**Hardness**	
W	**sccm**	**hrs**	**kHz**	**ns**	**%**	**µm**	**±σ**	**at%**	**±σ**	**GPa**	**±σ**
1200	10	5	123	576	93	10.0	0.60	26.9	2.07	6.1	1.6
1200	10	5	123	816	90	10.0	0.48	28.0	1.02	5.5	1.3
1200	10	5	123	1213	85	10.0	0.12	31.8	1.33	6.7	1.9
1000	4	4	123	816	90	7.00	0.04	16.9	0.4	11.2	±0.5
1000	4	4	123	1616	80	6.61	0.04	19.8	0.6	n/a	n/a
1000	4	4	123	2416	70	6.59	0.05	18	0.6	n/a	n/a

Table 5. 4 Parameters, thickness, nitrogen at% and hardness for samples deposited at different target pulse width and duty cycle

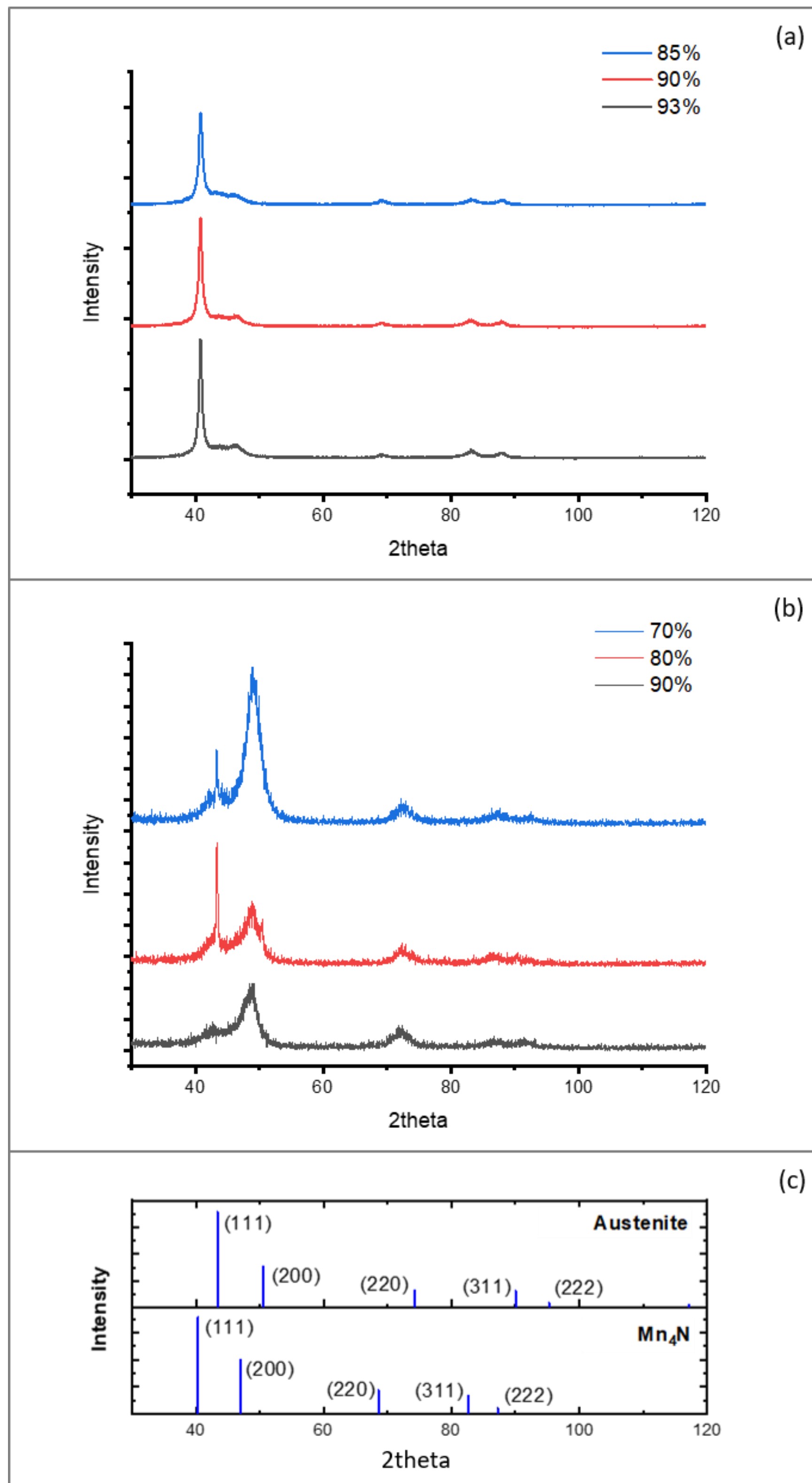

Figure 5. 7 (a) Theta-2theta XRD patterns for coatings deposited at different duty cycles at 1200 W, 123 kHz and nitrogen flow rate of 10 sccm and (b) GAXRD patterns for coatings deposited at different duty cycles at a target power of 1000 W, 123 kHz and 4 sccm nitrogen flow rate.

As explained in section 4.3.1, the pulse of the power supplies can be controlled from the frequency and the pulse width of the reverse time. However, the power supply's configuration is such that while the frequency can be set to any value from the range 50 to 250 kHz, the pulse width can only be set to a value from a pre-programmed set of values (e.g. 816, 896, 976… etc (ns)). This made it difficult to maintain the duty cycle at the same exact value (e.g. 80 %), whilst increasing the frequency. However, since the runs were set with parameters where the difference in frequency in much larger than that in the duty cycle, (as can be seen in Table 5.5), any affects generated from the frequency should still be detectable.

Power	**N flow rate**	**Time**	**Freq.**	**Pulse width**	**Duty cycle**	**Thickness**		**N content**		**Hardness**	
W	**sccm**	**hrs**	**kHz**	**ns**	**%**	**µm**	**±σ**	**at%**	**±σ**	**GPa**	**±σ**
1200	10	5	123	1216	85	10.0	0.12	31.8	1.33	6.7	1.9
1200	10	5	164	1216	80	10.6	0.15	34.0	1.02	4.7	1.4
1000	4	4	123	816	90	7.00	0.04	16.9	0.4	11.2	±0.5
1000	4	4	245	816	80	7.00	0.03	22.4	0.4	13.5	±1.5

Table 5. 5 Parameters, thickness, nitrogen content and hardness for samples deposited at different target frequencies

Previous work on the pulse frequency variation of the applied target power [92,111] has shown how pulsing the target results in more energetic ion fluxes impinging on the substrate surface. This would often result in an improvement of certain coating qualities such as adhesion and wear resistance [111–113]. However, there have been reports [91,110] where increasing the frequency did not result in any significant changes in the coatings. In this work, as the frequency increased, the only deduction that can be inferred

from the results tabulated in Table 5.5 is that the nitrogen uptake seemed to increase with increasing frequency. The XRD results also show this increase in nitrogen for the 1000 W samples (Figure 5.8 (b)), with a slight shift of the peaks to lower angles and, as shall be seen in the section discussing nitrogen doping (Section 5.8) – as the nitrogen increases, the peaks become increasingly (200) oriented. For those samples deposited at 1200 W and a higher nitrogen flow rate, EDX measurement and XRD testing were not enough to determine whether the increase (≈33 %) in target power frequency resulted in an increase in the nitrogen content of the coatings – this is because on the one hand, the relatively larger measurement error for the nitrogen content measured by EDX puts the difference between the runs within statistical error, and secondly, the onset of nitride precipitation[2] resulted in XRD peaks with positions similar to those of austenite, making interpretation of the XRD patterns more difficult. Furthermore, it should be noted that the difference in frequency in the tests conducted at 1200 W was not as large as that in between the samples deposited at 1000 W, where the frequency was doubled.

The measured coating thicknesses clearly show that increasing the frequency did not result in any increased re-sputtering effects on the coating, suggesting that the high energy ions impinging on the substrate (resulting from pulsing the target) do not have sufficient energy to etch the depositing coating. On the contrary, more nitrogen atoms have become trapped into the coating. It is not clear what mechanism could cause such an increased nitrogen entrapment, but it could be speculated that the higher energy in the flux caused better 'packing', and perhaps 'forcing of' the nitrogen atoms into interstitial sites, without being excessive enough to cause re-sputtering.

---

[2] Nitride precipitation, its type and interpretation of the XRD pattern will be discussed in some detail in Section 5.8

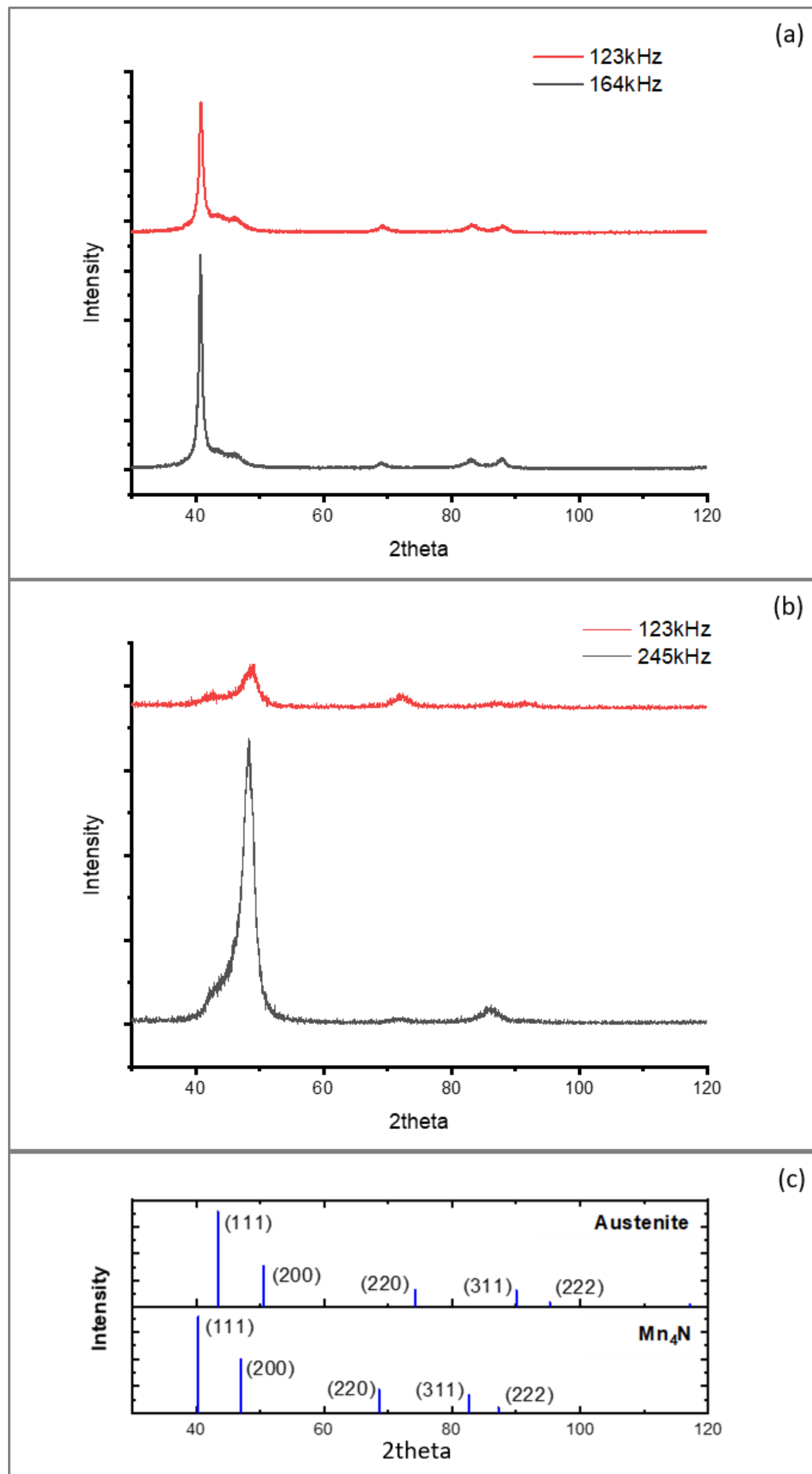

Figure 5. 8 (a) Theta-2theta XRD patterns for coatings deposited at different frequencies at 1200 W, 10 sccm nitrogen; (b) GAXRD patterns of coatings deposited at different frequencies at 1000 W and 4 sccm nitrogen; (c) Peak positions for austenite and Mn_4N *as per PDF cards 04-018-3211 and 01-089-3704, respectively*

5.5 Substrate bias

In order to assess the effect of the substrate bias on the deposits, 3 hour runs using a pulsed target power of 1200 W (123 kHz, 90 % duty cycle) and a nitrogen gas flow rate of 4 sccm were deposited with pulsed substrate biases of -40, -70 and -110 V (250 kHz, 88 % duty cycle). As can be seen from Figure 5.9, the substrate bias had little effect on the hardness, but the thickness and nitrogen uptake decrease as the negative bias increases. The ion current drawn at the substrate increased with substrate bias, as observed by other authors [124,125].

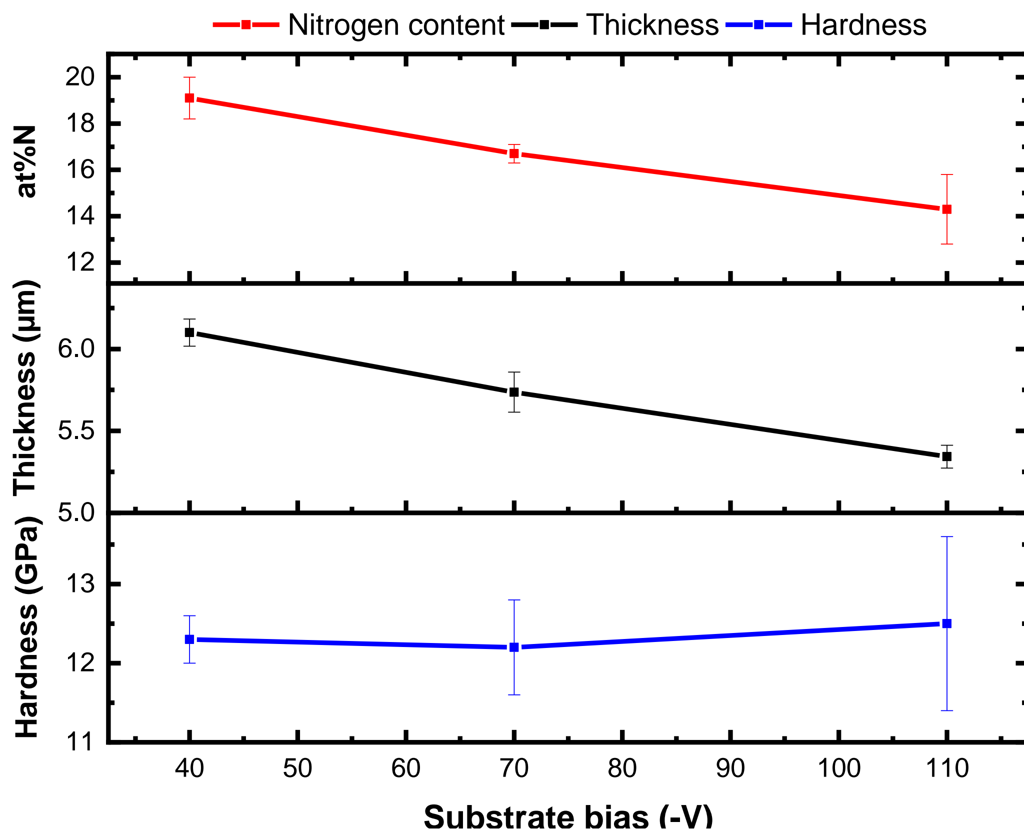

Figure 5. 9 Nitrogen content, thickness and hardness against substrate bias (pulsed at 250 kHz, 88 % duty cycle) for coatings deposited at 1200 W (123 kHz, 90 % duty cycle) and flow rate of 4 sccm nitrogen

A nitrogen reduction in films upon the application of some substrate bias (-100 V) was already been observed by Winters and Kay [168] for nickel films, although in that case the quantities of nitrogen involved were of an order of magnitude smaller and the change observed in the nitrogen values was much higher. In this case, the nitrogen content decreases from 19 at% for the -40 V sample to 14 at% in the -110 V case. Given that the changes in nitrogen content are small, it is not surprising that the XRD patterns, shown in Figure 5.10, did not entirely reflect the variation in the nitrogen uptake; where the patterns for the -70 and -110 V were very similar, whereas that for the -40 V substrate bias showed a different preferred orientation.

In literature, while some authors have found that a substrate bias changed the preferential orientation in their films (Ta: [119]; Al: [116]; Be: [97]; CrN: [123]; TiN: [169] TiN-MoSx [125], others did not observe any major differences (Cr: [117]). This is because any changes occur as a result of the changes in the energy supplied to the growing surface – and whether or not a substrate bias provides enough energy to incur changes in the texture of phases obtained, depends on the particular system being employed.

In this case, at a substrate bias of -40 V, the deposit has a relatively high amount of nitrogen (19 at%), and with respect to the other coatings, should be the least stressed, since substrate bias is widely reported to increase compressive stress CrN: [123]; TiN-MoSx [125]; Al: [116]; Cr: [117]; ZrO_2 –Y_2O_3 [118]; Ta:[119]; Nb [99]; various materials [120]). The XRD pattern shows a main peak at 24° - which is not an austenitic peak, but which does not seem to be any of the main nitride peaks either.

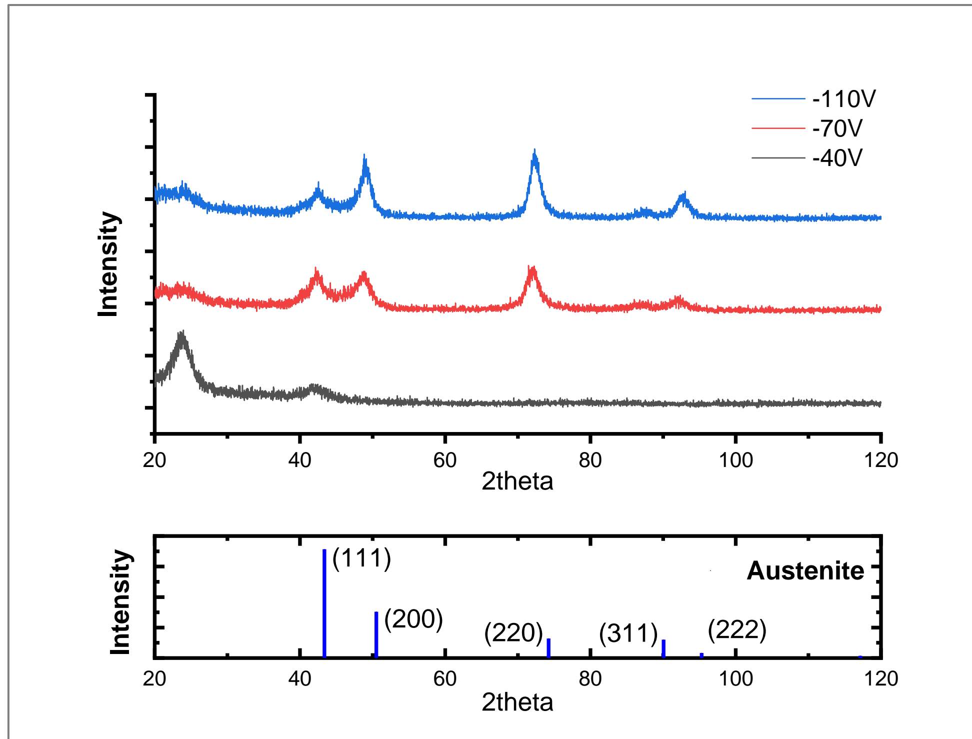

Figure 5. 10 GAXRD patterns for coatings deposited at a pulsed target power of 1200 W (123 kHz, 90 % duty cycle), nitrogen flow rate of 4sccm, and different pulsed (250 kHz, 88 % duty cycle) substrate bias values -40, -70 and -100 V. Superimposed are the austenite peaks from PDF card 04-018-3211

The decrease in thickness with substrate bias could be explained by an increased re-sputtering effect of the deposit that is caused by the argon ions in the environment, that bombard the substrate at higher energies as the substrate bias increased. A decrease in thickness was also observed by Freeman et al. [123] and Gangopadhyay et al. [125] in the deposition of chromium nitride films and composite TiN-MoS_x films, respectively. Re-sputtering could in fact also explain the reduction in nitrogen observed with bias increase discussed earlier – with the suggestion that a preferential re-sputtering of nitrogen is taking place.

Qualitative SEM assessment of the coatings deposited at different substrate bias values did not reveal any improvement or deterioration in the adhesive properties of the coatings. In all cases, doming – as shown in Figure 5.11 was observed. Moreover, whilst the hardness variation in the sample biased to -110 V indicated extensive delamination, one sample deposited at a substrate bias of -40V failed catastrophically during cutting. Other samples have shown some wrinkling upon cutting.

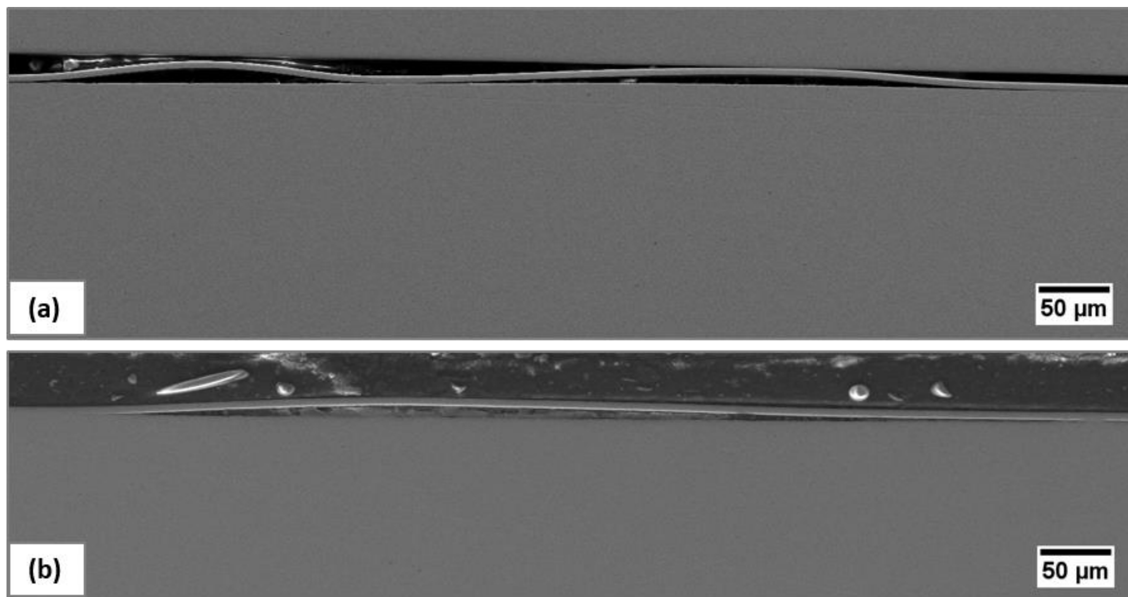

Figure 5. 11 SEM cross-sectional images of coatings deposited at pulsed target power of 1200 W (123 kHz, 90 % duty cycle), nitrogen flow rate of 4sccm, and pulsed (250 kHz, 88 % duty cycle) substrate bias values of -110 V (a) and -40 V (b).

As previously stated, the literature stipulates that increasing the substrate bias tends to increase the compressive stress in a coating. Moreover, it is often suggested that hardness exhibits a similar trend to the compressive stress [125,170]. Hence, a higher hardness

was expected as the substrate bias was increased. However, despite the significant variation, the hardness measurements in these experiments have shown no major shift as the substrate bias increases. This could be explained by the simultaneous decrease in nitrogen with substrate bias (as shown in Figure 5.9), which is known to have a major effect on hardness [48,59,70]. This suggestion that two opposing mechanisms: the increase in stress and the nitrogen reduction with increasing substrate bias, maintain the hardness at a relatively constant level would partially disagree with the findings of Darbeida et al. [122], who stated that, for similar nitrogen doping levels in AISI 316L coatings, no changes in hardness were observed when the substrate bias was varied. The authors therefore suggest that the nitrogen effect on the hardness is higher than the atomic peening caused by the substrate bias. While this study suggests the action of two opposing mechanisms, it does not contradict the statement made by Darbeida [122], as while the change in nitrogen quantities is only 5 at% (representing a 25 % decrease in nitrogen content), that of the substrate bias is a relatively larger 70 V (which is equivalent to an increase of 175 % in substrate bias).

5.6 Substrate pulsing

To understand how pulsing the substrate bias was affecting the deposits, coatings produced with a -70 V bias voltage, in pulsed and DC mode, were compared for two different nitrogen flow rates: 5 and 10 sccm. The rest of the parameters were kept constant. The target was given a power of 1200 W and pulsed to a frequency of 123 kHz (90 % duty cycle) while the substrate pulse frequency was set to 250 kHz (88 % duty cycle). The duration of the runs was 2.5 hrs, at a working pressure of 0.27 Pa.

During the process, the ion current drawn at the substrate for the pulsed samples (in both 5 and 10 sccm runs) was measured to be 0.9-1.0 A, translating to an approximate ion flux density of 0.24 mA/cm^2, almost twice that measured for the DC counterparts which stood at 0.05-0.06 A and 0.13 mA/cm^2, respectively. This agrees with what was observed by other authors in other material systems [125,169].

nitrogen flowrate (sccm)	**Substrate pulse mode**	**N at% (± 1.2)**	**Thickness µm (±0.1)**	**Hardness GPa**
5	Pulsed	18.2	5.6	11.8 ±0.5
5	DC	20.9	5.5	12.6 ±0.3
10	Pulsed	28.2	5.6	6.9 ±1.8
10	DC	30.6	5.5	11.8 ±2.6

Table 5. 6 Nitrogen content, thickness and hardness for coatings deposited in the pulsed and DC substrate bias modes, at different nitrogen flow rates

EDX results show that when the substrate was pulsed the nitrogen content was slightly less than when the bias is in DC. This shows that a higher re-sputtering rate of nitrogen took place when the bias was pulsed. Given that the measured ion current drawn at the substrate is higher for pulsed samples, it follows that the higher re-sputtering of nitrogen is a consequence of the higher ion flux impinging on the substrate. As evidenced by the thickness that remains constant, re-sputtering is limited only to nitrogen, unlike what was reported by Gangopadhyay et al. [125] in a TiN-MoS_x composite coating system, whereby the coating thickness decreased with pulsing due to re-sputtering of the coating.

The small difference in nitrogen content, seems to be reflected in the hardness measurements for the 5 sccm samples, where the DC sample has a higher hardness when compared to its pulsed counterpart. Although previous studies [114,123,125,127] have reported that the hardness and compressive stress both increase with pulsing, in this case

it would seem that the nitrogen content has a greater effect on the hardness than that of a pulsed bombarding flux. Unfortunately, it is not possible to also consider the hardness of the 10 sccm samples, since the spread in the readings was too wide. This large variation is due to bad adhesion resulting from stress, as will be discussed in Section 5.9.

XRD results in Figure 5.12 show that pulsing the substrate did not affect the resulting phases in the coating, as the patterns between pulsed and DC samples are very similar. The 5 sccm samples exhibit an austenitic structure; and the peaks for the DC sample are at slightly lower angles than those of the pulsed sample, due to the higher nitrogen content. On the other hand, the 10 sccm samples appear to have precipitated Mn_4N nitrides.

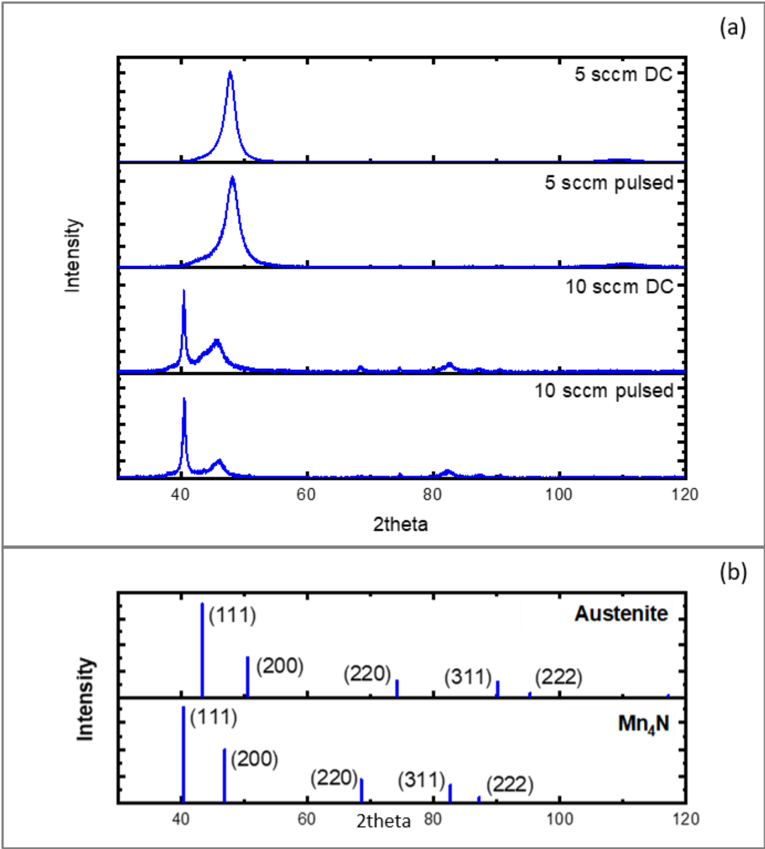

Figure 5. 12 Theta-2theta XRD patterns for coatings deposited in pulsed (250 kHz, 88 % duty cycle) and DC mode, at different nitrogen flow rates (5 or 10 sccm) and power 1200 W (123 kHz, 90 % duty cycle).

5.7 Substrate material

In a coating deposition run without nitrogen and 1500 W target power, glass slides and AISI 304 metal pieces were used as substrates. Both the target and substrate bias were pulsed. The glass slides, same as the metal pieces, were successfully coated, with a highly reflective coating. No delamination was observed for glass, not even during post-deposition processing.

Figure 5.13 (a) shows the XRD patterns obtained for both glass and steel substrates. Since no nitrogen was introduced into the chamber, the resulting microstructures are ferritic with a dominant (200) orientation. The pattern for steel appears to have a stronger texture compared to the coating deposited on the glass slides. On the other hand, the latter, shows a small peak at ≈45°, which could represent the (110) ferritic peak and another small broad peak around ≈51°, which could suggest the presence of some austenite. To better show these smaller peaks, the same patterns in Figure 5.13 (a) have been plotted on a logarithmic scale in Figure 5.13 (b). This latter representation has revealed other small ferritic peaks at ≈82°, ≈99° and ≈116°. The stronger texture for the steel substrate can be attributed to the higher bias effect on the steel with respect to the glass, as it has been reported in a number of studies that increasing the bias, resulted in a different texture [97,107,114,116,119,123,125,127,169].

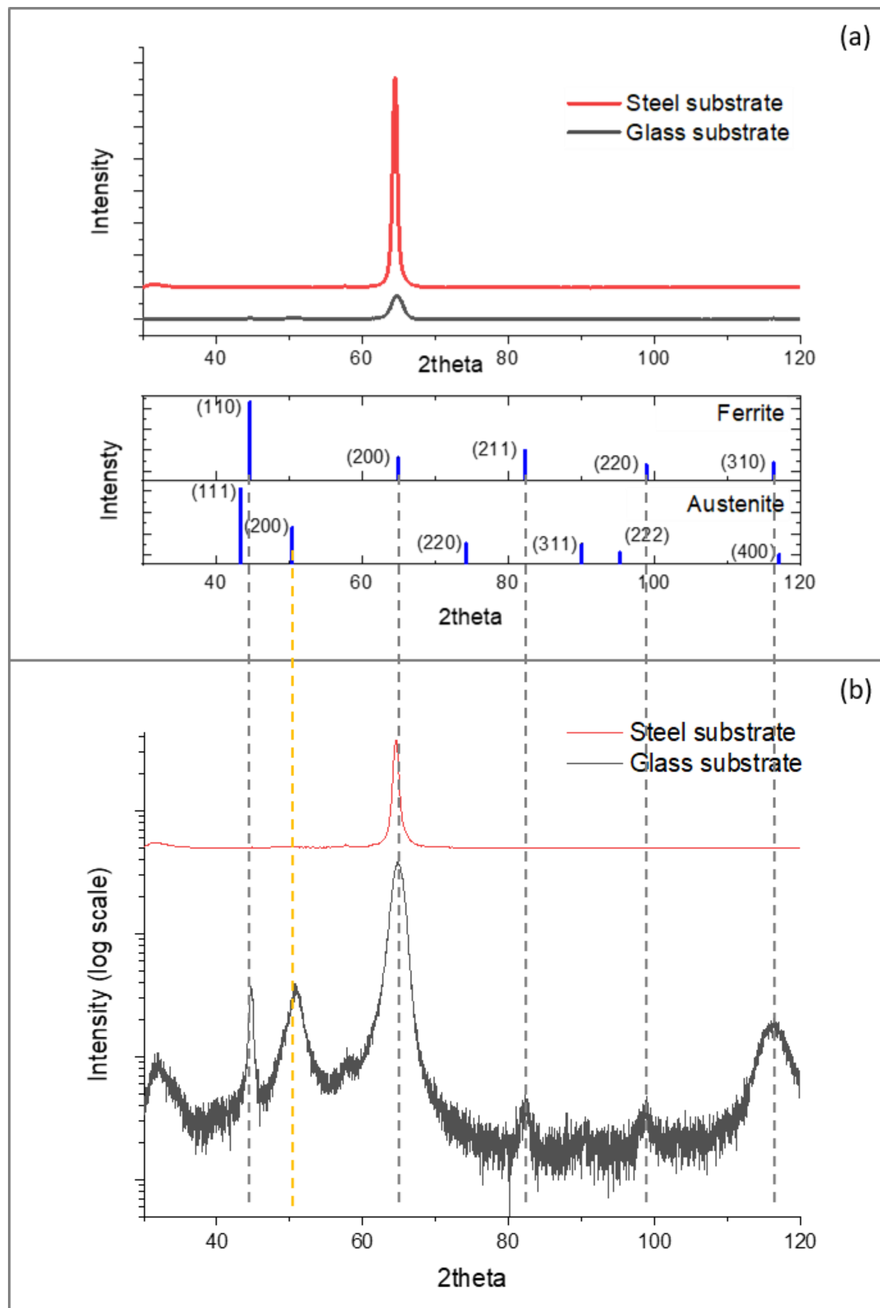

Figure 5. 13 (a) Theta-2theta XRD patterns for coatings deposited onto different substrates: steel and glass. Also displayed are the peak positions and relative intensities for ferrite and austenite as per PDF cards 00-006-0696 and 04-018-3211 respectively. (b) shows same patterns in (a) but in logarithmic scale.

SEM/EDX analysis of the samples revealed small differences in thickness and composition, as shown in Table 5.7. These differences could be partly due to a different position within the chamber, but could also be the result of different condensation

conditions provided by the glass. The noticeably higher manganese content would justify the XRD pattern for glass exhibiting some austenite. However, it is difficult to justify the difference in thickness, except by variation in the flux of the plasma within the chamber.

	Si at%	**Cr at%**	**Mn at%**	**Fe at%**	**Ni at%**	**Thickness µm**	**Hardness GPa**
Steel	0.5 ±0.1	19.0 ±0.1	16.8 ±0.2	62.9 ±0.2	0.8 ±0.1	9.0 ±0.1	9.2 ±0.5
Glass	1.2 ±0.4	18.1 ±0.1	19.5 ±0.1	60.5 ±0.2	0.7 ±0.1	8.7 ±0.1	8.8 ±1.9

Table 5. 7 Elemental composition, thickness and hardness of coatings deposited onto different substrates: steel and glass

The major difference between the coatings lies in their structure, as shown in Figure 5.14. Clearly, the coating deposited on glass does not have the same fibrous Zone T structure as that deposited on steel. It rather has coarser grains, with possibly some voids in between. This change would be the result of the heat dissipation properties of the substrate used and the substrate bias effect on the condensing surface. Heat dissipation is not as good in glass as it is in steel, which increases the T/T_m for the coating deposited onto the glass substrate, which in turn increases the energy given to the condensing atoms and should lead to a columnar structure. On the other hand, the substrate bias acting on the glass substrate may not be as effective as that on the steel and as shown by previous studies (TiO_2: [169]; CrN: [123]; TiN: [114,125,127]), the bombarding action of the substrate bias also supplies energy to the condensing surface that leads to an increased substrate temperature and densified structure. For the deposit on the glass substrate, therefore, while a poor heat dissipation could be increasing the T/T_m, a lower effective bias could be decreasing it.

In a study by Alresheedi and Krzanowski [53] were AISI 304 was deposited on Si substrates, deposits conducted at a bias of -100 V produced a microstructure that is very similar to that deposited on glass in this study. When the substrate bias was increased to -140 V, a more columnar structure was observed and although the microstructure becomes coarser with temperature as well, the columnar structure was observed only with the increase of nitrogen content or substrate bias, but not with temperature alone. Comparing these observations to those in this study, it can be concluded that the effects in the different morphology are the result of a more dominant reduced bias effect (compared to the decreased heat dissipation effect) when the substrate is glass, which resulted in a Zone 1 structure. The increased variation in nano-hardness measurements for the deposit on the glass substrate could also be explained by this structure, which as shown in Figure 5.14 (b), contained some voids.

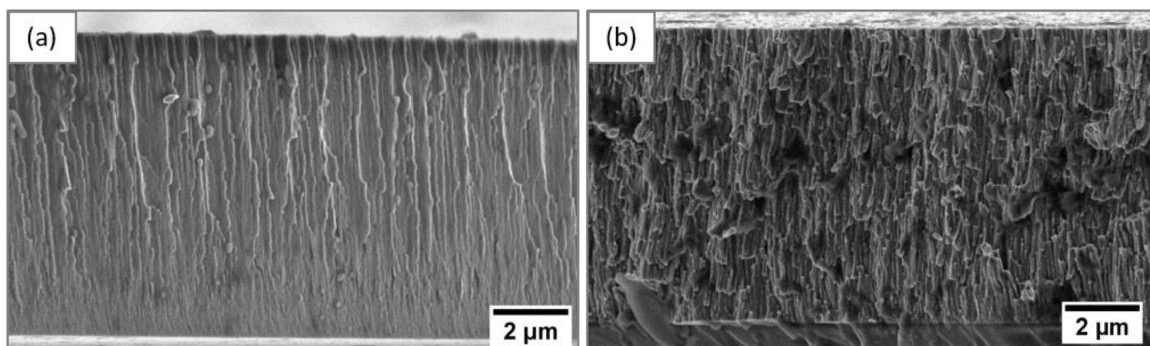

Figure 5. 14 Fracture of coating deposited on steel (a) and glass (b) in an argon atmosphere, 1500 W target power and -70 V substrate bias

It can therefore be concluded that although coating on glass was possible, the resulting coating structure (and consequently some of the coating properties) were different. The differences in the coatings are a result of substrate heat dissipation and substrate bias effects, which were affected by the substrate properties. These findings differ from those

of Alresheedi and Krzanowski [53], that reported a similar structure for steel and silicon substrates in the deposition of nitrogen-doped AISI 304 films. Most of the other studies that perform depositions on different substrate materials (to facilitate subsequent different analytical tests on the resulting coatings) do not comment about any differences in coating structure between the samples (e.g. [58,60,112]).

5.8 Nitrogen doping

Nitrogen content in the coatings increased with increasing nitrogen flow rate in an almost linear fashion, as was also observed by previous studies [48,52,59,60,70,133]. However, unlike most of the other previous works that reported a stable nitrogen content across the coating thickness [47,59] for all the nitrogen containing coatings deposited in this work, a small gradient, where the amount of nitrogen was higher towards the substrate was observed. An example of such a gradient across the coating is given in Figure 5.15 which shows the nitrogen elemental concentration across the cross-section of the coating. A similar nitrogen gradient was only reported by Dahm and Dearnley [48] for coatings containing nitrogen levels higher than 40 at%.

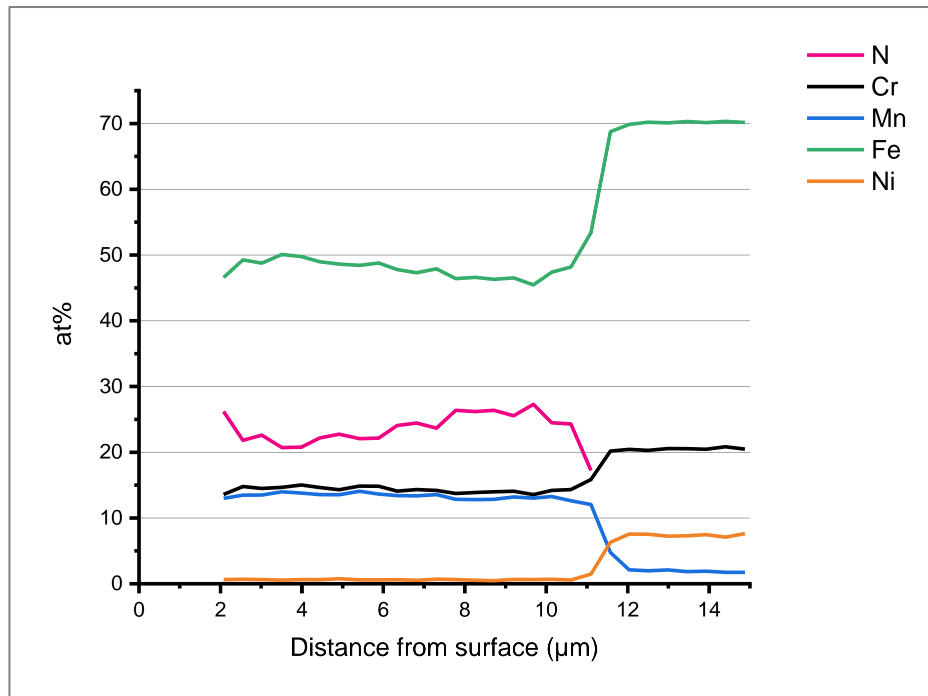

Figure 5. 15 Elemental composition by EDX, across the cross-section of a coating having an average of 24 at% nitrogen

Also of interest is that while some authors [47] have reported a diffusion of interstitial nitrogen across the interface to the substrate, in this study this was not detected. On the contrary, viewing any of the nitrogen-containing samples in a scanning electron microscope revealed a sublayer of the order of a few hundred nanometers (≈300 nm) (Figure 5.16). (For those coatings having a low nitrogen content, the use of the back-scattered electron imaging was required to identify this layer.) This sublayer seems to be absent of nitrogen and would represent the 5 minute deposition without nitrogen and subsequent nitrogen flow rate ramp up at the beginning of every run. Although this could not be confirmed by EDX due to equipment limitations, the fact that it is absent from coatings having no nitrogen and that its dimensions would roughly correspond to the 5 minute nitrogen free deposition and ramp up, support this argument.

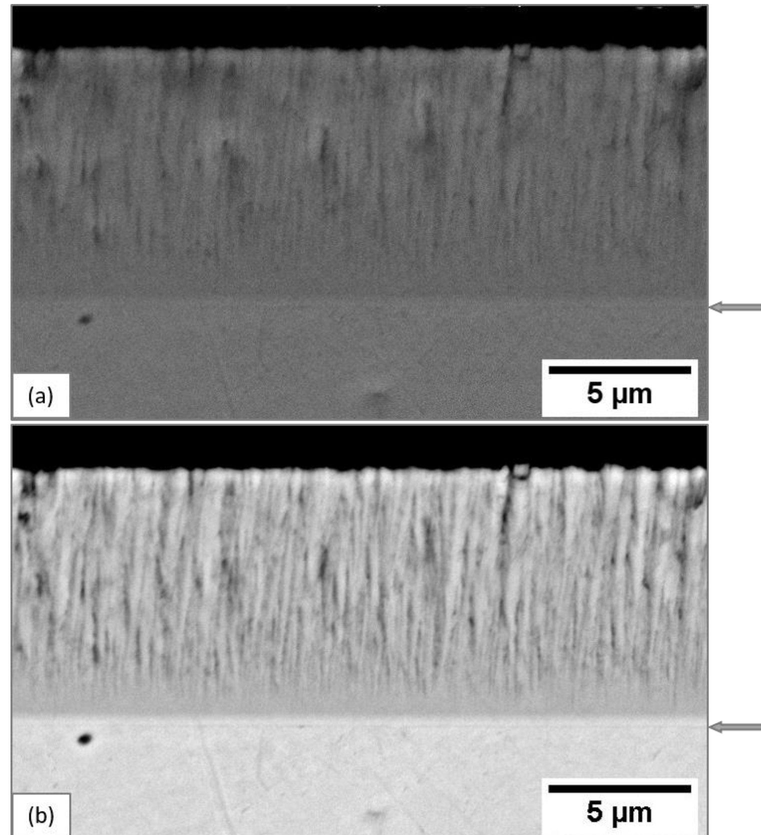

Figure 5. 16 Cross-sectional images of a 29 at% Nitrogen containing deposit in SE (a) and BSE (b) modes. Arrows show the interface

Furthermore, with increased nitrogen content, polished samples no longer appeared as white, featureless, dense coatings; vertical patterns as shown in Figure 5.16 became more evident. Perhaps this is further evidence of a change in morphology, which from the Zone T of a nitrogen-free coating (Figure 5.6 (c)-(d)) changed to a columnar structure, as shown in the Figure 5.17. The transition from a Zone T to a columnar structure typical of Zone 2 with the addition of nitrogen for austenitic coatings was also observed by Fryksa and Baranowska [47] and Dahm and Dearnley [48].

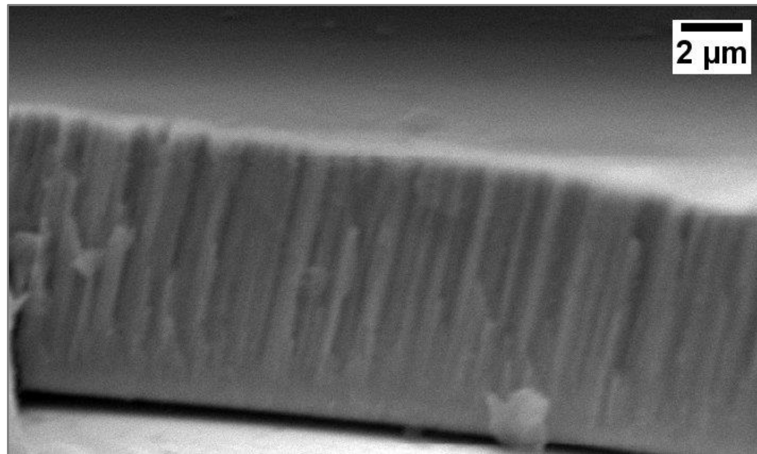

Figure 5. 17 Fracture of 24 at% nitrogen coating (deposited using a pulsed target power of 1200 W and a pulsed substrate bias of -70 V) showing a columnar structure

Figure 5.18 shows the XRD patterns of 4 coatings having different levels of nitrogen: zero, 7, 13 and 24 at%. Superimposed on the diagram are the peak positions of ferrite in grey (PDF card 00-006-0696) and austenite in orange (PDF card 04-018-3211).

The coating without nitrogen shows a mostly ferritic structure, with a (200) preferential orientation. As has been previously discussed in Section 5.2, this phenomenon has been reported by many studies [48,52,60,133,161]. Nevertheless, contributing to this change may also be the slight loss of manganese and maybe nitrogen, both of which are austenite stabilisers, from the original target composition. As the nitrogen was introduced into the chamber, the microstructure changed first to a mixture of ferrite and austenite (7 at% nitrogen coating in Figure 5.18), and subsequently to a fully austenitic structure with further increase in nitrogen content (13 and 24 at% nitrogen coatings). The (200) preferential orientation is maintained in the austenitic coatings and becomes stronger with further nitrogen increase. This (200) preferential orientation has also been reported

by other works [48,60,70,133,171]. Similar to previous studies [48,52,59,70,128], the peak(s) shift to lower angles and the lattice parameter increases with nitrogen addition.

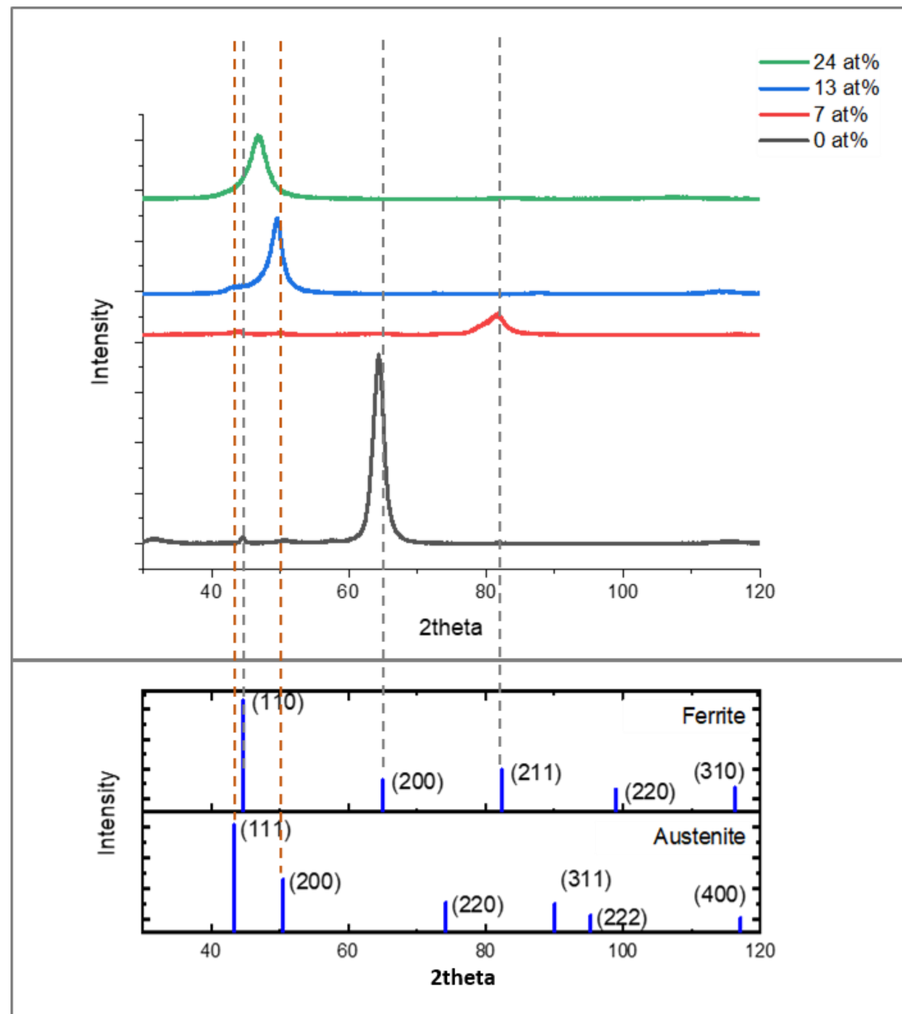

Figure 5. 18 Theta-2theta XRD patterns of coatings with different nitrogen levels: 0, 7, 13 and 24at%, all remaining parameters constant

As can be seen in Table 5.8, with the nitrogen increase, the hardness increased, until at 23.8 at% nitrogen, the hardness of 18.5 GPa was the highest measured in this study. Higher nitrogen increases, as could be perceived from previous sections in this chapter,

have resulted in a severe hardness drop (Sections 5.4, 5.6). In general, hardness measurements were sometimes difficult to make because of coating disbondment, as shown for instance in Figure 5.11 (Section 5.5), or substrate damage, (discussed in the following section, Section 5.9) – both of which could have resulted in the instrument partly measuring the coating deflection (as the tip pushed the coating towards the substrate) rather than the hardness of the coating itself. In fact, load-displacement curves obtained often showed such a drift before the actual indent began. In the light of these difficulties, the only conclusion that could be drawn with some confidence is that hardness increases with nitrogen content, until it reaches 23 at%N, in accordance with many previous literature studies [48,52,53,59,70,122,153,161]. However, further investigations have to be undertaken to understand what happens at higher nitrogen levels. In the literature, several authors have reported the hardness to stop increasing after some level of nitrogen concentration has been reached [52,128], and sometimes the hardness levels off at a lower value than the maximum hardness observed [58,59]. However, when presented, the results in these studies [48,52,153] often showed increased percentage errors for hardness values at higher nitrogen content, compared to those at lower nitrogen concentrations. The reasons for such behaviour are never explicitly stated, but would probably be the result of having phase changes due to nitride precipitation.

The increase in hardness between the coating deposited with no nitrogen in the chamber (8.0 ±1.2 GPa) and that of the target (5.9 ±0.5 GPa) could be attributed to process induced stress and grain refinement. While the stress in the coatings will be discussed in the next section, the grain size of the coatings in this study was estimated to be in between 10-20 nm, as measured by a selected area electron diffraction analysis. In the nanocrystalline regime, the Hall-Petch relationship, which predicts an increase in hardness with grain

size reduction [15] is not valid: while some researchers found the hardness to be less than that predicted by the equation [172–174] others observed softening at very small grain sizes [174–176]. In any case, hardness increases by grain refinement play only a minor role in these coatings and the larger hardness increases have been observed as the interstitial nitrogen quantities in solid solution increased. For this reason, further investigation of the grain size was not pursued and instead all hardness analyses were limited to comparisons of coatings within this study.

nitrogen (at%)	**±σ**	**Hardness (GPa)**	**±σ**
0.0	n/a	**8.0**	1.2
7.3	1.6	**4.1**	1.3
13.0	1.0	**14.5**	1.5
23.8	0.8	**18.5**	1.5
Staballoy AG17 (target)		**5.9**	0.5

Table 5. 8 Hardness for coatings having different nitrogen contents

5.8.1 Corrosion testing

A tentative potentiodynamic test in Ringer's solution was conducted comparing the zero nitrogen coating and the coating with 24 at% nitrogen. Another test was also conducted on the untreated substrate material AISI 304, a staple austenitic stainless steel, for comparative purposes.

From the polarization curves shown in Figure 5.19, it can be seen that all three samples exhibit passivity at low voltages. However, as the voltage is increased, the untreated AISI 304 substrate and the coating without nitrogen experience pitting, i.e. sudden large

increase in current density due to this localised corrosion phenomena. Breakdown potentials are at about 285 and 650 mV, respectively. At the end of these tests, the surfaces of both of these test specimens incurred localised corrosion in the form of pitting. Prior to the breakdown potential, metastable pitting events can be observed for both of these materials. On the other hand, the curve for the coating containing 24 at% nitrogen shows no metastable pitting events and no breakdown potential, meaning that this specimen remained passive up to 1000 mV, which indicates that the pitting corrosion resistance has been improved over the coating without nitrogen and the untreated AISI 304 substrate.

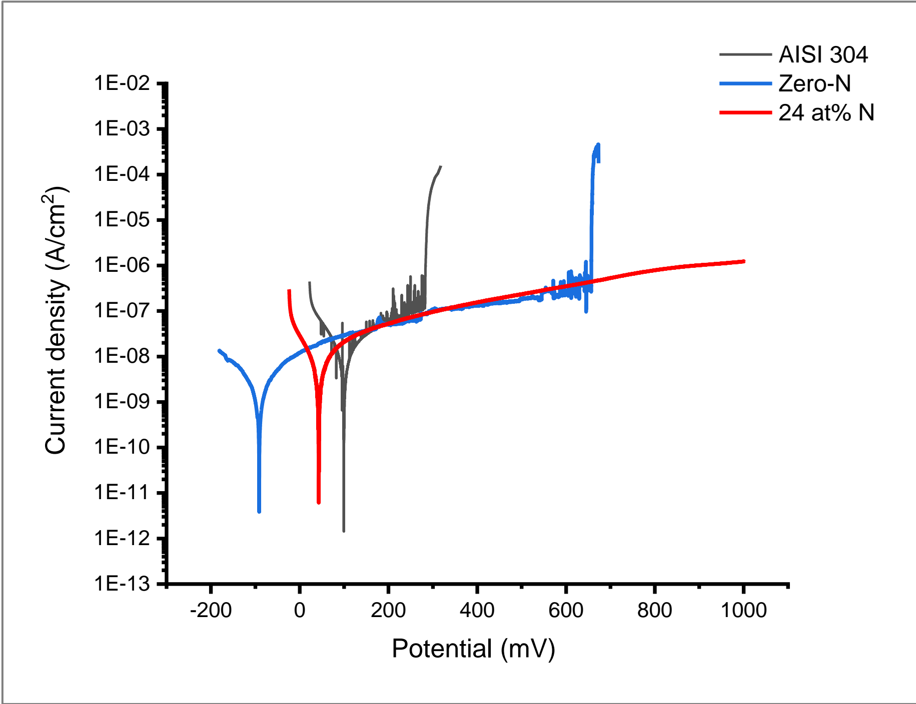

Figure 5. 19 Potentiodynamic tests in Ringer's solution for AISI 304 steel (grey), Staballoy AG17 coating with no added nitrogen (blue) and with 24 at% nitrogen (red). Coatings were deposited at a pulsed target power of 1200 W and pulsed substrate bias of -70 V

OCP values obtained in these tests could suggest some deterioration in general corrosion resistance of the zero-nitrogen sample (OCP at -90 mV) with respect to the untreated sample (OCP at +102 mV) and the 24 at% coating (OCP +42 mV), however, no strong conclusions can be made on this result in absence of repeated tests. Since these latter two samples are both austenitic, while the former is ferritic, such an increased susceptibility to general corrosion resistance is expected.

Although multiple tests should be conducted to validate a potentiodynamic test, these test results agree with multiple nitrogen-expanded austenite studies that show that with respect to untreated counterparts, pitting corrosion resistance in chloride solutions is improved, while the general corrosion resistance is maintained [45,49,62,63,177].

5.8.2 Nitride precipitation

Judging from the XRD patterns and the corrosion resistance of the coated sample containing 24 at% nitrogen (previous section), it would seem no detrimental chromium nitride precipitation occurred. However, at higher nitrogen contents, it appears that there is some precipitation of Mn_4N. It is difficult to ascertain with absolute certainty that Mn_4N has precipitated based on XRD patterns alone, because the peak shift of expanded austenite to smaller angles could overlap with the peaks of Mn_4N. However, as can be seen in Figure 5.20, the strong, relatively narrower peak at ≈40°, together with the appearance of smaller peaks at ≈69, 83 and 88° - which were not seen for any of the other lower nitrogen containing coatings, would suggest the presence of Mn_4N. (Peak positions for chromium nitrides and other manganese nitrides can be found in Appendix II, Figures II.2 and II.3 respectively).

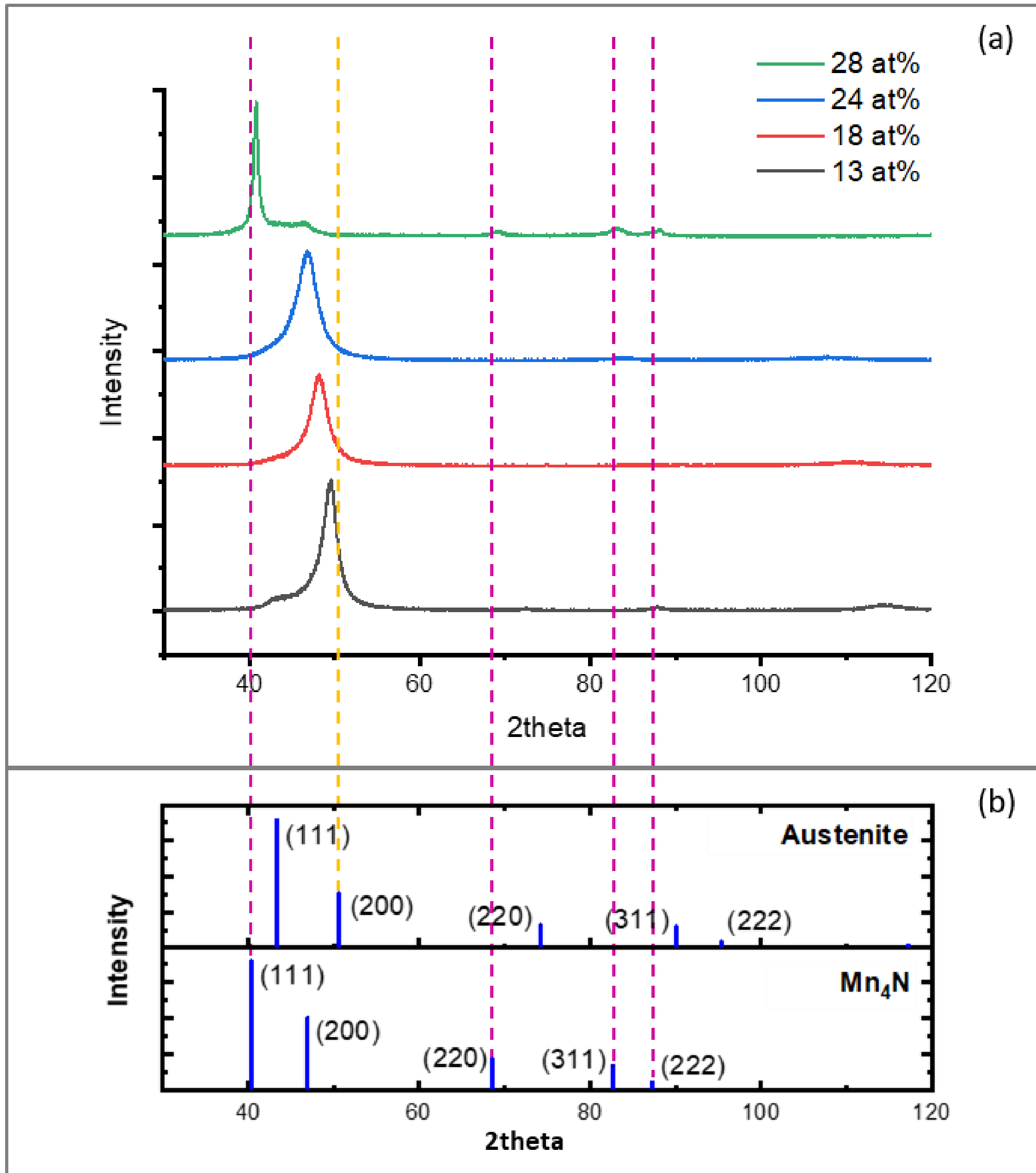

Figure 5. 20 (a) Theta-2theta XRD patterns for coatings containing high levels of nitrogen; (b) Peak positions for Mn_4N – PDF card 01-089-3704 and austenite, PDF card 04-018-3211

Since most of the more common austenitic stainless steels are a mixture of predominantly iron, chromium and nickel, in most expanded austenite studies, the onset of nitride formation usually means the precipitation of CrN [47,59,128]. Some studies [59,128] have shown that with increase in nitrogen, a stoichiometric MN is formed (where M is a

metal (e.g. Fe, Cr, Ni, Mo) that corresponds to the composition of the stainless steel target). On the other hand, studies of low temperature nitriding of the nickel free, high manganese content stainless steels ASTM F2581-07 (Fe-17Cr-11Mn-3Mo-0.5N-0.5Si-0.2C) and Staballoy AG 17 (same material as that used in this study), resulted in the precipitation of Mn_3N_2 [56], and CrN [71] respectively. A change in free energy – temperature diagram provided by Gemma et al. [178] (Figure 5.21) for various chromium, manganese and iron nitrides, would suggest that at temperatures lower than 500 °C, the formation of Mn_4N precipitates is most likely, given that its formation carries the highest change in free energy. The reasons why this nitride has not been reported to precipitate in austenitic stainless steel so far might be that: i) higher chromium levels, compared to manganese levels (if any) are present in the alloys generally studied (nickel-chromium alloys); and ii) difficulty in detecting this phase from XRD analysis.

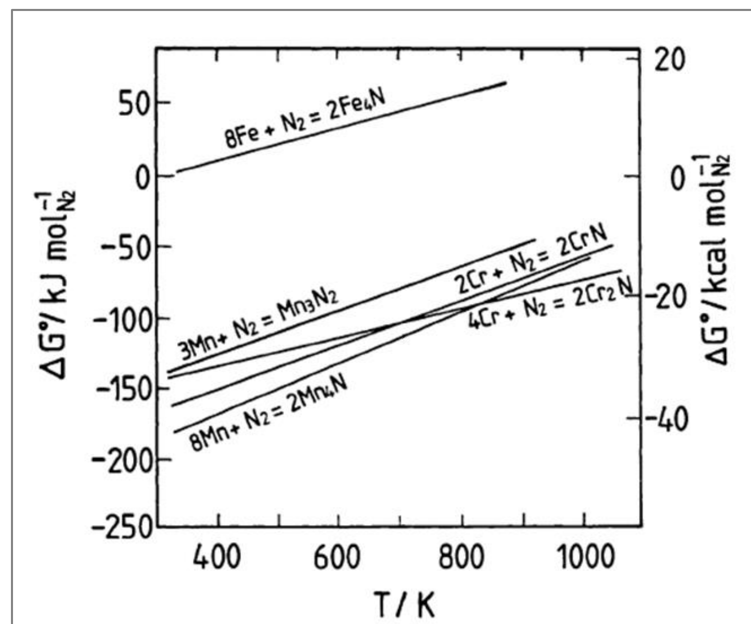

Figure 5. 21 Change in free energy against temperature for various chromium, manganese and iron nitrides, from [178]

Literature is not only unavailable for the precipitation of manganese nitrides in austenitic stainless steels but also for generic properties of compounds themselves (i.e. of the manganese nitrides). There are only a few [179,180] computational studies from first principles and these predict that Mn_4N is a stable, hard (24 and 18 GPa, respectively) and brittle phase. In this study, because of the adhesion problems experienced, an increase in hardness upon precipitation was not observed.

However, while a potential increase in hardness caused by manganese nitride, in addition to the increase in hardness that is brought about by expanded austenite would be attractive, understanding the implications of this kind of nitride precipitation on the corrosion resistance would be of utmost importance; because while the manganese nitride has precipitated, sensitisation of chromium has been avoided.

In the work of Buhagiar [181] mentioned earlier, the precipitation of Mn_3N_2 in austentitic stainless steel ASTM F2581-07, was accompanied by a deterioration of intergranular corrosion resistance. This deterioration was attributed to the dissolution of Mn_3N_2 precipitates that was manifested in current transients similar to those observed by Suter et al. [182] for MnS inclusions. Amongst the various theories of why the dissolution of MnS inclusions leads to increased pitting corrosion susceptibility is that proposed by Baker and Castle [183] which suggests that the dissolution of MnS inclusions releases Mn^{2+} ions in the presence of Cl^- ions and that in sufficient concentrations could result in the precipitation of a $MnCl_2$ salt film which prevents repassivation of the metal surface (exposed upon inclusion dissolution), leading to stable pitting conditions. Hence, while the theoretical work of Yu [179] predicts that Mn_4N is more stable than Mn_3N_2, understanding whether Mn_4N precipitates dissolve or not is of utmost importance as this

will in turn reveal whether the corrosion resistance of Staballoy AG17 with manganese nitrides is impaired.

5.9 De-adhesion and stress

In most cases, the coatings did not exhibit wrinkling upon unloading from the chamber. Nor did they fail catastrophically during subsequent cutting. Instead, in most cases the de-adhesion could only be observed under microscopic examination. However, there have been some cases when wrinkling was observed upon unloading or subsequent to a cutting process. In other even less frequent cases, the sample failed catastrophically during cutting as shown in Figure 5.22. The curling of the debonded parts of the film suggests that there is a stress profile within the film. In general, these observations would suggest that the coatings were in a state of very high residual stress and that any application of external load – such as cutting or mishandling during unloading – could result in spontaneous failure.

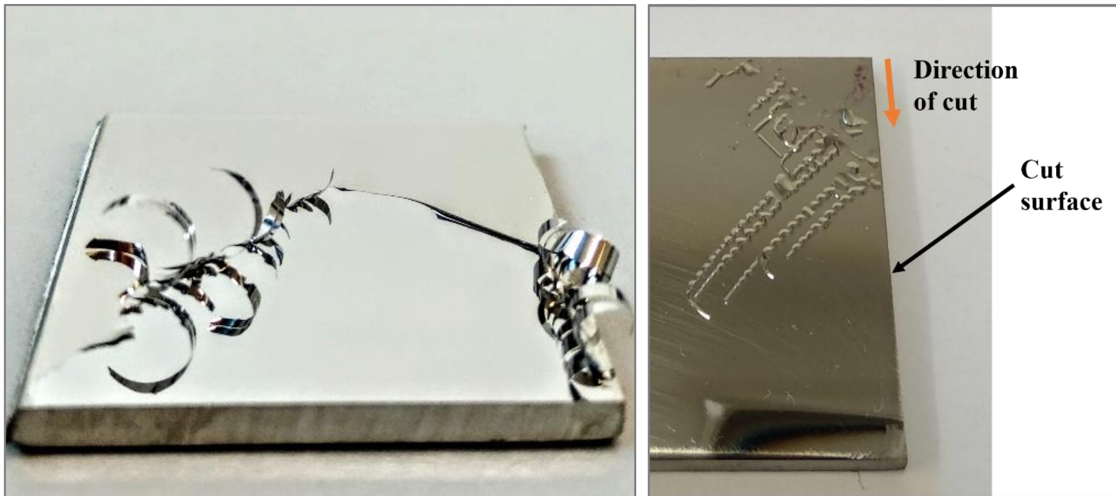

Figure 5. 22 Examples of compressive stress manifestations following cutting: (a) Catastrophic failure showing curling of a coating and (b) Worm-tracks following cutting.

In all of the coatings a delamination of the film from the substrate was observed under microscopic inspection; however, in some regions the coating-substrate interface was so smooth, it could barely be resolved. This would suggest that while the chemical bonding and adhesion between the film and the substrate is good, the cause of the de-adhesion was the result of high internal stresses. In fact, the fracture very often started in the nearby material region of the interface, within the substrate, as evidenced by Figure 5.23.

When the coating was thin enough (<6μm), buckling, in addition to substrate damage could be observed and when the curvature of the buckling was too large, fracture occurred (Figure 5.24, (a) and (b), respectively). For thicker coatings, only substrate damage could be observed.

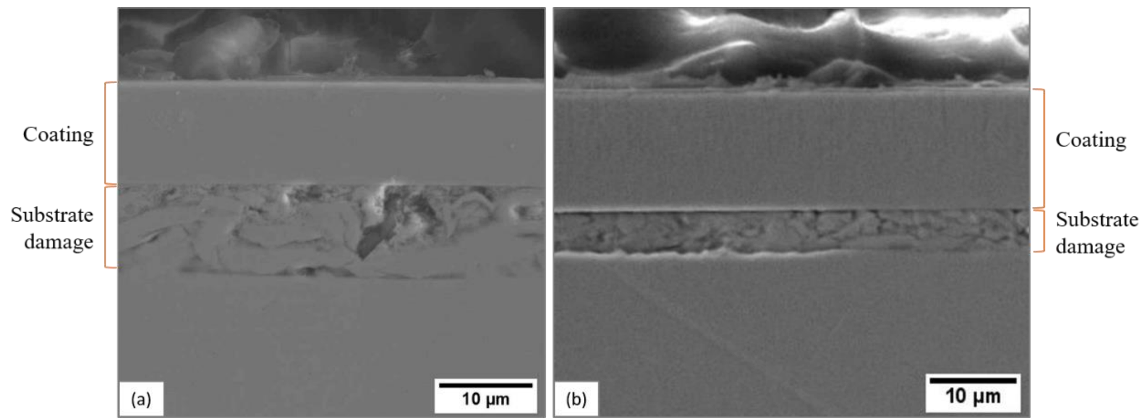

Figure 5. 23 An example of substrate damage in a coating that was deposited at a pulsed target power of 1200 W, pulsed substrate bias of -70 V and contains 7 at% nitrogen

Buckling and wrinkling are typical compressive stress failure modes; hence the buckling exhibited by the thinner coatings, the wrinkling, as well as lack of typical tensile failure modes (coating cracks, for example) in the thicker coatings show that the nature of the residual stress in the coating is compressive. Since in a film-substrate system, system compatibility requires that a stress within the coating is balanced out by an equal but opposite stress in the substrate, the substrate therefore incurs a tensile stress. The maximum stress that can be applied to the system is equivalent to the yield strength of the coating material, since once this is exceeded, the film would deform. However, in this case, the yield strength of the film exceeds the maximum stress the substrate can withstand in tension and hence, failure of the substrate can be observed.

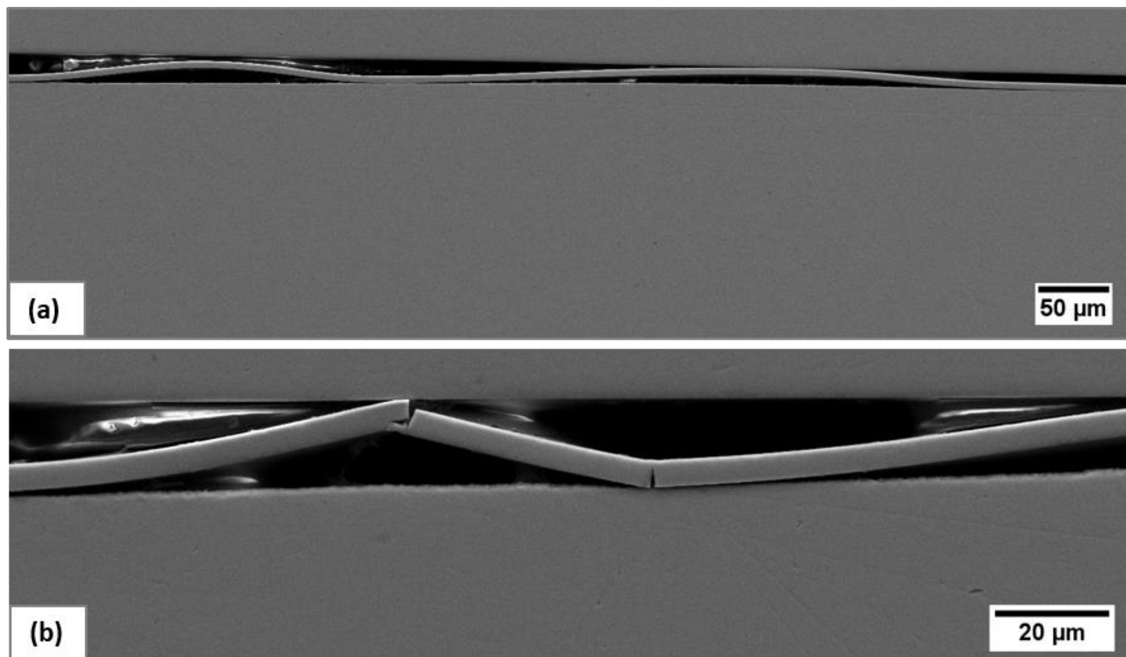

Figure 5. 24 Deadhesion (a) and fracture of delaminated coating (b) produced using a target power of 1200 W (123 kHz, 90 % duty cycle), substrate bias -110 V (250 kHz, 88 % duty cycle) and 4 sccm Nitrogen flow rate

This very high compressive stress is the accumulation of intrinsic and thermal stress. While the intrinsic stress results from the sputtering method employed and the incorporation of nitrogen into the coating – both of which are widely reported to increase the compressive stress in a system (Table 3.2 and Section 2.2.2), the thermal stress is imposed on the system while it cools down from the deposition run temperature (≈200 °C) to room temperature. Although the thermal expansion coefficient values for AG17 target material are not available in the literature, if the thermal expansion co-efficient of a similar alloy (for example, S28200, see Appendix I) is used, the thermal stress according to equation 3.2 for the film-coating system used in this study could be estimated and it will be found to be tensile and around 200 MPa.

However, it has been shown that the thermal expansion coefficient of expanded austenite decreases significantly with increasing nitrogen content [184]. It is therefore expected that the thermal stress for the nitrogen containing coatings would be compressive, the magnitude of which increases with increasing nitrogen content. Moreover, it can be deduced that the resultant compressive thermal stress was of a substantial magnitude, since all the attempts to try to reduce the intrinsic compressive stress in the system turned out to be futile. Indeed, the effect of changing process parameters (such as decreasing target power and substrate bias), that in theory should have decreased the compressive stress and hence decreased the buckling and deadhesion issues could not be observed.

A solution to decrease the effect of thermal stress would therefore be to use a substrate material that would shrink less than the coating as the sample is returned to room temperature. Glass substrates, for instance, would have worked had the resulting coatings not had a different structure (Section 5.7). Another solution that could have been tested if equipment availability had permitted, was to use nitrided AISI 304 substrates – since nitriding would result in a substrate which is under compressive stress, harder and of a low thermal expansion co-efficient (since the thermal expansion of expanded austenite diffusion layers is reported to decrease with nitrogen increase [184]).

The tests conducted in an attempt to reduce the intrinsic stress included: a reduction in target power (Section 5.3), duty cycle and frequency of target power (Section 5.4), reduction in substrate bias (Section 5.5) and pulsing of the substrate (Section 5.6). Planned future tests had included a non-pulsed target and a higher chamber pressure.

5.10 Summary

In this chapter the results were presented and discussed, starting from generic observations of the coatings, to deposition parameter effects on coating properties, nitrogen concentration effects, and finally stress (and de-adhesion of) in the coatings.

The process was stable, producing dense and featureless coatings, having a mirror-like finish and a Zone T morphology. Only minor compositional deviations between target and deposited layer were observed - as reported by other authors in the literature [47,59,70,160]. It has been proposed that a sublayer of denser morphology that was observed close to the substrate in this study as well as in others [58,97,117], is the result of an increasing substrate temperature.

Deposition parameter effects on the coatings can be summarized as follows:

- Target power: Increasing the target power increased the deposition rate, as has been reported by other studies [90,100,106,108]. Nitrogen content in the coatings and resulting phases remained unaffected, whilst the morphology coarsened and the hardness increased.
- Pulsed target parameters: While no arcing was observed for all the trials conducted, changes in the duty cycle of the pulsed target did not result in any evident differences in coating thickness, nitrogen content, hardness and texture. Similarly, increasing the frequency of the pulse at the target did not result in any changes except for an increased nitrogen concentration in the coatings as the frequency increased.
- Substrate bias: As the negative substrate bias was increased, the coating thickness and nitrogen concentration in the coatings decreased. These observations have

been explained by an increased re-sputtering effect on the coating together with a preferential re-sputtering of the lighter element nitrogen. It has been proposed that the decreased nitrogen content in the coatings and the opposing effect of increased stress in the coatings with increasing substrate bias maintained relatively stable coating hardness values.

- Substrate pulsing: When the substrate bias was pulsed as opposed to in DC mode, the ion flux density observed at the substrates was doubled. This increased ion flux density for pulsed substrate bias substrates resulted in an increased (preferential) re-sputtering of nitrogen, resulting in smaller nitrogen concentrations for pulsed substrate bias samples. Correspondingly, the hardness for pulsed substrate bias samples was slightly less than those deposited in DC mode, showing that in this study, the nitrogen concentration had a greater effect on hardness than pulsing the substrate bias. This is different to several studies [114,123,125,127] found in literature, whereby hardness increased when the substrate bias was pulsed.
- Substrate material: Coatings of Staballoy AG17 were deposited on glass and steel substrates, and although in both cases deposition was possible, the resulting coating structure, and consequently some of the coating properties (e.g. hardness) differed. These variations appear to be the result of different heat dissipation properties and substrate bias effects on the substrates. While this study sheds light on the importance of the substrate in setting the deposition conditions, these findings are in contrast with literature where some of the studies, although performing depositions on different substrate materials do not comment on [58,60,112], or find no differences in between [53], coatings deposited on different substrate materials.

High manganese stainless steel coatings with different quantities of nitrogen content were produced by varying the nitrogen flow rate into the chamber. Analysis of these coatings confirmed several observations previously reported in some studies of nickel-containing austenitic stainless steels, such as a hardness increase with increasing nitrogen content, the resultant texture having a predominant (200) orientation, and a coating morphology that changes from Zone T to Zone 2 with increasing nitrogen content. However, unlike other studies, the coatings exhibited a slight nitrogen gradient across the coating thickness, with the nitrogen content increasing towards the substrate. At the same time, no nitrogen diffusion from the coating into the substrate was observed.

Excessive nitrogen content resulted in the precipitation of Mn_4N within the coating – and an accompanying drop in hardness. To the knowledge of the author, Mn_4N has not been observed before – since it is usually chromium nitrides that are reported to precipitate for nickel containing stainless steels above some critical time/temperature threshold. Since theoretical computational studies [179,180] predict that Mn_4N is a hard and stable precipitate, the drop in measured hardness is thought to occur primarily as a result of coating delamination. Nevertheless, corrosion sensitisation due to chromium nitride precipitation has been avoided.

Finally the stress and de-adhesion issues in the coatings were considered. It was discussed how the coatings deposited were generally found to be in a state of high compressive residual stress that manifested in various forms (i.e. wrinkling, buckling, substrate damage, etc.). Also, that all attempts to reduce intrinsic stress were insufficient suggested that significant differential thermal contraction stresses were also present. Thus it was suggested that a substrate material with a thermal coefficient of expansion

that is smaller than that of the coating – or indeed a coating/substrate ‘buffer’ layer, of appropriate composition should be used.

The material Staballoy AG17, a high-manganese, high chromium, nickel-free austenitic steel, has never been used as a sputtering target material for coatings. In general, there are extremely few studies on PVD treated nickel-free materials, despite their benefit to the biomedical industry and their better economic value (due to replacement of expensive nickel by manganese). This work analyses the effects of several processing parameters, and very often compares the results obtained with works from other material systems, in the absence of literature review on the processing of austenitic stainless steel coatings. Most of the results presented above therefore impart novel information about Staballoy AG 17 and austenitic stainless steel coatings behaviour in response to the parameter changes studied. The most significant of these results is the suppression of chromium nitride precipitation at high nitrogen levels, which is widely known to deteriorate corrosion resistance. Other significant contributions include the often underestimated effects of the substrate material and the discussion of stress and stress manifestations in the coatings, which is very rarely discussed.

CHAPTER 6: CONCLUSIONS AND FUTURE WORK

6.1 Main findings

In this study, relatively thick austenitic stainless steel coatings with various nitrogen additions have been deposited. Following an extensive literature review of magnetron sputtering parameter effects (mostly featuring other materials, since literature on austenitic stainless steel coatings is very limited), it has been seen how process parameters can affect the structure and properties of the austenitic stainless steel coatings. The major findings for each of the parameters evaluated can be summarised as follows:

i) Target power: The increased momentum energy given to the growing film by the higher and more energetic flux condensing on or bombarding the substrate when the target power was increased resulted in a coarser Zone T structure and a higher hardness. Minimal effect of target power on the crystallographic phases formed was observed.

ii) Target pulsing parameters – duty cycle and frequency: While varying the duty cycle did not seem to have any effect on the coatings, increasing the pulse frequency increased the amount of incorporated nitrogen content in the coatings (all other parameters being maintained constant).

iii) Substrate bias: Increasing substrate negative bias led to an increased re-sputtering rate, that decreased both coating thickness and nitrogen content.

Since, despite the decrease in nitrogen content, no hardness shifts were observed, it was proposed that two simultaneous mechanisms that have opposing effects on the hardness were at play: increased stress due to atomic peening and loss of nitrogen due to re-sputtering.

iv) Substrate material: The thermal and electrical conductivity properties of the substrate ultimately determine the deposition conditions and thereby resulted in different coating structure, phases and texture between metallic, crystalline and non-metallic, amorphous substrate materials.

v) Pulsing of the substrate bias: When the substrate bias is pulsed, as opposed to in D.C. mode, nitrogen content in the coatings decreased due to re-sputtering (particularly of light elements, such as nitrogen).

On the other hand, the study of Staballoy AG17 coatings with different nitrogen content has revealed that:

i) Hardness increased with an increase in nitrogen content – and that the effect of nitrogen on the hardness is more profound than that of the deposition parameters
ii) The morphology changed from Zone T to Zone 2 with nitrogen addition
iii) While a nitrogen gradient that increased towards the substrate was observed, there was no evidence of nitrogen diffusion across the interface, into the substrate

iv) XRD diffraction patterns showed that Mn_4N, rather than CrN, was precipitated in coatings with high nitrogen contents. This would imply that sensitisation has been avoided.

Finally, a discussion of the stresses and failure modes involved concluded that the resultant residual stress was of a compressive nature and was caused by both intrinsic and thermal stress.

6.2 Future Work

In Section 5.9 it has been suggested that the thermal stress in the depositions should be addressed first in any future work as without a sound adhesion between coating and substrate, a thorough investigation of the properties of nitrogen doped austentic stainless steel costings would not be possible. A substrate with a linear thermal expansion coefficient that is less than that of the coating should be used. Nitrided substrate samples having an expanded austenite surface are strongly recommended (e.g. nitrided AISI 304) as such substrates would have a higher strength, be in a state of compressive stress and possess a low thermal expansion coefficient at the coating/substrate interface.

Once the thermal stress has been significantly reduced, parameters that could reduce the intrinsic stresses should once again be considered. Perhaps the most imminent of these parameter tests would be to conduct depositions without any target pulsing as pulsing has been reported to significantly increase energy of the ion fluxes at the substrate [92,111] while at the same time, stainless steel targets have generally not been reported to incur target poisoning, except in very high nitrogen atmospheres [47,48]. (Since the

scope of this work was aimed at studying intermediate nitrogen contents in the coatings, rather than these extreme limits, the potential risk for target poisoning at high nitrogen contents is limited). Other tests that could be carried out to reduce the intrinsic coating stress would be to increase the chamber pressure or to deposit a sublayer (e.g. of 5 μm) without nitrogen, thereby preparing a harder 'base layer' for the subsequent nitrogen-containing coating. Tests with simultaneous multiple parameter changes, such as reduced target wattage together with reduced substrate bias, should be considered.

The effect of coating thickness on the stress should also be taken into consideration since some works [96,97] show how stress could be accumulating with thickness. This generally sets a thickness limit for a given stress beyond which de-adhesion would occur. Yet, producing 10 μm thick austenitic stainless steel coatings by sputter deposition is not an impossible feat as evidenced by a number of studies [59,122,153,161].

6.3 Concluding remarks

This thesis has underlined the importance of a sputtering system's parameters, which cannot be over emphasised, as each parameter will, directly or indirectly affect the energy imparted to the growing film. This in turn affects the properties of the coatings – from its structure, to its attributes like hardness, density, conductivity etc.

Whilst energy intensification is necessary for the formation of a dense and functional coating, excessive flux energy may be deleterious to the coating adhesion – as is evidenced by the deposits in this study. Perhaps in this research, the extent of the adhesion problem and that of the thermal stress were underestimated, with the

consequence that it was thought that varying some deposition parameters (which would affect the intrinsic stress) would solve the problem. It turns out that varying one parameter at a time did not solve the problem – despite the initial parameter set being based on literature and experience of previous equipment users. In the end, although a substantial number of parameters have been evaluated in a very limited time (equipment breakdown), the optimum parameter set that would yield a perfectly adherent coating could not be established. However, this study remains a good starting point for other researchers to study the effect of nitrogen in nickel-free austenitic stainless steels. Many suggestions and recommendations have been produced to lead a researcher in the correct direction, in an area in which literature data is very scarce.

This area of study remains of interest because the potential applications for an austenitic stainless steel that has mechanical and wear resistance properties improved without compromising its generally good corrosion resistance would be numerous. Moreover, Staballoy AG17, the austenitic material used in this study has the further advantage of being free of nickel – which, other than making the price of the stainless steel more commercially viable, makes the material especially attractive to the medical industry by providing a relatively inexpensive alternative material to the widely-used nickel-containing stainless steels which can cause cytotoxicity issues.

Subsequent to success in depositing austenitic coatings with high amounts of nitrogen without delamination issues, investigations of manganese nitride precipitation should be considered to assess the potential of hardening the material by dispersion strengthening (through the precipitation of stable, hard Mn_4N precipitates) in addition to the higher hardness brought about by the expanded austenite structure. Since sensitisation appears to be avoidable in high-Mn stainless steels, it is of utmost importance to understand the

effects of manganese nitride precipitation on the corrosion resistance. In general, the use of strong nitride/carbide formers in low temperature PVD processes such as nitriding, for dispersion strengthening and corrosion resistance retention, has not yet been investigated [185]. If Mn_4N is found to be non-detrimental to corrosion resistance, the use of manganese instead of the more traditional titanium and niobium carbide/nitride formers should be studied as this would have the advantage that manganese is an austenite stabilizer, (rather than a ferrite stabilizer like Ti and Nb) – which means that there will be no issues with maintaining the austenitic structure of the alloy when higher quantities of the nitride/carbide former is required. Moreover, manganese is a significantly cheaper alloying element than either titanium and niobium.

REFERENCES

1. Lang Y, Qu H, Chen H, Weng Y. Research progress and development tendency of nitrogen-alloyed austenitic stainless steels. J Iron Steel Res Int. 2015;22(2):91–8.

2. Simmons JW. Overview: High-nitrogen alloying of stainless steels. Mater Sci Eng. 1996;A207(2):159–69.

3. Uggowitzer PJ, Harzenmoser M. Strengthening of austenitic stainless steels by nitrogen. In: Foct J, Hendry A, editors. High nitrogen steels HNS 88. Lille: The Institute of Metals; 1989. p. 174–9.

4. Norström L-Å. The influence of nitrogen and grain size on yield strength in Type AISI 316L austenitic stainless steel. Met Sci. 1977;11(6):208–12.

5. Rawers JC. Alloying effects on the microstructure and phase stability of Fe-Cr-Mn steels. J Mater Sci. 2008;43(10):3618–24.

6. ASM Handbook committee. Elevated-temperature properties of stainless steels. In: ASM Handbook Volume 1 Properties and Selection: Irons, Steels, and High Performance Alloys. 1990. p. 930–49.

7. Christiansen T, Somers MAJ. Controlled dissolution of colossal quantities of nitrogen in stainless steel. Metall Mater Trans A Phys Metall Mater Sci. 2006;37A(3):675–82.

8. Hauck Heat Treatment. Stainihard® NC Surface hardening of stainless steel [Internet]. [cited 2020 Jun 23]. Available from: https://stainihard.com/

9. Expanite - Surface hardening of stainless steel [Internet]. [cited 2020 Jun 23]. Available from: expanite.com

10. Bodycote. Specialty Stainless Steel Processes (S3P) [Internet]. 2019 [cited 2020 Jun 23]. Available from: https://www.bodycote.com/services/heat-treatment/specialty-stainless-steel-processes-s3p/

11. World Steel Association. The white book of steel. World Steel Association, 2012; 2012.

12. Krauss G. Steels processing, structure, and performance. 2nd ed. Ohio: ASM International; 2015.

13. Bain EC, Paxtron HW. Alloying elements in steel. 2nd ed. Ohio: American Society for Metals; 1961.

14. ASM Handbook. Classification and designation of carbon and low-alloy steels. In: ASM Handbook Volume 1 Properties and Selection: Irons, Steels, and High Performance Alloys. 10th ed. ASM International; 1990. p. 140–94.

15. Callister, Jr. WD, Rethwisch DG. Materials science and engineering. An introduction. 9th ed. Stenquist B, editor. Hoboken: Wiley; 2014.

16. British Stainless Steel Association. The discovery of stainless steel [Internet]. 2018 [cited 2019 Apr 13]. Available from: https://www.bssa.org.uk/about_stainless_steel.php?id=31

17. Cobb HM. The history of stainless steel. 2nd ed. ASM International, editor. Ohio; 2010.

18. British Stainless Steel Association. Melting temperature ranges for stainless steels [Internet]. 2018 [cited 2019 Jun 13]. Available from: https://www.bssa.org.uk/topics.php?article=103

19. European Committee for Standardization (CEN). Definition and classification of grades of steel. (BS) EN 10020:2000E. Brussels; 2000.

20. European Committee for Standardization (CEN). (BS) EN 10088-2:2014. Stainless steels - Part 2: Technical delivery conditions for sheet/plate and strip of corrosion resisting steels for general purposes. Brussels; 2014.

21. Regtuit H. About stainless steel [Internet]. EUROFER The European Steel Association. [cited 2019 Jul 8]. Available from: http://www.eurofer.org/Eurofer Stainless/About Stainless Steel.fhtml

22. Cunat P-J. Alloying elements in stainless steel and other chromium-containing alloys [Internet]. Euro Inox 2004. 2004 [cited 2019 Jul 8]. p. 1–24. Available from: https://www.bssa.org.uk/cms/File/Euro Inox Publications/Alloying Elements.pdf

23. British Stainless Steel Association. 50 Grades of stainless steel [Internet]. 2014 [cited 2019 Jul 8]. Available from: https://www.bssa.org.uk/50-grades-of-stainless-steel.php

24. British Stainless Steel Association. Classification of stainless steel types. Stainless Steel Advisory Service. SSAS Information Sheet No. 1.2. 2000. p. 1–2.

25. European Committee for Standardization (CEN). (BS) EN 10088-1:2014. Stainless steels Part 1 : List of stainless steels [Internet]. Brussels; 2014. p. 67. Available from: https://bsol.bsigroup.com/Bibliographic/BibliographicInfoData/000000000030254166

26. McGuire M. Stainless steels for design engineers. 1st ed. ASM International. Ohio: ASM International; 2008.

27. Grassel O, Kruger L, Frommeyer G, Meyer LW. High strength Fe-Mn-(Al, Si) TRIP / TWIP steels development - properties - application. Int J Plast. 2000;16:1391–409.

28. European Committee for Standardization (CEN). (BS) EN 10095:1999. Heat resisting steels and nickel alloys. Brussels: European Committee of Standardization; 1999. p. 1–26.

29. Kikuchi M, Kajihara M, Frisk K. Solubility of nitrogen in austentic stainless steels. In: Foct J, Hendry A, editors. High nitrogen steels HNS 88. Lille: The Institute of Metals; 1989. p. 63–74.

30. Stein G, Menzel J, Dorr H. Industrial manufacture of massively nitrogen-alloyed steels. In: Foct J, Hendry A, editors. High nitrogen steels HNS 88. Lille: The Institute of Metals; 1989. p. 32–8.

31. Mathew MD, Laha K, Ganesan V. Improving creep strength of 316L stainless steel by alloying with nitrogen. Mater Sci Eng A [Internet]. 2012;535:76–83. Available from: http://dx.doi.org/10.1016/j.msea.2011.12.044

32. Jargelius-Pettersson RFA. Electrochemical investigation of the influence of nitrogen alloying on pitting corrosion of austenitic stainless steels. Corros Sci. 1999;41(8):1639–64.

33. Shapiro MB, Bernshtein ML, Barsukova IM. Influence of nitrogen on the intercrystalline corrosion resistance of 03Kh19AG3N10-type steels. Met Sci Heat Treat. 1984;26(1):62–5.

34. International Stainless Steel Forum (ISSF). “New 200-series” steels: An opportunity or a threat to the image of stainless steel? Forum American Bar Association. Brussels: International Stainless Steel Forum (ISSF); 2005. p. 1–11.

35. Rawers J, Bennett J, Doan R, Siple J. Nitrogen solubility and nitride formation in Fe-Cr-Mn-Ni alloys. Acta Met mater. 1992;40(6):1195–9.

36. Speidel M. Properties and applications of high nitrogen steels. In: Foct J, Hendry A, editors. High nitrogen steels HNS 88. Lille: The Institute of Metals; 1989. p. 92–6.

37. Vanderschaeve F, Taillard R, Foct J. Discontinuous precipitation of Cr2N in a high nitrogen, chromium-manganese austenitic stainless steel. J Mater Sci. 1995;30(23):6035–46.

38. Simmons JW, Covino JBS, Hawk JA, Dunning JS. Effect of Nitride (Cr2N) Precipitation on the Mechanical, Corrosion, and Wear Properties of Austenitic Stainless Steel. ISIJ Int. 1996;36(7):846–54.

39. Pickering F. Some beneficial effects of nitrogen in steel. In: Foct J, Hendry A, editors. High nitrogen steels HNS 88. Lille: The Institute of Metals; 1989. p. 10–31.

40. Jargelius-Pettersson RFA. Sensitization behaviour and corrosion resistance of austenitic stainless steels alloyed with nitrogen and manganese. ISIJ Int. 1996;36(7):818–24.

41. Fritz J. Effects of metallurgical variables on the corrosion of stainless steels. In: Cramer S, Covino JBS, editors. Corrosion: Fundamentals, Testing, and Protection Vol 13A. Ohio: ASM International; 2003. p. 266–74.

42. Menthe E, Rie KT. Further investigation of the structure and properties of austenitic stainless steel after plasma nitriding. Surf Coatings Technol. 1999;116–119:199–204.

43. Li XY, Sun Y, Bell T. The stability of the nitrogen S-phase in austenitic stainless steel. Z Met. 1999;90(November):901–7.

44. Lei MK, Zhu XM. Plasma-based low-energy ion implantation of austenitic stainless steel for improvement in wear and corrosion resistance. Surf Coatings Technol. 2005;193(1-3 SPEC. ISS.):22–8.

45. Buhagiar J, Dong H. Corrosion properties of S-phase layers formed on medical grade austenitic stainless steel. J Mater Sci Mater Med. 2012;23:271–81.

46. Sun Y, Li XY, Bell T. X-ray diffraction characterisation of low temperature plasma nitrided austenitic stainless steels. J Mater Sci. 1999;34(19):4793–802.

47. Fryska S, Baranowska J. Microstructure of reactive magnetron sputtered S-phase coatings with a diffusion sub-layer. Vacuum. 2017;142:72–80.

48. Dahm KL, Dearnley PA. On the nature, properties and wear response of s-phase coatings on AISI 316L. Proc Instn Mech Eng. 2000;214(Part L):181–98.

49. Samandi M, Shedden BA, Smith DI, Collins GA, Hutchings R, Tendys J. Microstructure , corrosion and tribological behaviour of plasma immersion ion-implanted austenitic stainless steel. Surf Coatings Technol. 1993;59:261–6.

50. Ichii K, Fujimura K, Takase T. Structure of the ion-nitrided layer of 18-8 stainless steel. Tech Rep Kansai Univ. 1986;27:135–44.

51. Leyland A, Lewis DB, Stevenson PR, Matthews A. Low temperature plasma diffusion treatment of stainless steels for improved wear resistance. Surf Coatings Technol. 1993;62(1–3):608–17.

52. Schneider JM, Rebholz C, Voevodin AA, Leyland A, Matthews A. Deposition and characterization of nitrogen containing stainless steel coatings prepared by reactive magnetron sputtering. Vacuum. 1996;47(9):1077–80.

53. Alresheedi FI, Krzanowski JE. Structure and morphology of stainless steel coatings sputter-deposited in a nitrogen/argon atmosphere. Surf Coatings Technol. 2017;314:105–12.

54. Sun Y, Li X, Bell T. Low temperature plasma carburising of austenitic stainless steels for improved wear and corrosion resistance. Surf Eng. 1999;15(1):49–54.

55. Williamson DL, Ozturk O, Wei R, Wilbur PJ. Metastable phase formation and enhanced diffusion in f.c.c. alloys under high dose, high flux nitrogen implantation at high and low ion energies. Surf Coatings Technol. 1994;65(1–3):15–23.

56. Buhagiar J, Li X, Dong H. Formation and microstructural characterisation of S-phase layers in Ni-free austenitic stainless steels by low-temperature plasma surface alloying. Surf Coat Technol. 2009;204(3):330–5.

57. Riviere JP, Meheust P, Villain JP. Wear resistance after low-energy high-flux nitrogen implantation of AISI 304L stainless steel. Surf Coatings Technol. 2002;158–159:647–52.

58. Dahm KL, Dearnley PA. S phase coatings produced by unbalanced magnetron sputtering. Surf Eng. 1996;12(1):61–7.

59. Saker A, Leroy C, Michel H, Frantz C. Properties of sputtered stainless steel-nitrogen coatings and structural analogy with low temperature plasma nitrided layers of austenitic steels. Mater Sci Eng A. 1991;140(C):702–8.

60. Terwagne G, Colaux J, Mitchell DR, Short KT. Temperature effect of nitrided stainless steel coatings deposited by reactive DC-magnetron sputtering. Thin Solid Films. 2004;469–470(SPEC. ISS.):167–72.

61. Hannula SP, Nenonen P, Hirvonen JP. Surface structure and properties of ion-nitrided austenitic stainless steels. Thin Solid Films. 1989;181(1–2):343–50.

62. Menthe E, Rie K, Schultze JW, Simson S. Structure and properties of plasma-nitrided stainless steel. Surf Coatings Technol. 1995;74–75:412–6.

63. Zhu XM, Lei MK. Pitting corrosion resistance of high nitrogen f.c.c. phase in plasma source ion nitrided austenitic stainless steel. Surf Coatings Technol. 2000;131:400–3.

64. Szklarska-Smialowska Z. Pitting and crevice corrosion. Houston: Nace International. The Corrosion Society; 2005. p. 314.

65. Grabke HJ. The role of nitrogen in the corrosion of iron and steels. ISIJ Int. 1996;36(7):777–86.

66. Olsson COA. The influence of nitrogen and molybdenum on passive films formed on the austenoferritic stainless steel 2205 studied by AES and XPS. Corros Sci. 1995;37(3):467–79.

67. Diekmann W, Panzner G, Grabke HJ. The bonding state of nitrogen segregated on Fe(100) and on iron nitrides Fe4N and Fe2N. Surf Sci. 1989;218(2–3):507–18.

68. Hallab NJ, Jacobs JJ. Orthopedic applications. In: Ratner B, Hoffman A, Schoen F, Lemons J, editors. Biomaterials Science: An Introduction to Materials: Third Edition. Third Edit. Elsevier; 2013. p. 841–82.

69. Christiansen T, Somers MAJ. On the crystallographic structure of S-phase. Scr Mater. 2004;50(1):35–7.

70. Bourjot A, Foos M, Frantz C. Basic properties of sputtered 310 stainless steel-nitrogen coatings. Surf Coatings Technol. 1990;43–44(Part 1):533–42.

71. Tao X, Liu X, Matthews A, Leyland A. The influence of stacking fault energy on

plasticity mechanisms in triode-plasma nitrided austenitic stainless steel: Implications for the structure and stability of nitrogen-expanded austenite. Acta Mater. 2019;164:60–75.

72. Dong H. S-phase surface engineering of Fe-Cr, Co-Cr and Ni-Cr alloys. Int Mater Rev. 2010;55(2):65–98.

73. Mattox DM. Handbook of physical vapor deposition (PVD): film formation, adhesion, surface preparation and contamination control. 1st ed. Noyes Publications. Westwood: Noyes Publications; 1998. pages 29-39; 239-246; and Chapter 11.

74. Teeter FJ. Introducing SECA: A new industry association. Adv Mater Process. 2001;(July):28–30.

75. R.C. Tucker J. Surface engineering*. ASM Handbook, Vol 5A, Therm Spray Technol. 2013;5A:10–30.

76. Mahan JE. Physical vapor deposition of thin films. 1st ed. New York: John Wiley and sons, inc.; 2000. 336 p.

77. Holmberg K, Matthews A. Coatings tribology: properties, techniques and applications in surface engineering. Dowson D, editor. Vol. 7, Elsevier. Amsterdam: Elsevier Science B.V.; 1994. 448 p.

78. Aufderheide BE. Sputtered Thin Film Coatings. In: Tracton A a., editor. Coatings Technology Handbook [Internet]. 3rd ed. Boca Raton: CRC Press; 2005. Available from: https://www.crcpress.com/Coatings-Technology-Handbook-Third-Edition/Tracton/9781574446494

79. Rudolph M. Synthesis and characterization of magnetron-sputtered Ta N thin films for the photoelectrolysis of water. Université Paris-Saclay; 2017.

80. Betz G, Wien K. Energy and angular distributions of sputtered particles. Int J Mass Spectrom Ion Process. 1994;140(1):1–110.

81. Goehlich A, Niemöller N, Döbele HF. Determination of angle resolved velocity distributions of sputtered tungsten atoms. J Nucl Mater. 1999;266–269:501–6.

82. Pan AI-T. Adhesion, residual stresses and tribology of Rf sputter deposited titanium carbide coatings. University of Illinois at Urbana-Champaign; 1981.

83. Liljeholm L. Reactive sputter deposition of functional thin films. Digital Comprehensive Summaries of Uppsala Dissertations from the Faculty of Science and Technology. Uppsala: Acta Universitatis Upsaliensis; 2012. p. 1–52.

84. Kelly PJ, Arnell RD. Magnetron sputtering: a review of recent developments and applications. Vacuum. 2000;56:159–72.

85. Depla D, Mahieu S, Greene JE. Sputter Deposition Processes. In: Martin PM, editor. Handbook of Deposition Technologies for Films and Coatings. 3rd ed. Burlnigton: Elsevier Inc.; 2010. p. 253–96.

86. Takadoum J. Materials and surface engineering in tribology. 1st ed. London and Hoboken: ISTE Ltd. and John Wiley & Sons, Inc.; 2008.

87. Sproul WD. Multi-cathode unbalanced magnetron sputtering systems. Surf Coatings Technol. 1991;49(1–3):284–9.

88. Window B, Savvides N. Charged particle fluxes from planar magnetron sputtering sources. J Vac Sci Technol A Vacuum, Surfaces, Film. 1986;4(2):196–202.

89. Teer DG. A magnetron sputter ion plating system. United States Patent. United States; 5,556,519, 1996. p. 1–4.

90. Iriarte GF, Engelmark F, Ottosson M, Katardjiev I V. Influence of deposition parameters on the stress of magnetron sputter-deposited AlN thin films on Si(100) substrates. J Mater Res. 2003;18(2):423–32.

91. Carter D, Walde H, Mcdonough G, Roche G. Parameter optimization in pulsed DC reactive sputter deposition of aluminum oxide. 45th Annu Tech Conf Proceedings Soc Vac Coaters. 2002;570–7.

92. Bradley JW, Bäcker H, Aranda-Gonzalvo Y, Kelly PJ, Arnell RD. The distribution of ion energies at the substrate in an asymmetric bi-polar pulsed DC magnetron discharge. Plasma Sources Sci Technol. 2002;11(2):165–74.

93. Dhivya P, Prasad AK, Sridharan M. Effect of sputtering power on the methane sensing properties of nanostructured cadmium oxide films. J Alloys Compd. 2015;620:109–15.

94. Song JH, Wang SC, Sung JC, Huang JL, Lii DF. Characterization of reactively sputtered c-axis orientation (Al, B)N films on diamond. Thin Solid Films. 2009;517(17):4753–7.

95. Thornton JA, Penfold AS. Cylindrical magnetron sputtering. In: Vossen JL, Kern W, editors. Thin Film Processes. 1st ed. New York: Academic Press; 1978. p. 75–113.

96. Thornton JA, Hoffman DW. Stress-related effects in thin films. Thin Solid Films. 1989;171(1):5–31.

97. Detor AJ, Hodge AM, Chason E, Wang Y, Xu H, Conyers M, et al. Stress and microstructure evolution in thick sputtered films. Acta Mater. 2009;57:2055–65.

98. Billard A, Foos M, Frantz C, Gantois M. Corrosion-resistant and hard 310 stainless steel-carbon coatings prepared by reactive d.c. magnetron sputtering. Surf Coatings Technol. 1990;43–44(Part 1):521–32.

99. Wu CT. Intrinsic stress of magnetron-sputtered niobium films. Thin Solid Films. 1979;64:103–10.

100. Kavitha A, Kannan R, Rajashabala S. Effect of target power on the physical properties of Ti thin films prepared by DC magnetron sputtering with supported discharge. Mater Sci Pol. 2017;35(1):173–80.

101. Rossnagel SM, Cuomo JJ, Westwood WD, editors. Reactive sputter deposition. 1st ed. Handbook of Plasma Processing Technology. Fundamentals, Etching, Deposition and Surface Interactions. New Jersey: Noyes Publications; 1990.

102. Rossnagel SM, Kaufman HR. Current – voltage relations in magnetrons. J Vac Sci Technol A. 1988;6(2):223–9.

103. Depla D, Buyle G, Haemers J, De Gryse R. Discharge voltage measurements during magnetron sputtering. Surf Coat Technol. 2006;200(14–15):4329–38.

104. Westwood WD, Maniv S, Scanlon PJ. The current-voltage characteristic of magnetron sputtering systems. J Appl Phys. 1983;54(12):6841–6.

105. Stuart RV, Wehner GK. Energy distribution of sputtered Cu atoms. J Appl Phys. 1964;35(6):1819–24.

106. Liu YM, Han RQ, Liu F, Pei ZL, Sun C. Sputtering gas pressure and target power dependence on the microstructure and properties of DC-magnetron sputtered AlB2-type WB2films. J Alloys Compd. 2017;703:188–97.

107. Sproul WD, Rudnik PJ, Graham ME. The effect of N2 partial pressure, deposition

rate and substrate bias potential on the hardness and texture of reactively sputtered TiN coatings. Surf Coatings Technol. 1989;39/40:355–63.

108. Hoffman DW. Stress and property control in sputtered metal films without substrate bias. Thin Solid Films. 1983;107(4):353–8.

109. Sultan M. Effect of Gas Pressure and Gas Flow Rate on the Magnetic Properties of Sputtered Ni and Ni81Fe19 Films. Res J Nanosci Eng. 2018;2(1):1–8.

110. Kelly PJ, Henderson PS, Arnell RD, Roche GA, Carter D. Reactive pulsed magnetron sputtering process for alumina films. J Vac Sci Technol A Vacuum, Surfaces, Film. 2000;18(6):2890–6.

111. Arnell RD, Kelly PJ, Bradley JW. Recent developments in pulsed magnetron sputtering. Plasma Sci Technol. 2004;188–189:158–63.

112. Henderson PS, Kelly PJ, Bäcker H, Bradley JW. Investigation into the properties of titanium based films deposited using pulsed pulsed magnetron sputtering. Surf Coatings Technol 174–175. 2003;174–175:779–83.

113. Kelly PJ, Beevers CF, Henderson PS, Arnell RD, Bradley JW, Bäcker H. A comparison of the properties of titanium-based films produced by pulsed and continuous DC magnetron sputtering. Surf Coatings Technol. 2003;174–175(03):795–800.

114. Kelly PJ, Braucke T, Liu Z, Arnell RD, Doyle ED. Pulsed DC titanium nitride coatings for improved tribological performance and tool life. Surf Coat Technol. 2007;202:774–80.

115. Benegra M, Lamas DG, Fernandez de Rapp ME, Mingolo N, Kunrath AO, Souza RM. Residual stresses in titanium nitride thin films deposited by direct current and pulsed direct current unbalanced magnetron sputtering. Thin Solid Films. 2006;494:146–50.

116. Kim SP, Choi HM, Choi SK. A study on the crystallographic orientation with residual stress and electrical property of Al films deposited by sputtering. Thin Solid Films. 1998;322:298–302.

117. Janssen GCAM, Kamminga JD. Stress in hard metal films. Appl Phys Lett. 2004;85(15):3086–8.

118. Knoll RW, Bradley ER. Correlation between the stress and microstructure in bias-sputtered ZrO2-Y2O3 films. Thin Solid Films. 1984;117:201–10.

119. Catania P, Roy RA, Cuomo JJ. Phase formation and microstructure changes in tantalum thin films induced by bias sputtering thin films. J Appl Phys. 1993;74(2):1008–14.

120. Bland RD, Kominiak GJ, Mattox DM. Effect of ion bombardment during deposition on thick metal and ceramic deposits. J Vac Sci Technol. 1974;11(4):671–4.

121. Liu C. Structure , mechanical and tribological properties of hydrogen-free amorphous carbon films deposited by dual-frequency mode pulsed-DC magnetron sputtering. The Univeristy of Sheffield; 2017.

122. Darbeïda A, Saker A, Billard A, von Stebut J. Optimization of the surface mechanical strength of AISI 316L physically vapour deposited nitrogen-doped coatings on AISI 316L substrates. Surf Coatings Technol. 1993;60(1–3):434–40.

123. Freeman JA, Kelly PJ, West GT, Bradley JW, Iordanova I. The effects of composition and pulsed biasing on chromium nitride films. Surf Coat Technol. 2009;204:907–10.

124. Kelly PJ, Hall R, Brien JO, Bradley JW, Roche G, Arnell RD. Substrate effects during mid-frequency pulsed DC biasing. Surf Coatings Technol. 2001;142–144:635–41.

125. Gangopadhyay S, Acharya R, Chattopadhyay AK, Paul S. Effect of substrate bias voltage on structural and mechanical properties of pulsed DC magnetron sputtered TiN – MoS x composite coatings. Vacuum. 2010;84:843–50.

126. Audronis M, Matthews A, Leyland A. Pulsed-bias magnetron sputtering of non-conductive crystalline chromia films at low substrate temperature. J Phys D Appl Phys. 2008;41(3).

127. Lee J, Tien S, Kuo Y. The effects of pulse frequency and substrate bias to the mechanical properties of CrN coatings deposited by pulsed DC magnetron sputtering. Thin Solid Films. 2006;494:161–7.

128. Kappaganthu SR, Sun Y. Influence of sputter deposition conditions on phase evolution in nitrogen-doped stainless steel films. Surf Coatings Technol. 2005;198(1-3 SPEC. ISS.):59–63.

129. Thornton JA. High rate thick film growth. Annu Rev Mater Sci. 1977;7(1):239–60.

130. Thornton JA. Influence of apparatus geometry and deposition conditions on the structure and topography of thick sputtered coatings. J Vac Sci Technol. 1974;11(4):666–70.

131. Anders A. A structure zone diagram including plasma-based deposition and ion etching. Thin Solid Films [Internet]. 2010;518:4087–90. Available from: http://dx.doi.org/10.1016/j.tsf.2009.10.145

132. Fernandes CM, Ferreira VM, Senos AMR, Vieira MT. Stainless steel coatings sputter-deposited on tungsten carbide powder particles. Surf Coatings Technol. 2003;176(03):103–8.

133. Shedden BA, Kaul FN, Samandi M, Window B. The role of energetic neutrals in reactive magnetron sputtering of nitrogen-doped austenitic stainless steel coatings. Surf Coatings Technol. 1997;97(1–3):102–8.

134. Ohring M. The materials science of thin films. 1st ed. San Diego: Academic Press; 1992.

135. Windischmann H. Intrinsic stress in sputter-deposited thin films. Crit Rev Solid State Mater Sci. 1992;17(6):547–96.

136. Hoffman DW, Thornton JA. The compressive stress transition in Al, V, Zr, Nb and W metal films sputtered at low working pressures. Thin Solid Films. 1977;45(2):387–96.

137. Priest J, Caswell HL, Budo Y. Mechanical stresses in silicon oxide films. Vacuum. 1962;12(6):301–6.

138. Hoffman RW. Mechanical properties of non-metallic thin films. In: Dupuy CHS, Cachard A, editors. Physics of nonmetallic thin films. New York: NATO advanced study institutes series; 1976.

139. Buckel W. Internal stresses. J Vac Sci Technol. 1969;6(4):606–9.

140. Klokholm E, Berry BS. Intrinsic stress in evaporated metal films. J Electrochem Soc [Internet]. 1968;115(8):823. Available from: http://jes.ecsdl.org/cgi/doi/10.1149/1.2411441

141. Sun RC, Tisone TC, Cruzan PD. The origin of internal stress in low-voltage sputtered tungsten films. J Appl Phys. 1975;46(1):112–7.

142. Windischmann H. Temperature dependence of intrinsic stress in Fe, Si, and AlN prepared by ion beam sputtering. J Vac Sci Technol A Vacuum, Surfaces, Film. 1989;7(3):2247–51.

143. Doljack FA, Hoffman RW. The origins of stress in thin nickel films. Thin Solid Films. 1972;12:71–4.

144. Alexander PM, Hoffman RW. Effect of impurities on intrinsic stress in thin Ni films. J Vac Sci Technol A. 1976;13(1976):96–8.

145. Wagner RS. Tungsten metallization for LSI applications. J Vac Sci Technol. 1974;11(3):582.

146. Hoffman DW, Gaerttner MR. Modification of evaporated chromium by concurrent ion bombardment. J Vac Sci Technol. 1980;17(1):425–8.

147. D'Heurle FM, Harper JME. Note on the origin of intrinsic stresses in films deposited via evaporation and sputtering. Thin Solid Films. 1989;171:81–92.

148. Ahlgren M, Blomqvist H. Influence of bias variation on residual stress and texture in TiAlN PVD coatings. Surf Coatings Technol. 2005;200(1-4 SPEC. ISS.):157–60.

149. Thouless MD, Jensen HM. The effect of residual stresses on adhesion measurements. In: Mittal KL, editor. Adhesion Measurement of Films and Coatings. Utrecht: VSP; 1995.

150. Cammarata RC. Stresses in thin films. 1st ed. Totten GE, Liang H, editors. New York: Marcel Dekker; 2004. 21–34 p.

151. Laugier M. A note on the curling of thin films and its connection with intrinsic stress. Thin Solid Films. 1978;56:L1–2.

152. Jankowski AF, Bionta RM, Gabriele PC, Jankowski AF, Bionta RM, Gabriele PC. Internal stress minimization in the fabrication of transmissive multilayer x-ray optics. J Vac Sci Technol A. 1989;7(2):210–3.

153. Figueiredo Pina CG, Dahm KL, Fisher J, Dearnley PA. The damage tolerance of S-phase coated biomedical grade stainless steel. Wear. 2007;263(7-12 SPEC. ISS.):1081–6.

154. Dearnley PA. A brief review of test methodologies for surface-engineered

biomedical implant alloys. Surf Coatings Technol. 2005;198:483–90.

155. ATI. ATI staballoy AG17 ™ and staballoy AG17 ™ HS alloys technical data sheet. Pittsburgh: Allegheny Technologies Incorporated; 2014. p. 1–2.

156. International Organization for Standardization. ISO 5832-1:2016(E). Implants for surgery — Metallic materials — Part 1: Wrought stainless steel. 2016;(5th edition).

157. ASTM International. F1586-13. Standard specification for wrought nitrogen strengthened 21chromium — 10nickel — 3manganese — 2 . 5molybdenum stainless steel alloy bar for surgical implants (UNS S31675). 2013;1–5.

158. International Organization for Standardization. ISO 5832-9:2019(E). Implants for surgery — Metallic materials - Part 9: Wrought high nitrogen stainless steel. 2019;

159. Bückle H. Progress in micro-indentation hardness testing. Metall Rev. 1959;4(1):49–100.

160. Malavasi S, Oueldennaoua A, Foos M, Frantz C. Metastable amorphous and crystalline (a , O ’) phase in physical vapor deposited Fe-(Cr)-Ni-(C) deposits. J Vac Sci Technol A. 1987;5(4):1888–91.

161. von Stebut J, Darbeïda A, Saker A, Rezakhanlou R. Optimization of the contact mechanical strength of magnetron-sputtered nitrogen-doped AISI 316L physically vapour deposited coatings*. Surf Coat Technol. 1993;57:31–42.

162. Bräuer G. Magnetron Sputtering. In: Hashni MSJ, editor. Comprehensive materials processing. Elsevier; 2014. p. 4: 57-73.

163. Sidelev DV, Bleykher GA, Krivobokov VP, Koishybayeva Z. High-rate magnetron sputtering with hot target. Surf Coatings Technol [Internet]. 2016;308:168–73. Available from: http://dx.doi.org/10.1016/j.surfcoat.2016.06.096

164. Ekpe SD, Bezuidenhout LW, Dew SK. Deposition rate model of magnetron sputtered particles. Thin Solid Films. 2005;474:330–6.

165. Kobayashi T. Computer simulation of gas rarefaction effects and film deposition characteristics in a magnetron sputtering apparatus. Appl Surf Sci. 2001;169–170:405–9.

166. Hoffman DW. A sputtering wind. J Vac Sci Technol A. 1985;3:561–6.

167. Rossnagel SM. Gas density reduction effects in magnetrons. J Vac Sci Technol A Vacuum, Surfaces, Film. 1988;6(1):19–24.

168. Winters HF, Kay E. Gas incorporation into sputtered films. J Appl Phys. 1967;38(10):3928–34.

169. Kelly PJ, Hall R, Brien JO, Bradley JW, Henderson P, Roche G, et al. Studies of mid-frequency pulsed dc biasing. J Vac Sci Technol A. 2001;19(6):2856–65.

170. Vaz F, Machado P, Rebouta L, Cerqueira P, Goudeau P, Riviere JP, et al. Mechanical characterization of reactively magnetron-sputtered TiN films. Surf Coat Technol. 2003;174–175:375–82.

171. Grigore E, Ruset C, Li X, Dong H. Synthesis and characterization of (C, N)-alloyed stainless steel coatings by high energy ion assisted magnetron sputtering deposition. Mater Manuf Process. 2010;25(5):341–4.

172. Nieman GW, Weertman JR, Siegel RW. Mechanical Behavior of Nanocrystalline Metals. Nanostructured Mater. 1992;1:185–90.

173. Weertman JR, Niedzielka M, Youngdahl C. Hall-Petch behavior in nanocrystalline metals. In: Nastasi M, Parkin DM, Gleiter H, editors. Mechanical Properties and Deformation Behavior of Materials having Ultra-Fine Microstructures. 1st ed. Porto Novo: Springer-Science + Business Media B.V.; 1993. p. 241–54.

174. Liu XD, Nagumo M, Umemoto M. The hall-petch relationship in nanocrystalline materials. Mater Trans JIM. 1997;38(12):1033–9.

175. Chokshi AH, Rosen A, Karch J, Gleiter H. On the validity of the Hall-Petch relationship in nanocrystalline materials. Scr Metall. 1989;23:1679–84.

176. Schiøtz J, Di Tolla FD, Jacobsen KW. Softening of nanocrystalline metals at very small grain sizes. Nature. 1998;391:561–3.

177. Lei MK, Zhu XM. In vitro corrosion resistance of plasma source ion nitrided austenitic stainless steels. Biomaterials. 2001;22:641–7.

178. Gemma K, Satoh Y, Ushioku I, Kawakami M. Abnormal nitriding behaviour of a high chromium, high manganese austenitic steel. Surf Eng. 1995;11(3):240–5.

179. Yu R, Chong X, Jiang Y, Zhou R, Yuan W, Feng J. The stability, electronic structure, elastic and metallic properties of manganese nitrides. R Soc Chem. 2015;5(2):1620–7.

180. Adhikari V, Liu ZTY, Szymanski NJ, Khatri I, Gall D, Sarin P, et al. First-principles study of mechanical and magnetic properties of transition metal (M) nitrides in the cubic M4N structure. J Phys Chem Solids. 2018;120(November 2017):197–206.

181. Buhagiar J. Plasma surface engineering and characterisation of biomedical stainless steels. The University of Birmingham; 2008.

182. Suter T, Bohni H. New microelectrochemical investigations to study the initiation mechanisms of pitting. Electrochem Soc Proc. 1996;95(15):127–44.

183. Baker MA, Castle JE. The initiation of pitting corrosion at MnS inclusions. Corros Sci. 1993;34(4):667–82.

184. Brink B, Stahl K, Christiansen TL, Somers MAJ. Thermal expansion and phase transformations of nitrogen-expanded austenite studied with in situ synchrotron X-ray diffraction research papers. J Appl Crsytallography. 2014;47:819–26.

185. Christiansen TL, Dahl K V., Somers MAJ. New stainless steel alloys for low temperature surface hardening? Berg- und Huttenmann Monatshefte. 2015;160(9):406–12.

186. International A. A276/A276M-17 Standard specification for stainless steel bars and shapes. 2017. p. 1–8.

187. Makteitfrom.com. UNS S28200 Stainless steel [Internet]. Material Properties Database. 2018 [cited 2019 Jun 13]. Available from: https://www.makeitfrom.com/material-properties/UNS-S28200-Stainless-Steel

188. ASM International. ASM ready reference: thermal properties of metals (materials data series). Cverna F, editor. Ohio: ASM International; 2002.

189. Ashby M. Material property data for engineering materials. 4th ed. Granta Design; 2016. 1–27 p.

190. Hull FC, Hwang SK, Wells JM, Jaffee RI. Effect of composition on thermal expansion of alloys used in power generation. J Mater Eng. 1987;9(1):81–92.

APPENDIX I

The target used in this study was ATI's Staballoy AG17, while the substrates used were AISI 304. Since some of the properties of Staballoy AG17 are not provided by the supplier, the properties of a similar alloy – UNS S28200 – have been used for some estimations / calculations. The composition and thermal properties of staballoy AG 17, AISI 304 and UNS S28200 are given in Sections I.I and I.II.

I.I Composition of materials used

	C	Mn	Si	Cr	Ni	Mo	N	Others	Ref
Staballoy AG17	0.03	20	0.3	17	. . .	0.05	0.5	. . .	[155]
UNS S28200	0.15	17.0—19.0	1.0	17.0—19.0	. . .	0.75—1.25	0.40—0.60	Cu 0.75—1.25	[186]
AISI 304 (S30400)	0.08	2	1.0	18.0—20.0	8.0—11.0	. . .	. . .	. . .	[186]

Table I. 1 Chemical composition of materials used

I.II Relevant thermal properties

	Melting temperature (°C)		Thermal expansion coefficient (10^{-6}/°C)		Calculated thermal expansion coefficient (10^{-6}/°C)
Staballoy AG17	--		--		17.50
UNS S28200	1330-1380	[187]	18.4	[188]	17.41
AISI 304	1400-1450	[18]	17	[188]	18.35
Silica Glass	960 – 1,600	[189]	1.4 – 1.7	[189]	--

Table I. 2 Melting temperatures and thermal expansion coefficient from literature, and calculated using reference [190]

Although UNS S28200 and Staballoy AG 17 have relatively similar compositions, UNS S28200 contains additional carbon, molybdenum, silicon and copper, and potentially less manganese. Each of these small differences could increase or decrease the thermal expansion coefficient. However, the empirical formula to calculate the thermal expansion coefficient derived by Hull [190] suggests that the effects of these differences in alloying element contents would cancel out each other, resulting in a very similar thermal expansion coefficient for UNS S28200 and Staballoy AG17. Unfortunately, Hull's equation does not take into consideration the effect of copper. For the estimated thermal stress in Section 5.9, the actual value of UNS S28200 of 18.4×10^{-6}/°C was used.

APPENDIX II – XRD PEAK POSITIONS

In this section, the main XRD peak positions for known iron phases and nitrides that could be present in this study are presented.

II.1 Austenite and ferrite

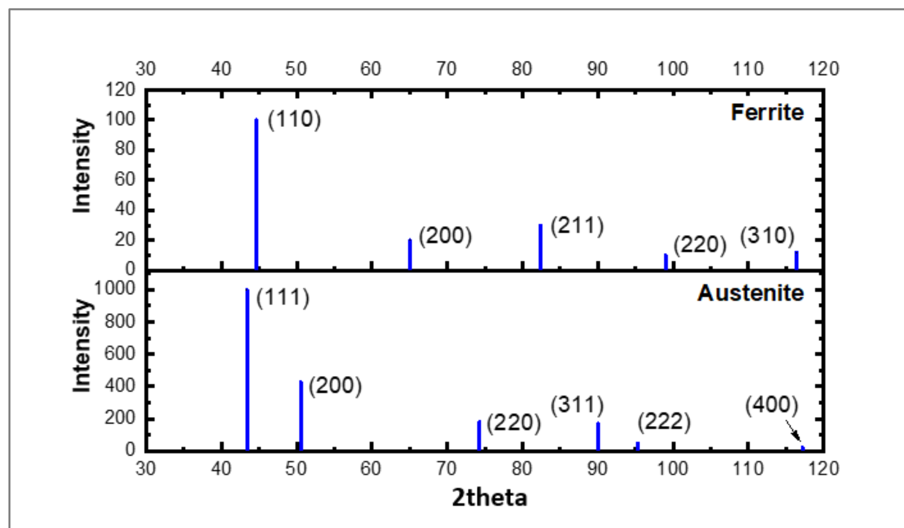

Figure II. 1 XRD peaks for ferrite, PDF card 00-006-0096 and austenite, PDF card 04-018-3211

II.2 Chromium nitrides

The chromium nitrides that are widely reported to precipitate in austenitic stainless steels are Cr_2N and CrN.

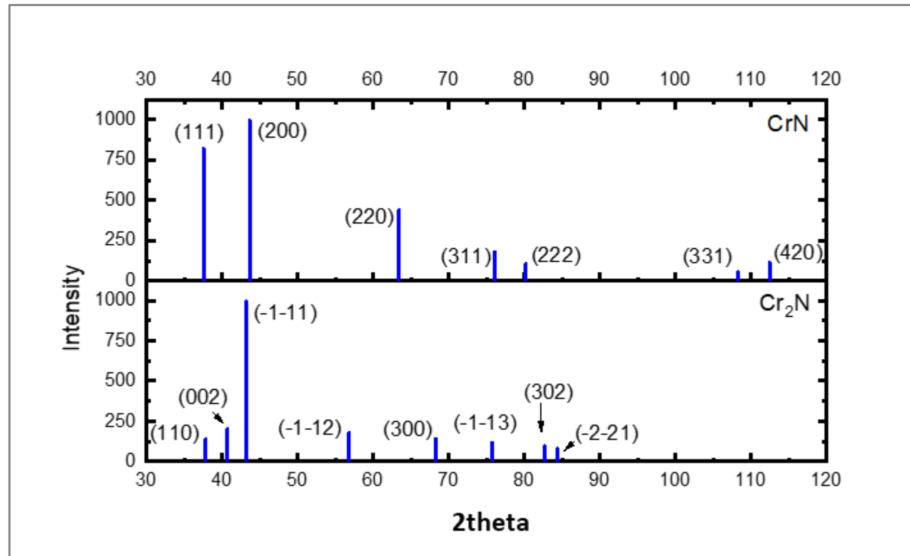

Figure II. 2 XRD peaks for CrN, PDF card 01-076-2494 and Cr_2N, PDF card 01-079-2159

II.3 Manganese nitrides

There are four stable intermediate phases that can be found in the manganese-nitrogen binary system. In order of decreasing stability [179], these are: MnN, Mn_4N, $Mn_2N_{0.86}$, and Mn_3N_2. The XRD peak reflections for these phases are given in Figure II.3.

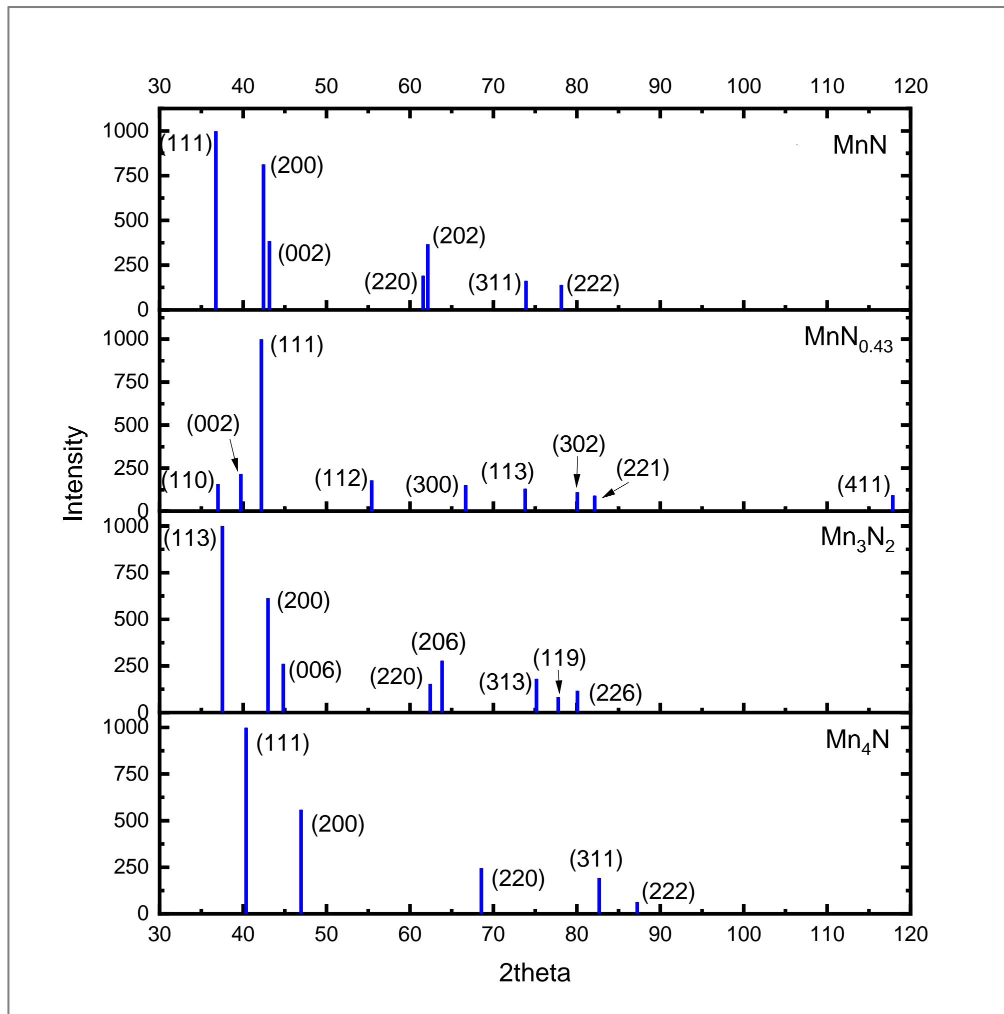

Figure II. 3 XRD peaks for MnN - PDF card 04-019-1077, $MnN_{0.43}$ - PDF card 04-007-2198, Mn_3N_2 - PDF card 01-089-3704 and Mn_4N - PDF card 01-089-3704